5-1-2018

An Analysis of Stresses and Displacements around a Fault Plane Due to Longwall Face Advance in Coal Mining

Corbin Grant Carlton
Southern Illinois University Carbondale, corbincarltonscc@hotmail.com

AN ANALYSIS OF STRESSES AND DISPLACEMENTS AROUND A FAULT PLANE DUE TO LONGWALL FACE ADVANCE IN COAL MINING

By

Corbin Carlton

B.S., Southern Illinois University Carbondale, 2012

A Thesis Submitted in Partial

Fulfillment of the Requirements

for the Degree of

Master in Science

in the field of Mining Engineering

Department of Mining and Mineral Resource Engineering

Southern Illinois University Carbondale

May 2018

THESIS APPROVAL

AN ANALYSIS OF STRESSES AND DISPLACEMENTS AROUND A FAULT PLANE DUE TO LONGWALL FACE ADVANCE IN COAL MINING

By

Corbin Carlton

A Thesis Submitted in Partial

Fulfillment of the Requirements

for the Degree of

Master in Science

in the field of Mining Engineering

Approved by:

Dr. Yoginder P. Chugh, Thesis Chair, MMRE

Dr. Joseph C. Hirschi MMRE

Dr. Tsuchin P. Chu, MEEP

Dr. Prabir K. Kolay, CE

Graduate School

Southern Illinois University Carbondale

May 2018

AN ABSTRACT OF THE THESIS OF

Corbin Carlton, for the Master of Science degree in Mining Engineering, presented on April 2nd 2018, at Southern Illinois University Carbondale.

AN ANALYSIS OF STRESSES AND DISPLACEMENTS AROUND A FAULT PLANE DUE TO LONGWALL FACE ADVANCE IN COAL MINING

MAJOR PROFESSOR: Dr. Yoginder P. Chugh

This study has examined 3D stresses and displacements around a longwall mining system that is intercepted by a geological fault. More specifically, the study has analyzed the effect of a fault on longwall gate development entries, set-up rooms, T-junctions, and the longwall face as the longwall face progressed toward, through, and away from the fault. A general lithologic sequence and mining parameters related to the Herrin No. 6 coal seam in southern Illinois were employed. FLAC3D structural analysis code was used for simulating two (2) adjacent longwall faces. Linear elastic rock mass elements with non-linear elastic-plastic fault elements were analyzed using Hoek- Brown brittle failure criteria. Two (2) models were developed for analysis: a base elastic case without fault and an elastic model with elastic-plastic fault elements. Engineering properties for the rock mass strata were derived from a history of rock core testing and modified following the process indicated for Hoek's Geologic Strength Index. Gob engineering properties and estimated load carrying capacities developed in earlier studies were used to make simulations physically realistic. The local tectonic (horizontal) stress field and vertical stress levels were applied to the simulation boundaries.

Analysis data was extracted for several data lines in the roof and floor that were determined to be critical based on the geometry of the mine layout. Extracted data included 3D stresses and displacements with the Z-direction indicating vertical. This data was used to calculate vertical convergence and vertical and horizontal stress concentration variables VSCF,

HSCF-XX, and HSCF-YY. Such data were developed for the longwall face advancing in 30-foot (10-m) increments away from the set-up room.

Incremental displacements due to the fault proved to be more significant than changes in stress concentrations VSCF, HSCF-XX, and HSCF-YY. Set-up room X-displacements show a consistent increase in the fault case around 35%. Incremental Y-displacements vary sharply at first then changes quickly reduce to zero (0). Z-displacements were similar in both models. A fault oriented more vertically would have larger Z-displacement values.

Gate X-displacements significantly decrease in the fault model until the face reaches 558 feet (170 m) from the starting point. Y-displacements show a rapid percentage rise in the fault model as the longwall face approaches the intersection of the fault with the first gate entry, but significant percentage decreases both before and after reaching this intersection. Significant increases in Z-displacements occur as the face approaches and leaves the intersection of the fault with the gate entries.

Around the fault, the first row of gate pillars experiences a change in horizontal displacements HSCF-XX and HSCF-YY of approximately 10%. Second row pillars also see a change in HSCF-XX of around 10%, but not a significant change in HSCF-YY. Gate entry VSCF values show significant increases at the fault intersection until the face passes the gate/fault intersection.

DEDICATION

To my family

ACKNOWLEDGEMENTS

I would like to thank Dr. Joseph C. Hirschi for the time that he took to review my work. His review not only included grammar and checks for consistency, but also was educational in regard to lessons in technical writing. Thank you Dr. Hirschi for both the quality of the review and the time you have dedicated to it.

Thank you, Harrold Gurley and Richard Lyon, for gathering the field data and our visits together to the mines. The trips were educational, impactful, and in one instance quite frightening. I will never forget being far from the ramp in a coal and having to make it back by turning off the vehicles headlights to conserve power in the battery. Going with you both down to the longwall mining areas gave me the ground level perspective of what the models in this work represent.

It is important that I thank my wife, Shaylin Carlton, for helping to maintain order in my life as I pressed onward to complete my master's while working full-time.

I started this journey 6 years ago. As an undergraduate I made the decision to sign up for an M.S. under Dr. Chugh. He and I have spent many hours together throughout this project. I've had the privilege to be his TA for 3 MNGE-431 courses, and the opportunity to work with Dr. Chugh on articles. His encouragement is reason why I was able to complete this document. No matter how much or how often I allowed life to get in the way, his persistence and willingness to get me through the M.S. program kept me focused and kept me going. Thank you Dr. Chugh for choosing me as a student, giving me the opportunities to teach students, spending hours going over concepts and analysis, and for not giving up on me.

TABLE OF CONTENTS

LIST OF TABLES

LIST OF FIGURES

CHAPTER 1

INTRODUCTION

1.1. Background

Historically, coal reserves that are closer to the surface are more economical to mine than coal that is deeper underground. Within the Illinois coal basin, near-surface economically mineable coal has largely been extracted. Currently, most of the coal mined in the Illinois coal basin comes from underground coal mines. The need for coal as an energy source remains strong in today's society; however, mining deeper coal reserves under adverse conditions presents challenges, particularly in regions where geological anomalies such as faults, folds, and dipping seams are present.

Due to economic and productivity pressures, several Illinois coal mines have determined that the longwall mining method (Figure 1.1) is worth the risk of the large capital investment required to pursue it. To mine coal using this method, development entries are driven from main entries along both sides of a block of coal and connected at the end by "set-up rooms" to establish the longwall face, which can be 900 to 1500 feet (274-457 m) long depending upon mining conditions and desired output. A slice of coal approximately 3-foot (1 m) wide is extracted each time the longwall shearer or plow travels the length of the face. Loosened coal falls off the face onto an armored face conveyor (AFC) chain. It travels in the AFC along the length of the face and is dumped onto a main belt conveyor through a stage loader and crusher. The belt conveyor carries run-of-mine coal to the surface where it may be processed and stockpiled prior to being shipped to the customer.

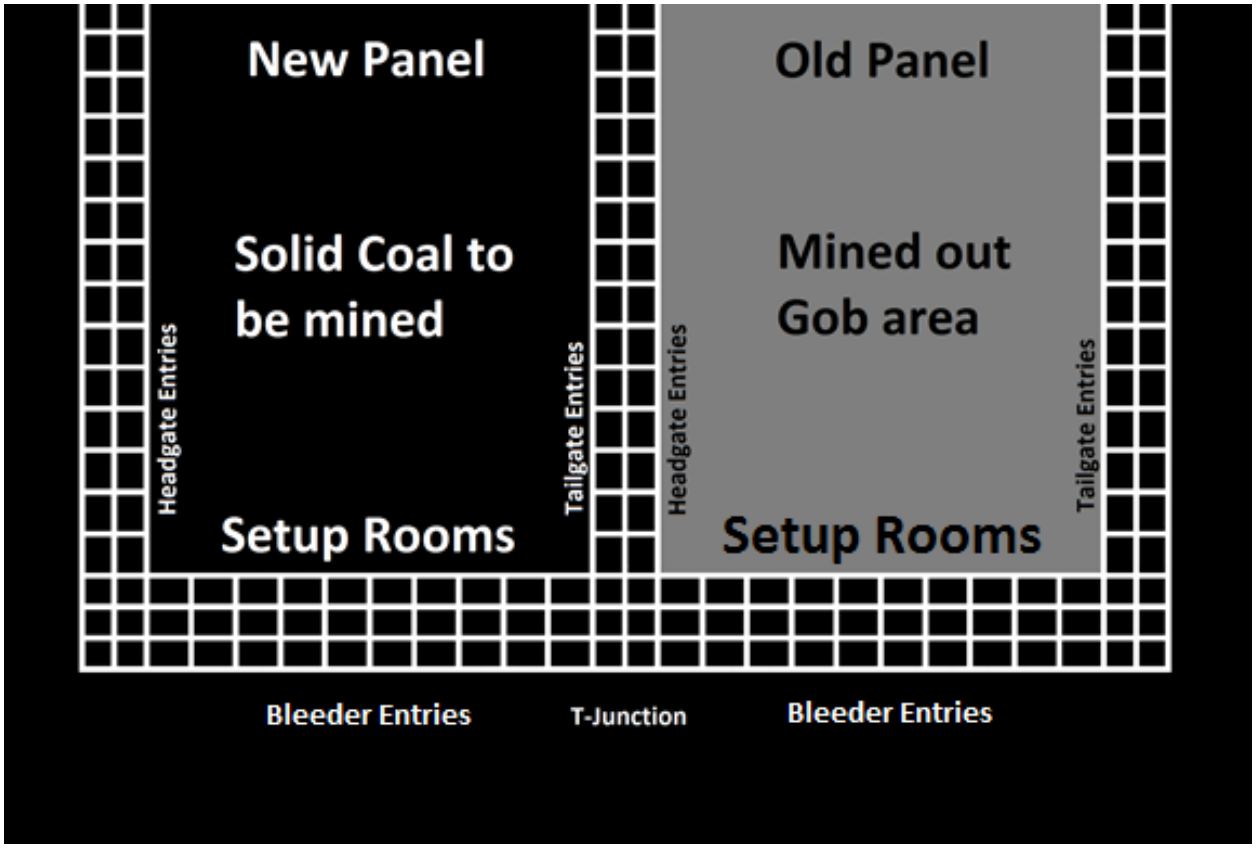

Figure 1.1: Example layout of adjacent longwall panels.

Along the entire length of the longwall face, the roof is supported by hydraulic steel supports called shields. These supports are advanced incrementally as coal is extracted. As supports advance, strata above the coal seam is allowed to cave and form a fractured gob material behind the face shields (Figure 1.2).

Longwall face advance rates have increased over time and are currently averaging 90 feet (27 m) per day with peak rates of 100 to 110 feet per day (30-35 m). This results in highly dynamic stress and displacement environments along the face and in the caving area behind the face. Mining companies must plan for ground control in the face area and in development areas to minimize production losses and maximize the safety of mine workers and equipment.

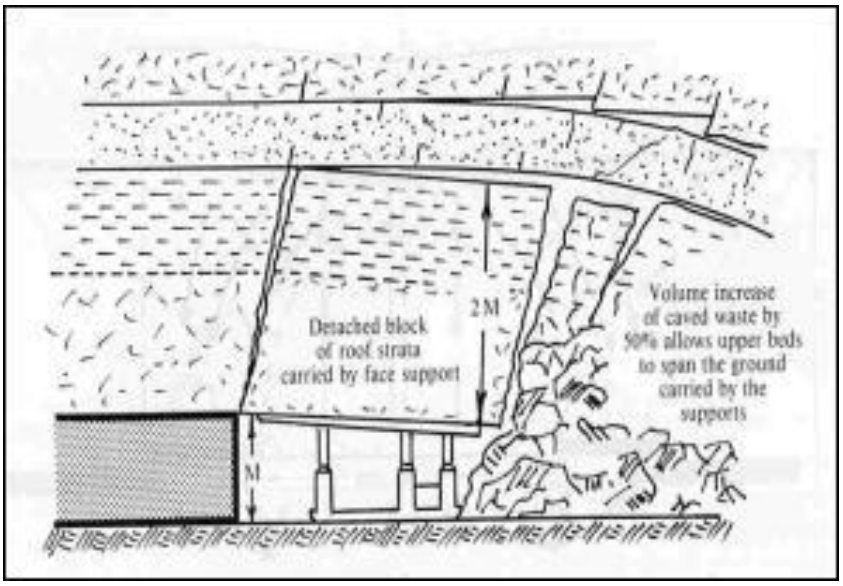

Figure 1.2: Rock mass supported by longwall shield support (Whittaker and Reddish, 1989).

1.2 Problem Statement

The longwall mining method is a very productive mining system capable of producing in excess of 20,000 clean tons per day. It is also a very safe mining system since workers are always under the continuous canopy of steel supports. However, this mining method is highly capital intensive due to the cost of support, materials handling, and extraction equipment. It is also a very inflexible mining method when it comes to geologic anomalies such as faults and dikes because it is extremely difficult to change mine layouts and very disruptive to change panel lengths. The only options are to mine through them or to leave large blocks of unmined coal by shortening panel lengths to avoid them. Both options can be very expensive and present economic challenges.

A fault plane in a geologic mass represents a discontinuity. The rock along the fault plane can be fractured and it lacks the stiffness of an undisturbed rock mass. Furthermore, there can be rigid body displacements or rotations along the fault plane during the mining process. Therefore,

there can be significant stress and displacement redistributions when mining through or around a fault zone.

Less stiffness will cause the fractured rock mass to shed its load to the stiffer non-fractured rock mass on both sides of the fault. This can result in significant loading of face supports as well as pillars and supports in development entries. Southern Illinois has a large concentration of faults when compared to other areas in the Illinois coal basin. These folds and shear zones within the coal basin are shown in Figure 1.3.

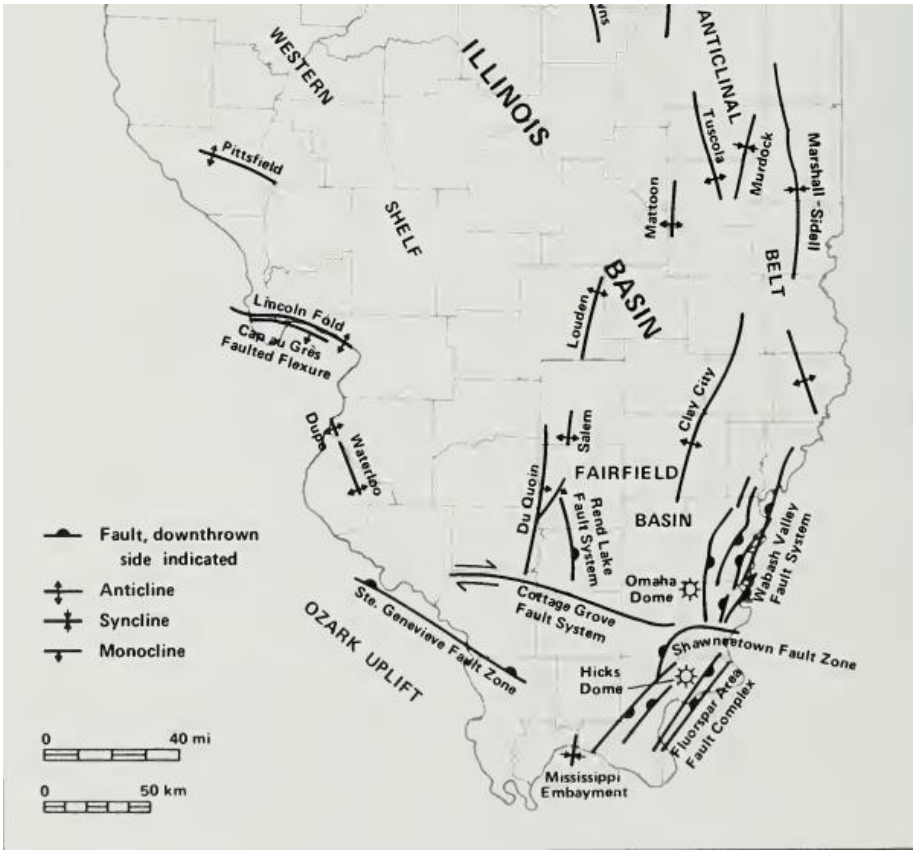

Figure 1.3: Faults in southern Illinois (from Nelson 1981).

Longwall coal mines require substantial coal reserves in terms of areal extent, which significantly increases the likelihood of encountering fault planes within a mining area. The

geometry and spatial extent of faults varies depending upon the geology of the area. Both of these characteristic parameters are significant factors influencing stress redistributions and displacement amounts in and around mining areas intercepted by one or more fault planes. Therefore, it is important to analyze stress and displacement distributions around a fault and use them to plan mining operations and determine the need for additional supports.

1.3. Goals and Specific Objectives

The goal of this study is to develop a better scientific understanding of how longwall stresses and displacements redistribute in and around mining areas and in the caved rock mass behind the face when a fault plane is in the vicinity of the longwall face. This is extremely important from mine planning, productivity, and worker and equipment safety points of view.

The more specific objectives of the study are to: 1) Develop a methodology for determining relevant rock mass strength and deformation parameters required as input into numerical models, with emphasis around faults; 2) Using FLAC3D software (developed by Itasca Consulting Group), construct a base numerical model of a longwall face and associated deforming rock mass material without introducing a fault plane; 3) Analyze results of the base model with in-mine field measurements to establish model validity; 4) If needed, modify the base model to increase accuracy and match modeling results with field measurements; 5) Utilize the validated numerical model to incorporate a fault plane within the rock mass; 6) Incrementally advance the longwall face to analyze stress and displacement redistributions due to a single fault plane; and 7) Develop recommendations for a mining company to allow passing through faulted areas without significant productivity losses and safety issues.

1.4. Significance of the Study

Production of coal by means of the longwall mining method has risen significantly in the United States during the last two (2) decades. During this same time period, the number of longwall mines in the United States has steadily decreased (Figure 1.5). Globally, longwall production has increased from just two (2) decades ago.

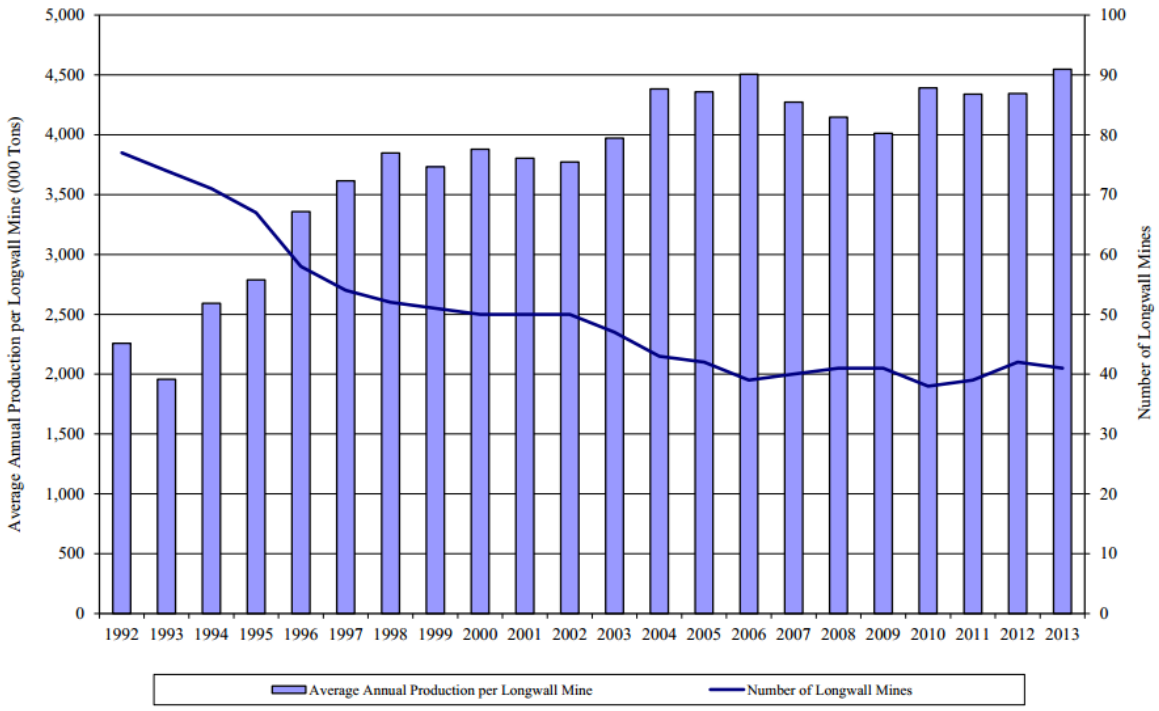

Figure 1.4: Average annual production per longwall mine and the number of longwall mines in the US, 1992 – 2013 (Weir United States Longwall Mining Statistics)

In the Illinois coal basin, use of the longwall mining method has experienced a sharp increase in both production and number of longwall mines during this same time period. Over the last 10 years, the number of longwall faces has increased from two (2) in 2005 to six (6) in 2014. Additional longwall faces are currently in planning stages.

Increasing application has resulted in greater potential for ground control problems while crossing faults. Problems involving ground control include roof falls, rib sloughing, and floor heave; all of which are related to stresses and displacements. Stress redistributions, inherent mechanical properties of unique strata, and geological structures such as faults are principal sources for issues involved with ground control. Ground control requires selecting and maintaining face supports as well as primary, secondary, and supplemental supports in gate development entries. Supplemental support design requirements and the timing of their installation are important considerations when crossing faults. The analysis of conditions around faulted longwall mining areas that is presented in this thesis can be used by mining companies and other researchers to develop solutions for improved safety and productivity when such conditions are encountered.

1.5. Thesis Structure

Chapter 2 reviews relevant literature to establish tasks for achieving research objectives. This includes reviewing previous research on engineering rock mass properties used as input for three-dimensional numerical modeling. Geological Strength Index (GSI) estimates and their relationships to Hoek-Brown rock mass strength estimates are also reviewed.

Chapter 3 describes the two (2) different numerical models of mine workings that were developed for analysis. They are: 1) A base model (Model 1) of a longwall panel's set-up rooms and gate development entries without faulting, and 2) A second model (Model 2) of the same mine workings with a fault running through set-up rooms and gate development entries (simulating the physical geometry of a fault in a case study mine). Non-linear modeling incorporating a fault could not be achieved due to time-run requirements. The fault was modeled

in FLAC3D as a Ubiquitous Jointed Rock Mass (UJRM) plane. Linear models were run and validated based on in-field studies and measurements at the case study mine site together with previous and ongoing research conducted by ground control research at Southern Illinois University Carbondale.

Chapter 4 explains analytical studies that evaluate stress and displacement redistribution in both models as the longwall face advanced in 6-foot (2 m) increments through a distance of 1005 feet (324 m). Analyses were performed along several different cross-sections within each model to assess effects of the fault on face supports and to formulate recommendations for improved mining operations and secondary and supplemental supports.

Chapter 5 provides a summary of the research including both analytical studies and modeling results. Recommendations for continuing this research are also presented.

CHAPTER 2

LITERATURE REVIEW

2.1. Overview of the Longwall Mining Method

There are two (2) primary extraction methods used in modern coal mines. The most common method since the mid-1900s has been the room-and-pillar mining method. This system requires coal to be extracted in multiple entries (rooms) that intersect with each other at right or near right angles to create networks of openings (Figure 2.1). Coal extraction is performed by a continuous miner. Entries are kept open with roof bolts as primary supports. These rooms are also stabilized by un-mined columns of coal, termed pillars, which are left in place between rooms. A room-and-pillar mine achieves extraction ratios of 40-50% in areas that are expected to stay stable over long periods of time. In areas of the mine primarily focused on production that will be sealed after mining, higher extraction ratios of 55-65% are achieved with different sized pillars in different areas.

The second prominent mining method is known as longwall mining. A block of coal between 1,000 and 1,500 feet (305-457 m) wide (Figure 2.1) is mined in slices of 3 feet (1 m) by a shearer with roof strata caving behind face support structures into the mined-out area. The length of the coal block (panel) varies from 10,000 to 15,000 feet (3050 to 4570 m). This mining system enables 100% extraction of coal within the longwall panel. In the United States (US), continual development and innovation of the longwall mining method since the early 1970s has increased production tonnages and led to reductions in operational costs on a per ton basis. However, longwall mining still requires large capital expenditures, long development times, a large contiguous mining area, flat or slightly dipping seams, and uniform coal seam thickness.

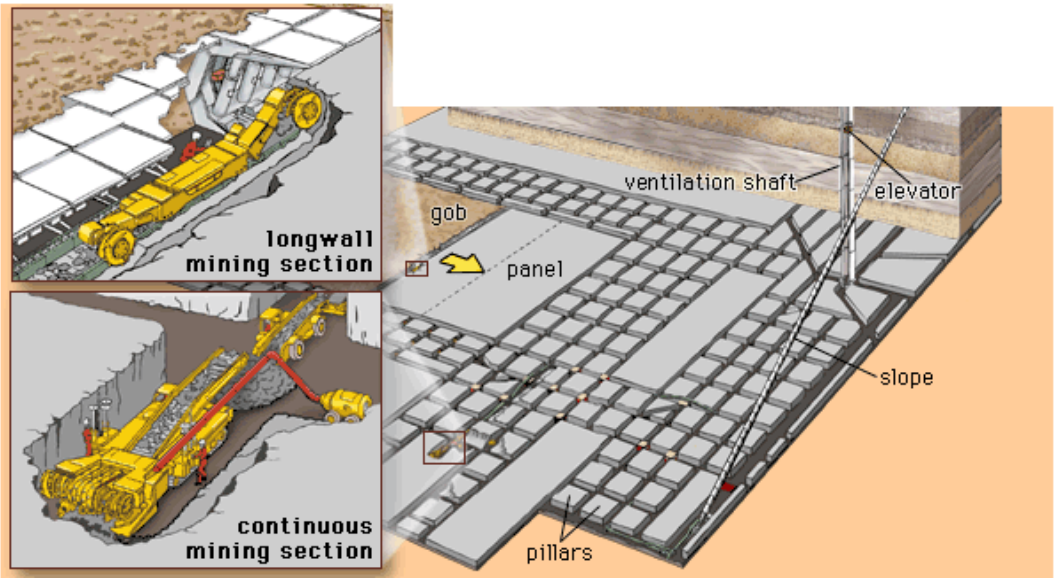

Figure 2.1: Depiction of both mining methods being used at a longwall mining operation (https://www.google.com/search images of longwall mining)

Room-and-pillar mining is an integral part of longwall mining as it is used to develop longwall gate entries and set-up rooms. Along both sides of the longwall panel, entries known as the headgate and the tailgate are developed for the entire length of the panel. When they reach full length, they are connected with entries known as set-up rooms that cross the full width of the panel. The front set-up room represents the starting point for the longwall face from which it advances toward main and/or sub-main entries (Figure 2.1). In the set-up room, hydraulic shields, the longwall shearer, and armored face conveyor (AFC) segments are positioned in alignment with each other along the entire longwall face.

Hydraulic shields protect mine workers and extraction equipment, which includes a longwall shearer and the AFC. As the shearer cuts coal from the face, it falls onto the AFC, which transports it to a stage loader where it is crushed and loaded onto a belt conveyor for transport to the surface. Each individual shield and its attendant AFC segment advance after the

shearer passes by on each cut. Once the shearer is a reasonable distance past a given shield, the shield pushes the AFC forward. Then the shield's hydraulic main jacks disengage releasing pressure on the roof. This allows the shield to pull itself forward by means of another hydraulic jack connected to the AFC.

If the mining direction is from the set-up room towards main entries, it is considered to be retreat longwall mining. With this approach, workers are always in a stable geological environment. In other countries, advance longwall mining has been practiced where the face starts at a point close to the main entries and mines toward the furthest extent of the coal block. In this method, gate entries and the longwall panel are mined simultaneously.

As the longwall face advances, no support remains for the overlying rock that was once above the coal seam. This lack of support results in the failure and ultimate caving of the roof material. Caving of immediate roof strata continues until the geological structural system stabilizes by reaching a new equilibrium. This caved material has a larger volume and different physical properties than the intact rock. Failure of the overlying rock mass results in vertical overburden loads transferring onto surrounding areas of higher stiffness, which includes solid coal ahead of the face, development pillars in headgate and tailgate entries, and compacted caved strata behind the face. The region of caved material is termed the "gob."

2.2. Ground Control around Longwall Mining Areas

The longwall mining system is extremely complex in terms of structural mechanics and involves significant stress redistributions when coal is mined. The system is dynamic during longwall face retreat with interactions occurring among high stiffness areas, such as solid coal ahead of the face and solid coal in development entry pillars, and relatively low stiffness areas such as shield supports in the face area and gob behind the face. These interactions result in high

stress concentrations at different locations around the mining area including set-up rooms, pillars in both headgate and tailgate development entries adjacent to the panel, and along the mining face (Figure 2.2). These high stress concentrations are called abutment loads. Distribution of loading around a longwall panel along cross-sections a-a, b-b, and c-c are shown in the figure and will be discussed in the following sections. The intensity of these abutment loads is dependent upon caving of the immediate roof and the vertical load carried by it as it gets compacted. Low stiffness gob areas do not carry much load, but as the gob is compacted, it can carry greater loads.

2.2.1. Gate Entries

As the solid coal is extracted, stresses are transferred onto gate entry pillars adjacent to the panel. These load transfers result in stress concentrations around mined-out regions and are referred to as abutment loading (Figure 2.2). The increased abutment loading, while extending to the second-row gate pillars, has substantially greater loading on the first row. The distance the abutment loading extends is defined by the equation (Peng and Chiang 1984):

$$D = 9.3\sqrt{H} \qquad \text{(Eq. 2.1)}$$

where D is horizontal distance affected by abutment loading (in feet), and

H is mining depth (in feet).

When evaluating stability of a longwall panel, T-junctions are of interest. T-junctions are the connection between gate (head or tail) entries (forming the side boundaries of the longwall panel) and the set-up rooms (forming the longwall face). As longwall mining commences in a panel, abutment loads that form in the set-up rooms and the adjacent gate entries cause a peak concentration of stresses in T-junction pillars. Another area of peak concentration will form in

gate entries on both sides of the longwall face and move with the face as it advances. This peak abutment is formed due to the interaction of front and side abutments.

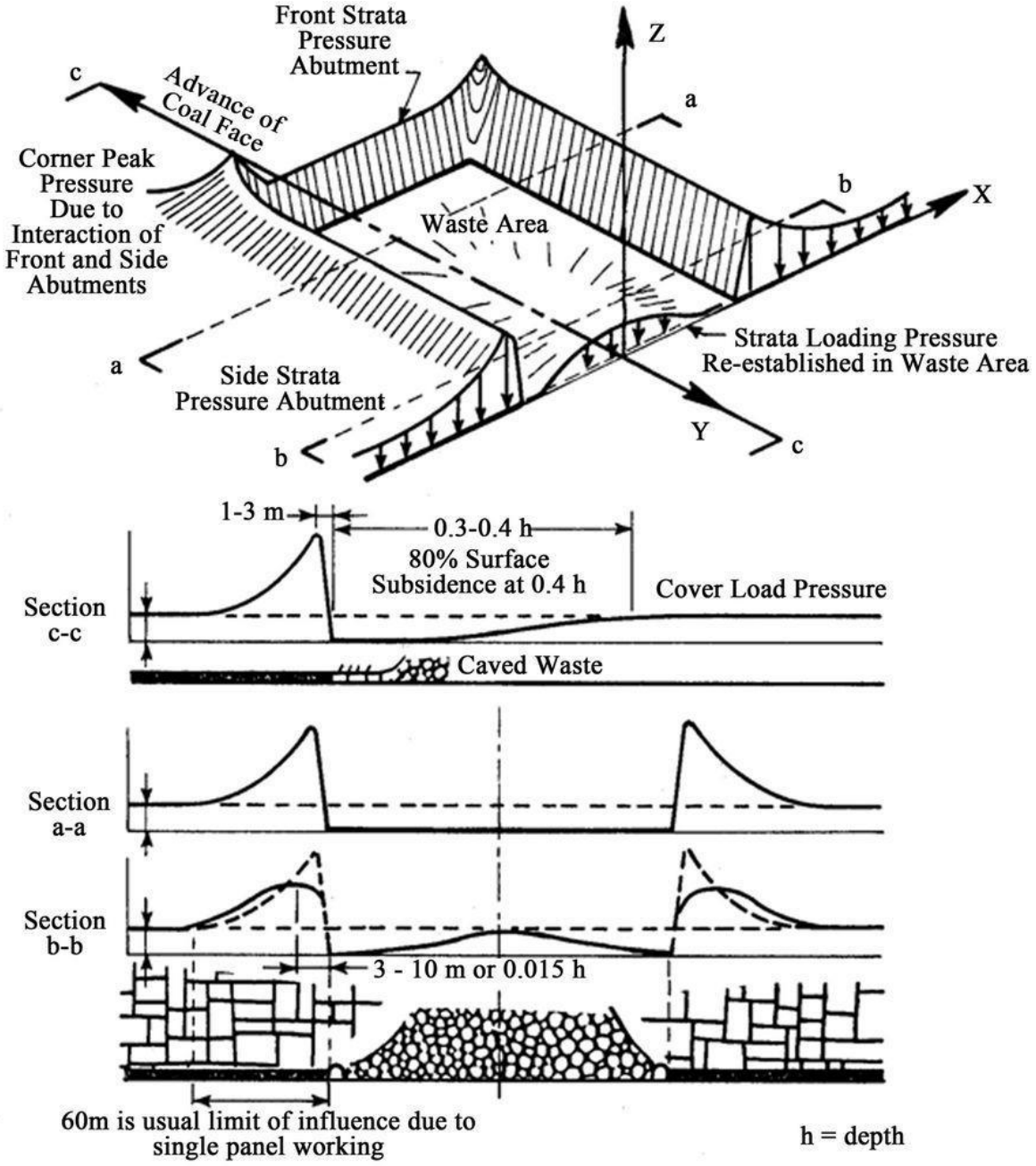

Figure 2.2: Distribution of loading about the longwall panel (Peng and Chiang, 1984).

2.2.2. Face Area

Ground control in the face area is critical to a productive longwall face. Stresses on longwall shields must remain within allowable limits to assure safety of workers and equipment. This area is of concern when mining around or through geological anomalies such as fault zones or dikes. These can significantly affect stress redistributions and displacements that occur. Slippage along a shear plane results in high displacements at the location where the face intersects a fault or dike zone and could potentially cause intense stress levels around the zone. The intensity of stress redistributions and displacements depends upon the angle of dip of the shear plane, the orientation of the shear plane with respect to the face, the curvilinear surface of the fault zone, and engineering properties of the material along the shear plane. An evaluation of the structural stability requires knowledge of these rock mass engineering properties.

As the longwall face advances, the immediate roof strata tend to fracture and fall into the mined-out area behind the face (Figure 2.3). Yielding or brittle fracturing also occurs ahead of the face as the coal is stiff enough for an abutment to form. Caving is a critical structural element of the longwall face, as it reduces pressures on shield supports in the face area and ahead of the face and allows gob to further compact and eventually take on some of the redistributed load. Studies by Deb *et al*. (2006), Trueman *et al*. (2011), and Medhurst and Reed (2005) show increased loading on shields near the center of the panel, with shields nearer to gate entries sharing abutment loading with pillars in those development entries.

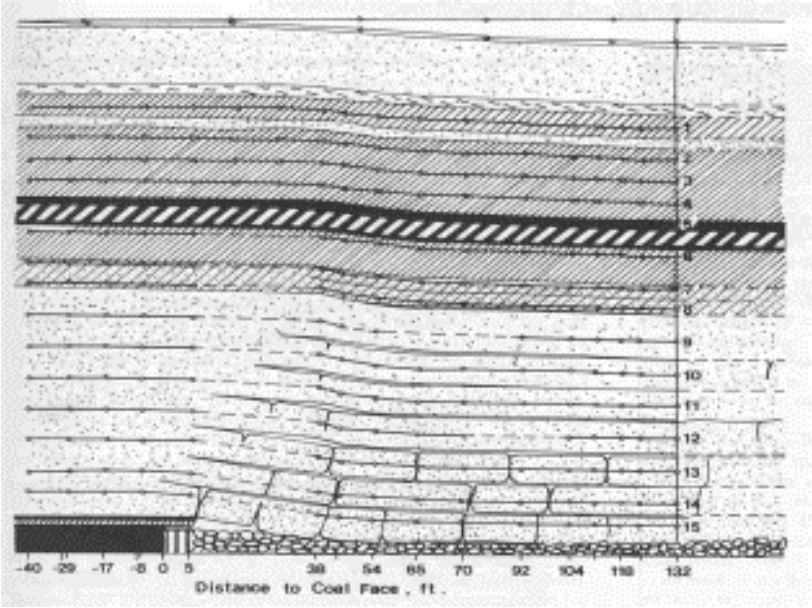

Figure 2.3: Caving and displacement of roof strata due to longwall face advance (Kolebaevna, 1968).

2.2.3 Gob Area

As mining progresses, abutment zones form around and adjacent to the gob area. Eventually, this caved gob material compacts to a point that it can carry load equal to pre-mining load (Figure 2.2 section c-c). Caving in longwall mining is dependent upon tensile and shear strength of caving materials. Since geology of the immediate roof and floor strata is highly variable in thickness and stiffness, caving of roof strata is generally non-uniform and occurs in zones (Figure 2.4). In regions where roof strata are thick, stiff, or of relatively high strength, it becomes difficult to induce caving at a desired distance behind the longwall face. Large blocks of hanging rock mass create a cantilever beam over longwall hydraulic shields in the face area and increase stresses in those areas (Figure 1.2). Increased stresses in these areas can result in productivity losses and potential damage to production equipment.

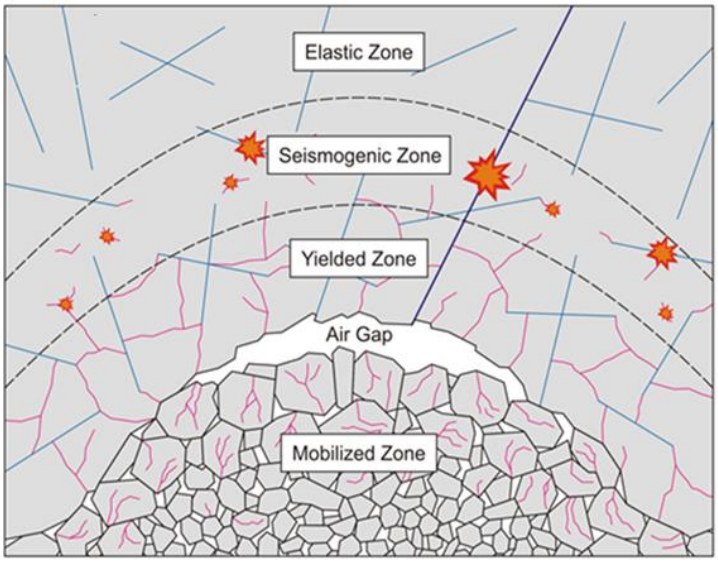

Figure 2.4: Five (5) zones associated with caving, proposed by Duplancic and Brady (1999).

The presence of geologic anomalies around a longwall face can affect stress and displacement distributions in many ways, including: 1) Increased loading on shield supports in the face area, 2) Increased or decreased caveability of immediate roof strata, 3) Increased loading on development pillars and around T-junctions, and 4) Increased loading and displacement rates due to the presence of one or more weak planes. This is discussed in more detail in Section 2.4.

2.3. Numerical Modeling of Longwall Mining Areas

Gale (2004) developed a two-dimensional (2D) numerical model of a longwall panel using FLAC. He determined rock fracture locations ahead of the advancing face as well as main modes of failure. Caving induced failure within the strata was very low. Gale studied the central portion of a longwall panel with a 2D vertical slice through the panel. The FLAC model was combined with a failure and fluid flow system for simulation of the rock mass. Failure of the rock mass was determined through the Mohr-Coulomb criterion. Hydraulic supports were

simulated by adding a hydraulic set and yield function into the model along the simulated face. Vertical loading was transferred through the shields by the inclusion of a canopy and base within the simulation. Longwall mining was simulated by gradually advancing the shield simulation in 3-foot (1 m) increments once the model removed that amount of coal ahead of the face. Creation of gob material was determined by both consolidation stiffness and post-failure criteria.

Verma and Deb (2008) used 2D plane strain in finite element models with a complete factorial design of six (6) factors in ANSYS to analyze interactions between hydraulic supports and surrounding strata for potential future deep longwall panels in India. These factors include mining depth, immediate roof modulus, immediate roof thickness, shield capacity, immediate roof friction angle, and whether the coal is hard or soft. Input values came from borehole samples collected across India. The yield criterion used was a three-dimensional (3D) pressure-dependent model, which estimates ultimate strength once a certain state of stress is reached. This work led to the development of statistical predictions for leg pressure, roof-to-floor convergence, and peak abutment loadings given the six (6) input factors.

Ozbay and Rozgonyi (2003) numerically modeled a 2-entry deep longwall system with FLAC. To model the coal accurately, they created an initial model of a quarter coal pillar (utilizing symmetry) and compared results to empirical formulas from Salamon and Munro (1967) and Bieniawski (1984). Coal element engineering property inputs were modified within the initial model until empirical formulas were well-reflected, then engineering inputs were placed within the full longwall model. In the analysis, they compared the Mohr-Coulomb failure criterion and the Mohr-Coulomb strain-softening criterion with field results. The strain-softening behavior more accurately matched field results. The model excavated coal in perimeter sections and then in longwall cuts allowing the model to equalize after each cut before

advancing again. Gob material was based on a 'compaction model' (Salamon, 1991) with non-linear elastic behavior where vertical stress rises exponentially with increasing strain.

Vakili *et al.* (2010) compared results of a finite difference model in FLAC3D and a Boundary Element model within MAP3D to the amount of surface subsidence and pillar stress expected within a typical longwall mining environment. Linear elastic modeling is preferred within MAP3D, so models studied within the software included either a gob material substitute or no gob material at all. The model with no gob material was the outlier of the MAP3D models. MAP3D was determined to be an acceptable modeling approach for the large-scale longwall environment, but has significant limitations for caving. An additional material to act as gob is not a necessity within FLAC3D. The study determined that, although FLAC3D requires more operator training, it is better suited for modeling environments where it is difficult to obtain *in situ* caving measurements (*i.e.*, stress levels within caved medium).

Shabanimashcool and Li (2012) evaluated the stability of gate entries in a Norwegian longwall coal mine using FLAC3D to create a numerical model. The rock mass in the numerical model undergoes strain-softening such that fracturing material undergoes unloading and reloading. Caved material consolidation is represented by the Double-Yield (DY) Constitutive Model within FLAC3D. The longwall is advanced in 16-foot (5-m) intervals. An algorithm was created to determine the thickness of the cave-in roof for the caving process behind the advancing longwall face. Empirical results show roof strata in gate entries are more affected by development of gate entries than by the active longwall mining process.

2.3.1 Development of Rock Mass Properties for Modeling

Solid earth material containing bedding planes, layered strata, and discontinuities such as joints, dikes, faults, shear zones, etc., is referred to as rock mass. Laboratory-determined

engineering properties for intact rock cores do not accurately represent rock mass values since they do not incorporate the complexity of the physical environment. Intact rock may behave isotropically or anisotropic orthotropically, depending upon the rock sample. However, a rock mass would be expected to have anisotropic properties. Rock mass engineering properties must be assessed as accurately as possible to analyze stability of jointed rock mass.

2.3.2 Intact Rock and Rock Mass Mechanical Behavior

An intact rock will not have fissures or joints within it. Strength behavior of intact rock is determined through strength tests in tension, shear, and compression loading at different confining stresses. Intact rock can refer to a lab specimen without discontinuities or an individual block of the rock mass (Figure 2.5). Examples of test results are given in Figure 2.6. Samples in an unconfined environment typically fail in a brittle manner with sudden loss of load carrying capacity (Figure 2.7). At higher confining stresses, the failure behavior shows a more gradual loss of load carrying capacity, and in some strain-hardening cases, even increased load carrying capacity (Figure 2.8). The failure behavior may be depicted as a failure envelope using the Mohr's circle approach shown in Figure 2.9(a). Connecting multiple circles with a tangent line represents the failure envelope. This generalized non-linear envelope (Figure 2.9(b)) can be idealized as a linear envelope (Figure 2.9(c)) with Equation 2.2:

$$S = So + [\sigma_n \tan(\varphi)]^a \qquad \text{Eq. (2.2)}$$

where S is the shear strength on a particular plane within a material,

σ_n is the normal stress acting on the plane,

φ represents the angle of internal friction of the material, and

So represents the cohesion of the material.

This equation is known as the Navier-Coulomb envelope. It is very often used as the first step in analysis. When a = 1, the Navier-Coulomb failure envelope is defined by:

$$S = So + \sigma_n \tan(\varphi) \qquad \text{Eq. (2.3)}$$

Figure 2.5: Example of an intact rock sample.

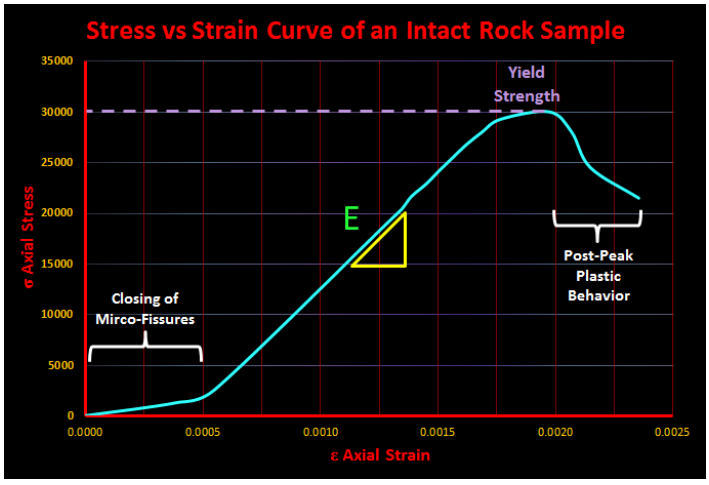

Figure 2.6: Example of a stress-strain curve for an intact rock sample.

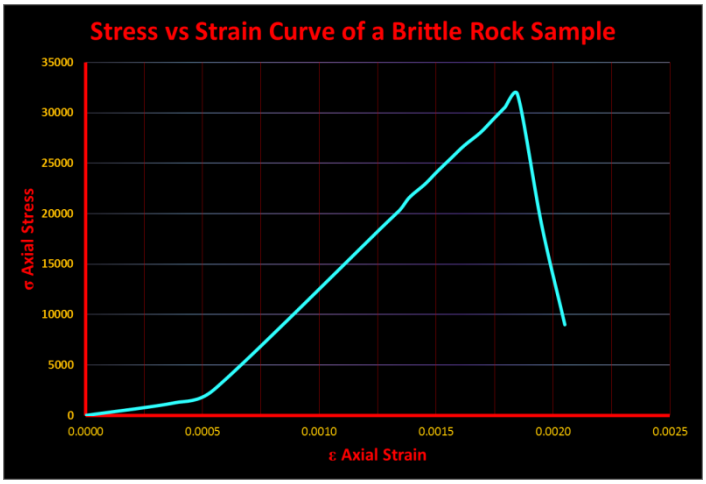

Figure 2.7: Stress-strain curve for a brittle material.

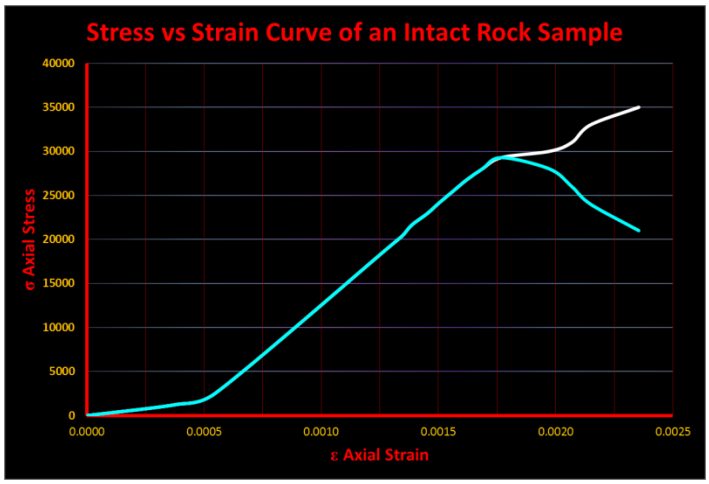

Figure 2.8: Stress strain curve for strain-hardening (upper) and strain-softening (lower) material.

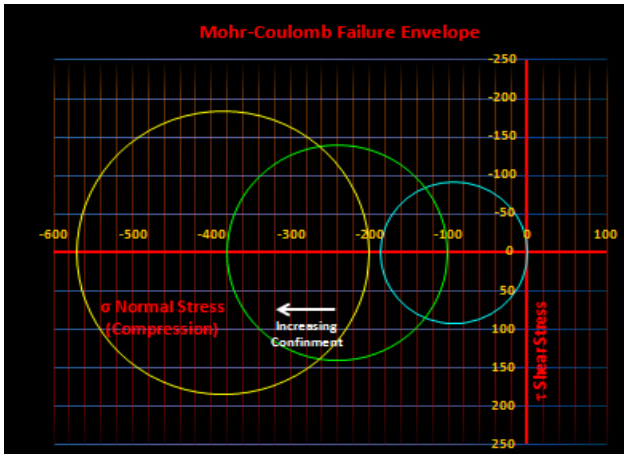

Figure 2.9(a): Mohr's circles from tri-axial testing.

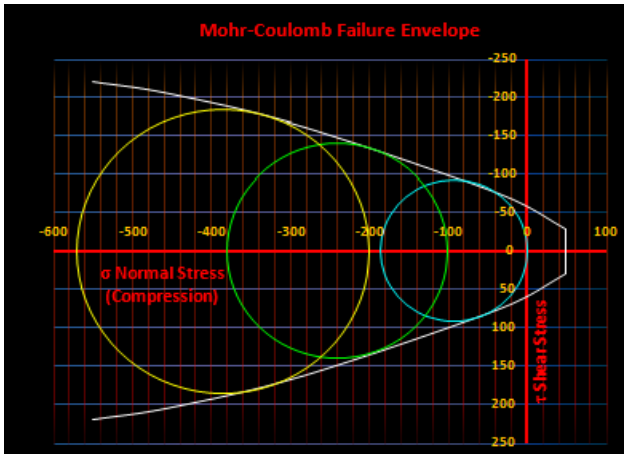

Figure 2.9(b): Generalized non-linear failure envelope.

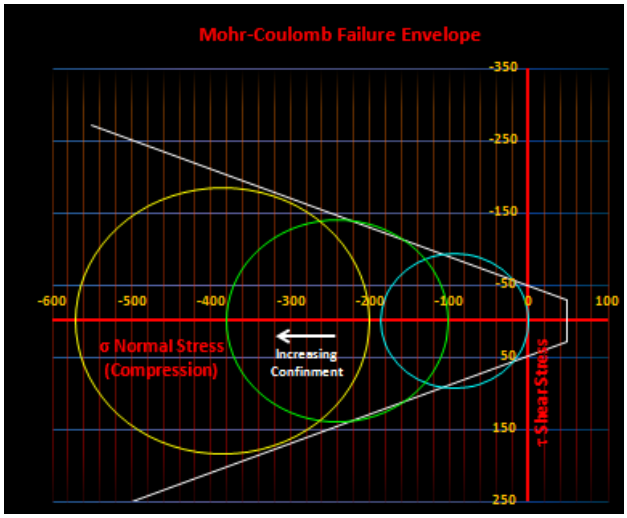

Figure 2.9(c): Idealized linear failure envelope if a = 1 (Navier-Coulomb).

To develop ground control practices that preserve stability in a jointed rock mass being mined, it is crucial to be as accurate as is possible in the determination of its mechanical properties. However, values for mechanical properties obtained through experimentation on intact rock samples are not always representative of the rock mass from whence they came. Because of scale and the sampling process used to obtain them, individual intact rock samples do not have the jointing seen in rock masses as a whole. Intact rock samples tend to behave mechanically in isotropic or orthotropic manners depending upon the rock sample whereas a rock mass may behave in more of an anisotropic fashion.

After intact rock properties are determined, that information can be used to estimate rock mass properties. The Geological Strength Index (GSI) is a crucial tool for this estimation (Hoek *et al*., 2005). Combined with intact rock engineering properties, the GSI enables approximation of the rock mass' Young's modulus, Poisson's ratio, as well as the rock mass yielding curve. The procedure for estimating rock mass behavior is discussed in depth in Chapter 3.

2.3.3 Hoek-Brown Failure Criterion

Unlike the Navier-Coulomb failure envelope, this criterion's yield surface is non-linear and can account for the decreasing incremental gain of strength with additional confinement (Figure 2.10). Its equation is given below:

$$\sigma_1{}' = \sigma_3{}' + \sigma_{ci}(m\frac{\sigma_3{}'}{\sigma_{ci}} + s)^a \qquad \text{Eq. (2.4)}$$

where $\sigma_1{}'$ and $\sigma_3{}'$ are major and minor effective principal stresses on the failure plane,

σ_{ci} is the uni-axial compressive strength for intact rock, and

m and *s* are material constants that are both dependent upon the GSI value.

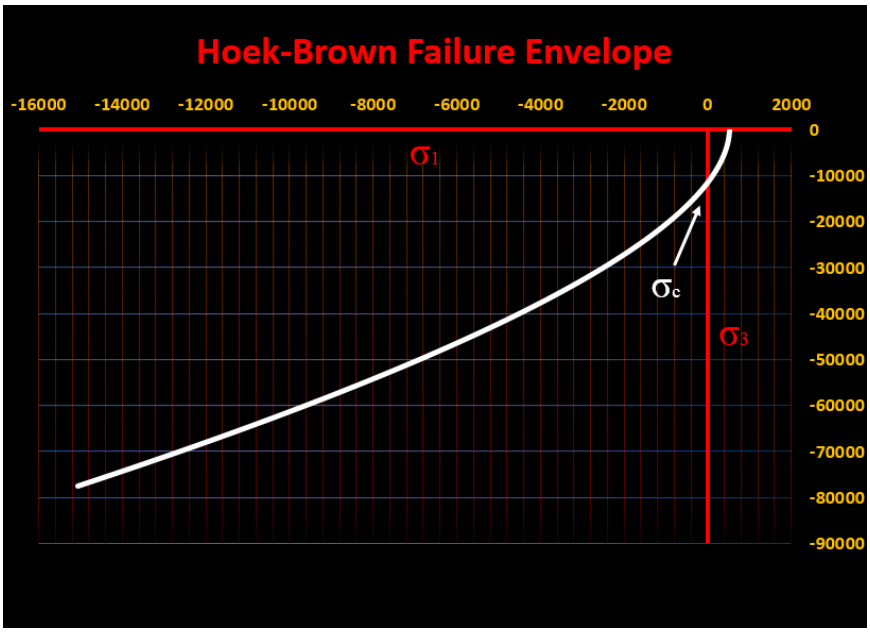

Figure 2.10: Hoek-Brown failure envelope for rock mass strength (σ_1 and σ_3 planes).

To obtain accurate values for use within the model, it is important to first develop inputs for the Hoek-Brown failure criterion that accurately depict non-linearity to appropriately account for the discontinuous nature of the rock mass. The yield surface for Hoek-Brown is dependent upon the GSI value, the disturbance factor D, the m_i value, and uni-axial compressive strength (UCS) parameters. The disturbance factor only comes into consideration when unnatural processes, such as drilling and blasting for tunneling, have been conducted. For this study, the disturbance factor is set to zero, since no blasting is involved. Displacements within the rock mass are in part derived from Young's modulus for intact rock using samples representative of the various types of strata in the mining environment. The GSI value is obtained by evaluating the lithology within the rock mass with respect to its structure and the surface weathering conditions of rock samples taken from the rock mass (Hoek *et al.*, 2005). This value ranges from 0 for extremely weathered and deformed geologic structures, to 100 for un-weathered and thick sedimentary beds (Table 2.1).

The Hoek-Brown criterion has an input, m_i, called the material constant (Hoek *et al*. 2002), which corresponds with the friction strength of the rock mass. Modifying this value to a lower amount will reduce the curvature of the Hoek-Brown failure envelope. The curve fitting parameter m_i can be accurately approximated by conducting tri-axial tests on the intact rock sample. This is in addition to the compressive strength value obtained through a series of UCS tests conducted on intact rock samples.

Table 2.1: Common GSI ranges for typical rock formations (Marinos and Hoek, 2000).

Rock Type	GSI value	Consideration
Sandstones	• Typical formation (45-90) • Tectonically brecciated (30-45)	• If weak interlayers, such as clayey or gypsiferous cement, are involved, GSI values may lower.
Silstones, clayshales	• Bedded, foliated, fractured (45-20) • Sheared, brecciated (25-5)	• GSI is not applicable in homogeneous rock with no formation of discontinuities. • If they are present as thin interlayers between stronger rocks, a downgrading of the rock mass towards the right part of the chart should be considered.
Limestones	• Massive (90-45) • Thin bedded (55-35) • Brecciated (45-30)	• During folding thin bedded layers result in differential movement lowering the GSI.

It is imperative for geotechnical analysis to ascertain mechanical parameters for the rock mass so that modeling behavior reflects what is observed in the mining environment. The key input parameters required to correctly model a longwall environment numerically include GSI, m_i (intrinsic material property), UCS of intact rock, elastic moduli, and Hoek-Brown residual parameters. The intrinsic heterogeneous distribution of discontinuities within the rock mass makes it difficult to determine these parameters. Mechanical properties of the rock mass for this

study were determined from laboratory testing on core samples, tests in the field, visual observations, and past experience. Testing on samples of caved material is impractical and unfeasible. Validating correct parameter values was performed by comparing model results to those ascertained in the field.

2.3.4. Mohr-Coulomb Failure Criterion for Intact Rock

For this study, tension will be treated as positive and the relationship between principal stresses will be: $\sigma_1 \geq \sigma_2 \geq \sigma_3$. This criterion is specifically for brittle materials under compression, such as rock and concrete. A Mohr-Coulomb analysis examines the state of stress along mutually orthogonal planes and analyzes every possible rotation of those planes to estimate if failure may occur within the material. Every possible orientation can be plotted in 3D space or in 2D with each plane represented by an individual Mohr's circle (Figure 2.11).

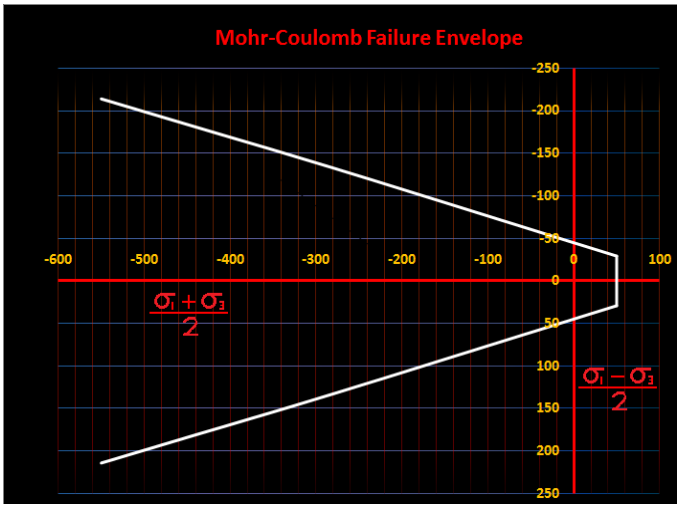

Figure 2.11: Envelope in Mohr-space using σ_1 and σ_3 planes.

The angle of internal friction and cohesion inputs are required for the development of a linear yield surface that is dependent upon confining pressure. If the yield surface, termed the failure envelope, is breached, then the material is expected to fail in the shear mode. However, tension failure is possible if the region of the failure envelope termed the tension cut-off is breached. The location where the failure envelope is breached by a state of stress can be related to the location and/or orientation of a failure surface in an intact rock given the orientation of stresses applied on the rock. At higher confining pressures, the angle of internal friction is seen to decrease during experiments, but the criterion sets the angle as a constant. The vertical axis intercept is the location of no confinement and is defined as the cohesion of the material. The angle of internal friction determines the steepness of the linear yield surface. If the angle of internal friction is non-zero, the material will be assumed to gain strength through additional confinement. When unconfined, the material can only fail if its cohesion is surpassed.

2.4. Stress Redistribution and Mechanisms of Failure

A dynamic mining environment with changing geometries will result in redistributions of stress fields. During mining of headgate and tailgate development entries, rock once acting as confining material is removed. Without this confinement, the stiffness of the rock immediately surrounding these entries is reduced and loading in these areas will redistribute to stiffer, more confined rock masses. Through this redistribution, parts of the rock mass surrounding the entry may experience tension depending upon the magnitude and orientations of principal stress fields and the orientation of entries. Failure in rocks will occur either in tensile or shearing modes. If the difference in principal stresses becomes great enough, then failure in the shear mode is possible depending on the greatest principal stress.

2.5. Numerical Modeling of Geologic Anomalies and Faults in Longwall Mining

A rock mass has numerous discontinuities including sets of joints, bedding planes resulting from sedimentary deposition, and in some instances, major shear planes. Behavior of a rock mass differs from intact rock in how deformation occurs. Intact rock deforms through strain and shape distortion. A rock mass, on the other hand, can deform in the same manner, but also through movement along numerous discontinuous surfaces where sliding could occur. To account for this behavior, ubiquitous joints can be included into models, particularly for linear features such as fault planes.

Ubiquitous Joint Rock Mass (UJRM) is a methodology for applying a weak plane or discontinuity to a rock mass simulated by a continuum in numerical modeling. UJRM weak plane mechanics is defined by the Mohr-Coulomb failure criterion with the tension cutoff along a weak plane (ITASCA, 2012). Many previous researchers have employed and verified this technique, including Lietner *et al*. (2006), Sainsbury *et al*. (2008), Sainsbury and Sainsbury (2017), Clark (2006), Board *et al*. (1996), and Chiu *et al*. (2013). While this methodology presents a highly useful tool, it also has limitations that must be considered. There are several important joints-related factors that UJRM does not consider including joint spacing, stiffness, and geometry (Sainsbury 2012). Implementation of a ubiquitous joint plane or surface in finite element models requires six (6) inputs: strike, dip, dilation, cohesion, friction angle, and tensile strength. To generate realistic modeling results, calibration of UJRM is usually required.

Geological discontinuities influence both failure initiation as well as progression. Weakness planes along the discontinuity shape the extent of failures. It is critical that the panel and entries within the panel be oriented with respect to the discontinuity and lateral stresses to lower peak stress levels in the mining environment. Panel design must take into account

interactions between stresses, discontinuity surfaces, and the configuration of mining entries. Stresses and deformation are also subject to variance in geo-mechanical properties of changing strata and the failure of weaker lithologies such as coal and claystone.

Gale (2005) studied geological discontinuities, reinforcement performance of roof bolts, and ground behavior in coal mines. His work showed how stresses redirect over the immediate roof of an entry before significant deformations occur (Figure 2.12) so that geological discontinuities and bedding plane shear that form at the beginning of the deformation process were enough to cause significant stress redistribution, even when displacements and observed deformations were found to be low.

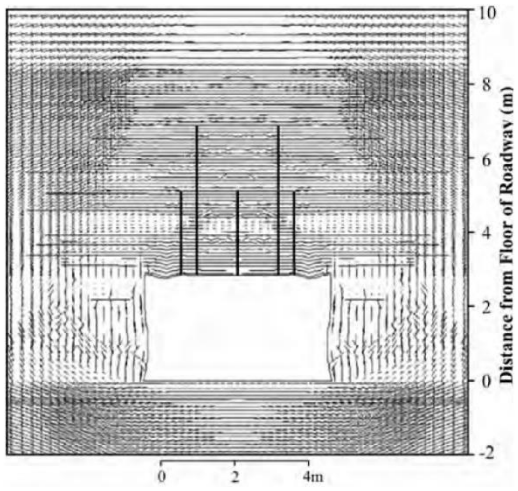

Figure 2.12: Stress redirection about the roadway caused by localized rock failure and subsequent changes in bulk material properties during roadway development (Gale, 2005).

2.5.1. Difficulties Associated with Modeling Geologic Anomalies Numerically

Modeling of geologic anomalies can be a challenging task. Mine exploration using vertical boreholes reveals only limited information about the geometry, engineering properties,

and anomalies within a given geology. Therefore, reasonable approximations must be made for the location and extent of anomalies within a model. Modeling mechanical behavior of an anomaly can be aided with information gathered from control points installed in active mining environments. Differences in behavior between control points around geologic anomalies and those in standard geologic areas show the influence and magnitude of an anomaly. This comparative information helps to ensure that input parameters are within acceptable tolerances.

2.6. Fault Modeling Using UJRM Technique

Abbasi *et al*. (2014) developed analytical tools to quantify displacements around a fault zone as a longwall face advanced towards it. They used FLAC3D software to generate a 3D model of a southern Illinois longwall panel intersected by a fault zone. The fault zone was simulated using the UJRM method. The model used the Hoek-Brown method with GSI inputs for the failure criteria of the strata, and the Mohr-Coulomb failure criteria for the fault zone. GSI estimates were used for different lithologic units to develop their rock mass engineering properties that were used in numerical models. Caved gob material engineering behavior was approximated by an empirically distributed loading function behind the advancing face. This approach led to roof-to-floor convergence results in several areas that were only 15-20% different than corresponding values measured in the field. Results showed that development entries intersected by the fault start to experience the deformational effect of the fault when the longwall face was 230 feet (70 m) away. Model observations were corroborated in the field through convergence measurements. Supplementary roof supports were used in gate development entries that allowed the company to mine successfully through the fault without loss of production or accident.

2.7. Modeling of Caved Gob in Longwall Mining

Since the start of mining methods that employ caving, researchers have been attempting to accurately predict caving behavior and propagation. Thin *et al*. (1993) used the DY model for gob material. Within FLAC, the DY model uses a strain-stiffening relationship in the gob where vertical stress within gob material is used to calculate a vertical strain. They found that the thicker the overlying beds above the coal, the greater distance initial loading reaches into the gob, and that this distance shortened with increasing depth.

Sainsbury (2010) created a numerical caving model with the Mohr-Coulomb failure criteria. A fully fractured and bulked cave material was simulated in the undercut regions of the numerical model. The study examined the sensitivity to caveability of the rock mass in the early stages of production. The study found that increased bulking occurred at the edge of the caved region, and that the rate of cave propagation increased with the depth of mining.

2.8. Experimental Approaches for Assessment of Caving

There are three (3) applicable methods that are useful in predicting caving behavior, each with its own strengths and weaknesses, as discussed next. The research reported in this thesis utilized all three (3) approaches.

2.8.1 Analytical Approach

It has been previously suggested by researchers that simplistic analytical volume relationships could be utilized in estimating caved material bulking and caving propagation (Beck *et al*., 2006). This approach makes the assumptions that propagation is in the vertical direction, at a constant rate, and that initiation of caving will always occur.

The analytical approach has been found to be inaccurate (Sainsbury, 2012) possibly due to geomechanical rock mass properties being ignored during calculations.

2.8.2 Empircal Approach

There have been several empirical approaches proposed to approximate caveability in the mining environment. Laubscher (1994) worked on a collection of cases from past caving practices in South Africa's block-cave mining of kimberlite pipes. This work characterized the extent of caving into three (3) distinct possibilities. Mining can result in: 1) no caving, 2) a transitional state of caving whereby there is cave initiation, but a lack of significant cave propagation, and 3) complete caving.

In more recent times, several researchers have obtained results that differ considerably from data presented by Laubscher. Kimberlite pipes are a weaker rock originating from deep subterranean eruptions, so data collected by Laubscher represented a weaker rock mass than is generally found in mining environments. Research to predict caveability for harder rock masses produced another prediction tool for caveability (Trueman *et al*.; 2003).

Both of these methods were developed based on collected sets of data, which causes some limitations. They lack sufficient information to estimate both rates of caving and zones of mechanical behavior in a caving environment.

2.8.3 Numerical Approach

Many numerical modeling techniques are available to researchers attempting to analyze geotechnical environment. These techniques include Boundary Element, Distinct Element, Finite Difference, Finite Element, and other numerical techniques that combine some or all of the aforementioned techniques. While any analysis program can be used to examine the

geotechnical environment, the critical aspect of analysis is the methodology incorporated within the study.

Geotechnical material presents researchers with a substantial challenge. Unlike man-made materials that are manufactured, natural material is extraordinarily complex with micro-fissures and varying arrangements of microscopic minerals. It is not possible using today's computers to model materials down to this scale while still trying to evaluate a macro-level environment such as longwall mining. Therefore, approximations must be made by researchers to define inputs such that reality is represented as well as possible. An international study on caving environments by Pierce and Lorig (1998) illustrates an enhanced methodology whereby sequential undercuts are simulated and a user-defined function can modify material properties based on plasticity state and strain. By analyzing 3D states of stress that surround the undercut, a point of self-sustaining instability can be determined.

CHAPTER 3

MODEL DEVELOPMENT AND FIELD MONITORING STUDIES

3.1 Description of Physical Problem and Mine Environment

The overarching purpose of this study is to apply analytical tools to quantify and determine incremental stresses and deformations that occur around a fault as longwall mining progresses toward, through, and away from it. Fault planes embody spatial discontinuities. They disturb the surrounding rock mass causing it to degrade. Both the weak fault plane and the surrounding degraded rock mass have different engineering properties than the adjoining undisturbed rock mass. Areas around the fault can undergo large displacements relative to the rock mass with the potential effect of shedding stresses onto the adjoining rock mass. Thus, when mining intersects a fault plane, mine operators must be aware of an increase in loading on some portions of coal ribs along an entry and on the caved or falling rock from the roof. The redistribution of stresses during mining around fault zones has the potential to result in additional deformations, rigid-body displacements, and rotations.

Another region of differing stiffness is the caved gob after longwall mining has removed coal from an area. It is here that stress redistributions are caused by varying stiffnesses of the spatially distributed gob area and by coal pillar failures. Displacements in these regions are affected by the orientation of the fault, the extent of the disturbed rock mass, properties of the fault plane, the dynamic stress field resulting from a retreating longwall face, properties of the spatially distributed gob area, and soft floor material.

The case study developed in this thesis is for a mine in southeastern Illinois extracting coal from the Herrin No. 6 coal seam at a depth of about 600 feet (180 m). The immediate roof

consisted of black shale, limestone, dark shale, coal riders, and sandy shale. The floor stratum is weak claystone underlain by shale rock. The mine uses the longwall mining method with panels generally oriented in the east-west direction. Gate entry widths are 19 feet (5.7 m) and crosscut spacing (center-to-center distance) ranges from 100 to 140 feet (30 to 45 m). T-junction pillar dimensions are 80 feet by 80 feet (24 m by 24 m).

The case study mine encountered both major and minor faults and grabens. Faults in the study had a general strike and dip of N30°W and about 60°, respectively. Ground movement monitoring points for the first fault zone encountered when mining gate entries are shown in Figure 3.1. A second fault zone was encountered as gate entry development continued. The main fault had a down-throw displacement toward the east of 3 feet (1 m) as depicted in Figure 3.2. This fault extended into the set-up rooms on the tailgate side.

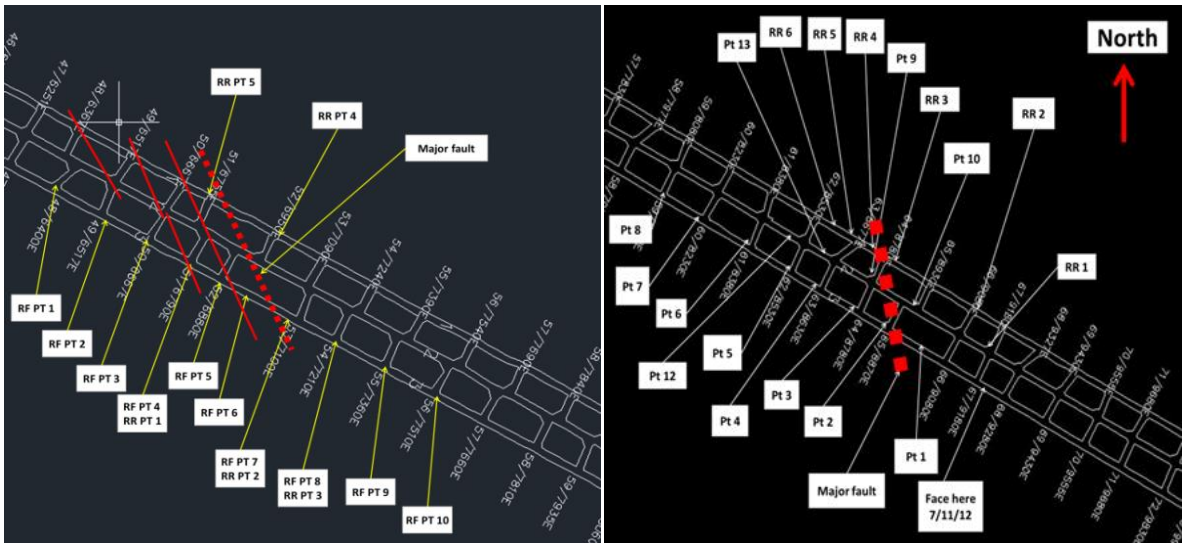

(a) (b)

Figure 3.1: Fault and ground movement monitoring station locations in: **(a)** Headgate of case study panel, and **(b)** Headgate of adjoining longwall panel for first fault zone.

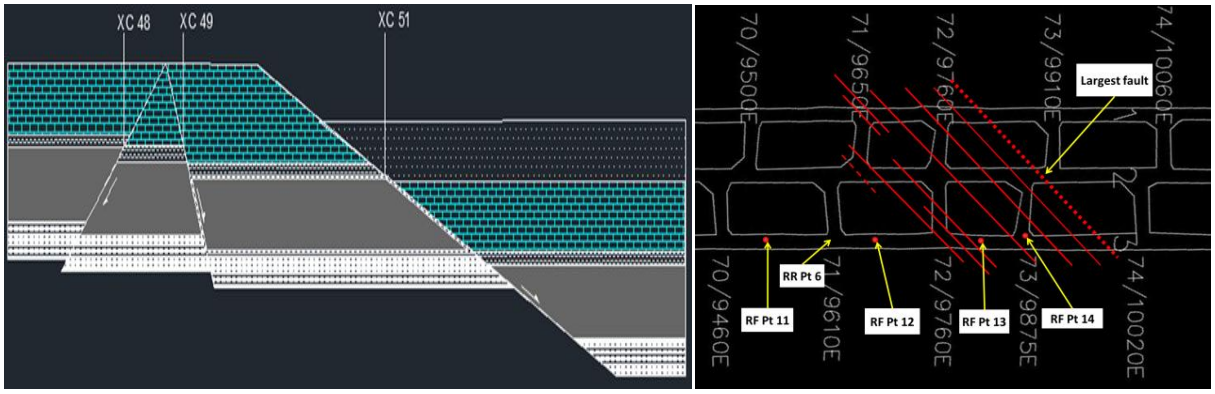

(a) (b)

Figure 3.2: (a) Cross-sectional view of second fault/graben area in headgate return entry of case study panel, and **(b)** Plan view of same area showing ground movement monitoring locations.

3.2 Identification of Modeling Areas

A plan view of the longwall panel's set-up rooms, tailgate entries, and headgate entries is shown in Figure 3.3 with pillar dimensions indicated. Designed pillar dimensions are standardized at 80 feet (24 m), 120 feet (36 m), and 140 feet (42 m). Entries in set-up rooms and headgate and tailgate sections are supported using 6-foot (1.8-m) long, #6 rebar, fully-grouted passive bolts as primary support. Areas with highly variable roof lithologies use steel channels in conjunction with fully grouted bolts. Set-up rooms use trusses as secondary support at 10-foot (3-m) intervals. Mining thickness is about 6.0 feet (1.8 m).

Figure 3.3: Layout and dimensions of the modeled mining environment.

A plan view of the modeled region at the coal elevation is shown in Figure 3.4 with the fault highlighted. The figure represents the modeled state immediately following development of set-up rooms and gate entries. As can be seen, the fault intersects the longwall face from the start of mining up to the fourth chain pillar in the headgate entry. Several gate entry pillars are intercepted by the fault as well.

For the sake of computing efficiency, only the portion of the longwall panel intersected by the fault was modeled. The other (symmetrical) half of the panel was not included. By limiting focus on this region, the density of elements within the model could be increased. Model boundaries were kept 150 feet (45 m) away from any entries so that intersections of fault and entry would not be distorted by being located at the model boundary.

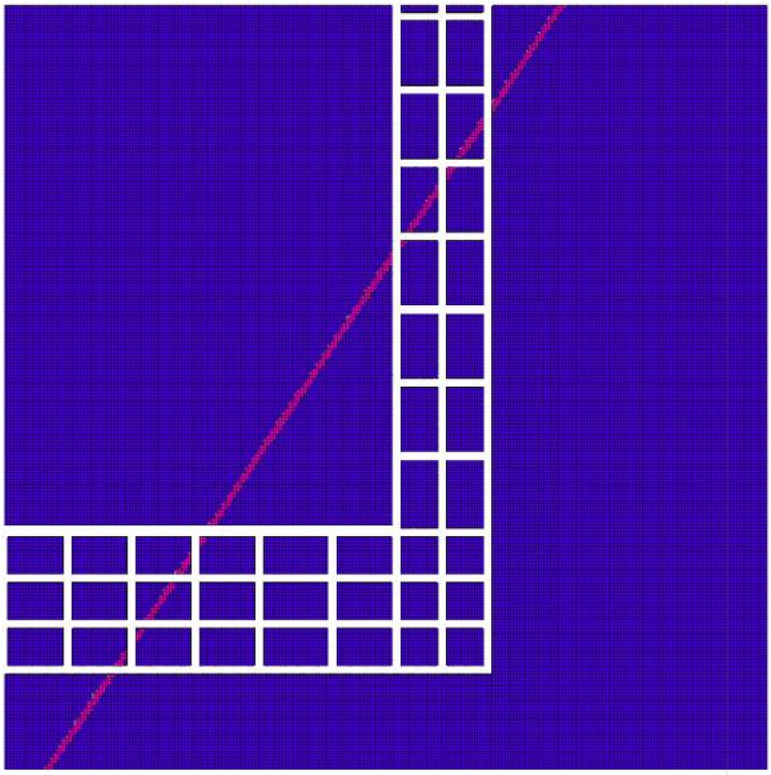

Figure 3.4: Area modeled at the coal seam level with fault zone highlighted.

3.2.1. Development of Numerical Models

Models were developed using FLAC3D, a structural analysis software developed by the Itasca Consulting Group that is used extensively for geotechnical modeling of geologic problems that involve highly complex geometries, and linear as well as non-linear behavior. FLAC3D is based on the finite difference computational scheme. Two (2) separate models were developed: Model 1 of mine workings without a fault, and Model 2 of mine workings with a fault. Both models were analyzed using linear properties and rock mass properties computed from intact rock properties using the well-established Hoek-Brown failure criterion (Hoek *et al*., 2002). The fault was modeled as a Ubiquitous Jointed Rock Mass (UJRM) in a well-defined spatial plane with weak rock mass surrounding the plane as discussed in Chapter 2 (Section 2.5).

3.2.2. Immediate Roof and Floor Lithology of Models

Each distinct geologic unit such as sandstone or limestone in the sedimentary deposit is known as a lithologic unit. Attributes of each lithologic unit change spatially. It is impossible to model continuous variability in these attributes. Therefore, average attributes of lithologic units above and below the coal seam, and the coal seam itself, were modeled in a columnar section as described in Table 3.1. The base of the model is 43 feet (13 m) of shale. Layers above this shale from bottom to top are as follows:

- 3 feet (1 m) of weak limestone,
- 3 feet (1 m) of gray shale,
- 2 feet (0.7 m) of shale,
- 1 foot (0.3 m) of claystone,
- 6 feet (2 m) of coal,
- 2 feet (0.6 m) of black shale,
- 2 feet (0.6 m) of gray shale,
- 2 feet (0.7 m) of weak limestone,
- 3 feet (1 m) of weak shale, and
- 3 feet (1m) of limestone.

At the top of the model is 39 feet (12 m) of shale.

Table 3.1: Engineering properties of rock strata used in modeling.

	Strata	Location (ft.)	Location (m.)	Bulk Modulus, K (psi)		Shear Modulus, G (psi)		GSI	m_i	Density (pcf)	σ_{ci} (psi)	E_i (psi)
Strata, Intact Rock Values, and GSI Inputs	Shale	72 - 112	22 - 34	217000		118000		70	10	155	6000	500000
	Good Limestone	69 - 72	21 - 22	365000		297000		95	15	165	12000	1326000
	Weak Shale	66 - 69	20 - 21	83000		28000		65	9	150	5500	700000
	Weak Limestone	63 - 66	19.3 - 20	259000		178000		80	13	160	7500	850000
	Gray Shale	61 - 63	18.6 - 19.3	217000		118000		70	9	150	5500	750000
	Black Shale	59 - 61	18 - 18.6	194000		146000		65	9	140	4000	650000
	Coal	53 - 59	16 - 18	139000		57000		62	8	80	3500	400000
	Clay Stone	52 - 53	15.7 - 16	33000		11000		58	50	135	1200	250000
	Shale	50 - 52	15 - 15.7	217000		118000		70	10	155	6000	500000
	Gray Shale	46 - 50	14 - 15	217000		118000		70	9	150	5500	750000
	Weak Limestone	43 - 46	13 - 14	259000		178000		80	13	160	7500	850000
	Shale	0 - 43	0 - 13	217000		118000		70	10	155	6000	500000
Derived Rock Mass Properties	Strata	E_{rm} (psi)	m_b	s	a	v	σ_c (psi)	σ'_{3n} (psi)	Φ'	c' (psi)	Bulk Modulus, K (psi)	Shear Modulus, G (psi)
	Shale	367000	3.4	0.036	0.501	0.215	1130	0.00006	32.1	570	215000	151000
	Good Limestone	1299000	12.5	0.574	0.5	0.1775	9080	0.00003	47.5	1710	672000	551000
	Weak Shale	443000	2.6	0.02	0.502	0.2225	780	0.00007	29.1	490	265000	181000
	Weak Limestone	748000	6.4	0.108	0.501	0.2	2470	0.00005	39.1	810	416000	312000
	Gray Shale	550000	3.1	0.036	0.501	0.215	1030	0.00007	30.5	540	322000	226000
	Black Shale	410000	2.6	0.02	0.502	0.2225	570	0.00009	26.6	430	247000	168000
	Coal	226000	2.1	0.015	0.502	0.227	420	0.0001	23.8	380	138000	93000
	Clay Stone	118000	11.2	0.009	0.503	0.233	120	0.0003	29	460	74000	48000
	Shale	367000	3.4	0.036	0.501	0.215	1130	0.00006	32.1	570	215000	151000
	Gray Shale	550000	3.1	0.036	0.501	0.215	1030	0.00007	30.5	540	322000	226000
	Weak Limestone	748000	6.4	0.108	0.501	0.2	2470	0.00005	39.1	810	416000	312000
	Shale	367000	3.4	0.036	0.501	0.215	1130	0.00006	32.1	570	215000	151000
Ubiquitous Joint Rock Mass Properties	Strata	E_{rm} (psi)	m_b	s		a		v	σ_c (psi)	σ'_{3n} (psi)	Φ'	c' (psi)
	Shale	183000	1.9	0.005		0.505		0.2405	440	0.00006	27.3	430
	Good Limestone	996000	5.3	0.04		0.501		0.2135	2380	0.00003	41.7	840
	Weak Shale	202000	1.5	0.003		0.506		0.2465	320	0.00007	24.7	380
	Weak Limestone	442000	3.1	0.012		0.503		0.23	800	0.00005	33.3	570
	Gray Shale	275000	1.7	0.005		0.505		0.2405	390	0.00007	25.8	410
	Black Shale	188000	1.5	0.003		0.506		0.2465	230	0.00009	22.3	340
	Coal	102000	1.2	0.003		0.507		0.2495	170	0.0001	20	3000
	Clay Stone	52000	6.8	0.002		0.509		0.254	60	0.0003	25.3	380
	Shale	183000	1.9	0.005		0.505		0.2405	440	0.00006	27.3	430
	Gray Shale	275000	1.7	0.005		0.505		0.2405	390	0.00007	25.8	410
	Weak Limestone	442000	3.1	0.012		0.503		0.23	800	0.00005	33.3	570
	Shale	183000	1.9	0.005		0.505		0.2405	440	0.00006	27.3	430

3.3 Model and Engineering Properties Development

Two (2) models were generated for analysis. The difference between them was UJRM inclusion. To estimate effects of UJRM zones on stress and displacement within a macro-system, a base case without any discontinuities was needed. This base case model was termed Model 1. Then, a second elastic model was created to be identical to the first, but with UJRM zones included establishing the effect of a geological discontinuity. This model was termed Model 2. A comparison of results from these two (2) elastic models is discussed in Chapter 4. Uniform strata thickness was preserved for both models.

3.3.1 Model Size

Both models were 1640 feet (500 m) long, 1640 feet (500 m) wide, and 110 feet (34 m) high. Lithological units 50 feet (15 m) above and 50 feet (15 m) below the coal seam were modeled to allow a reasonable distance for stress redistributions to equilibrate. A uniform vertical stress of 550 psi (3.8 MPa) was applied on the upper boundary of the model to simulate the remaining overburden. This was necessary to allow for large face advance distances and adequate solid coal on model peripheries so that stress levels would return to their virgin state. Elements created in both models were a uniform 6-foot × 6-foot (2-m × 2-m) size horizontally, but varied in thickness vertically. Weak claystone floor elements were 1 foot (0.3 m) in thickness. Coal seam elements were 1.5 feet (0.5 m) in thickness. Black shale in the immediate roof was 2 feet (0.6 m) in vertical thickness. Models were constructed to be rectangular prisms 250 elements long, 250 elements wide, and 38 elements thick for a total of 2,375,000 elements.

An interface was included between the claystone unit and the coal layer to prevent elements in the immediate roof layer above the coal seam from penetrating elements into the coal seam floor. When coal elements are removed (*i.e.*, simulating mining), the roof deforms towards the floor and there must be an impermeable barrier to keep roof elements from penetrating into the floor. This interface was assigned properties to prevent penetration of the roof and floor elements, but to minimize it interfering with gob loading behavior. Interface properties had to be calibrated via an iterative process to achieve this balance.

3.3.2 Engineering Properties of Intact Rocks

The engineering properties used during this study were derived from experience and a previous study at the cooperating mine by Chugh *et al*. (2013). The previous study examined the

properties of strata at and around the fault zone. Bulk samples and cores were tested and average property values for the strata were determined.

3.3.3 Additional Engineering Properties

Elastic engineering properties, such as Geological Strength Index (GSI), material constant m_i, intact rock uni-axial compressive strength σ_{ci}, and intact rock Young's modulus E_i, for different lithologic units contained in the modeled rock mass are given in Table 3.1. These were based on previous studies conducted at Southern Illinois University Carbondale at the cooperating mine.

Development of Hoek-Brown rock mass parameters for non-linear analysis was more complex. Hoek-Brown failure criterion relates principal stresses σ_1 and σ_3 (Equation 3.1). These were calculated from estimated values of the GSI for each lithologic unit.

The rock mass Young's modulus for each layer was developed using Equation 3.2. In this equation, D, the disturbance factor, was always assigned a value of 0, as it applies generally to blasted rock. Rock mass elastic modulus and Poisson's ratio estimates were used to calculate rock mass bulk and shear moduli. Material constants m_b, s, and a, can be calculated from Equations 3.3, 3.4, and 3.5, which are based on the GSI value. Poisson's ratio for each strata was calculated from Equation 3.6.

Most researchers are more familiar with the Mohr-Coulomb failure criterion, which relates normal stress and shear stress on a plane. To approximate the equivalent Mohr-Coulomb cohesion and angle of internal friction values, it is important to first know the value for σ_{3n}or the confining stress. Equation 3.7 is used to determine this value. It is dependent upon the value σ'_{3max}, where $\sigma'_{3max}$is the highest confining stress for which Hoek-Brown and Mohr-Coulomb

relationships are to be examined. A value of 2500 psi (17 MPa) was chosen for σ'_{3max}. This is a vertical stress concentration factor of 4.5, which is unlikely to be achieved except for at the corner of pillars. Obtaining the equivalent Mohr-Coulomb relationship over the span of σ'_{3max} for each lithologic unit requires constants m_b, s, and a, as well as the intact strength of material,σ'_{ci}, and the value of σ_{3n}. The complex equations for cohesion and angle of internal friction are shown in Equations 3.8 and 3.9.

$$\sigma_1 = \sigma_3 + C_o\left(m_b \frac{\sigma_3}{C_o} + S\right)^a \quad \text{Eq. (3.1)}$$

$$E_{rm} = E_i\left(0.02 + \frac{1-D/2}{1+e^{\left(\frac{60+15D-GSI}{11}\right)}}\right) \quad \text{Eq. (3.2)}$$

$$m_b = m_i \exp\left(\frac{GSI-100}{28-14D}\right) \quad \text{Eq. (3.3)}$$

$$s = \exp\left(\frac{GSI-100}{9-3D}\right) \quad \text{Eq. (3.4)}$$

$$a = \frac{1}{2} + \frac{1}{6}\left(e^{-\frac{GSI}{15}} + e^{-\frac{20}{3}}\right) \quad \text{Eq. (3.5)}$$

$$v = 0.32 - 0.0015 x GSI \quad \text{Eq. (3.6)}$$

$$\sigma_{3n} = \frac{\sigma'_{3max}}{\sigma_{ci}} \quad \text{Eq. (3.7)}$$

$$c' = \frac{\sigma_{ci}\left[(1+2a)s + (1-a)m_b\sigma'_{3n}\right](s+m_b\sigma'_{3n})^{a-1}}{(1+a)(2+a)\sqrt{1+\left(6am_b(s+m_b\sigma'_{3n})^{a-1}\right)/((1+a)(2+a))}} \quad \text{Eq. (3.8)}$$

$$\phi' = \sin^{-1}\left[\frac{6am_b(s+m_b\sigma'_{3n})^{a-1}}{2(1+a)(2+a)+6am_b(s+m_b\sigma'_{3n})^{a-1}}\right] \quad \text{Eq. (3.9)}$$

3.3.4 Development of Strata Properties Along the Fault

As previously mentioned, the fault was modeled as a UJRM plane. This plane was developed with a dip of approximately 35 degrees off the horizontal. The dip went downward along the positive y-direction and negative x-direction. FLAC3D allows estimated engineering properties of the fault to be assigned not only to the UJRM plane, but also to the rock mass adjoining the fault plane defined by the user. Engineering properties along the UJRM and adjoining the UJRM for different lithologic units were developed in the manner described previously. The same method and values were applied, and except for the GSI value, all other constants were preserved. The GSI value of each lithologic unit was reduced to represent the weaker material along the fault plane. UJRM zones within models were approximately 10 feet (3 m) in width.

3.3.5 Modeling of Face Advance

Coal seam elements were always 6-ft × 6-ft (2-m × 2-m) in the horizontal plane. The longwall shearer extracts a slice of approximately 3 feet (1 m) in horizontal thickness when making a cut along the face. Given the element size chosen in modeling, face advance was simulated in 6-ft (2-m) increments. In numerical modeling, each simulated advance involved removing a full row of elements and running the simulation again until equilibrium was achieved and resulting data saved. This process of modeling face advance in 6-ft (2-m) increments was repeated through a total advance of 1063 feet (324 m) in the FISH (short for "FLAC-ISH" or the language of FLAC) code. Vertical forces within the face area (*i.e.*, simulating longwall shield supports) were also moved with face advance after each cut was completed. The move distance was the same as the extraction thickness (*i.e.*, 6 feet (2m)).

3.3.6 Simulation of Gob Loading Characteristics and Longwall Hydraulic Supports

When material caves behind an advancing longwall, it is initially loose, not compacted. The volume of the caved material is about 25% larger than in the uncaved or intact state. Therefore, after a certain amount of caving, it acts as the medium of load transfer between the floor and the roof (see Figure 3.5). With face advance, the caved material becomes more compacted and stiffer and therefore can assume more load. About 200 feet (60 m) behind the face, the gob transfers pre-mining vertical stress between the roof and the floor. Abbasi *et al*. (2014) developed gob loading characteristics behind the longwall face and implemented them into a FLAC3D simulation model with code to simulate vertical loading at selected nodal points in the roof and floor corresponding to load carrying characteristics of the gob. They compared roof-to-floor convergence data from the simulation model with field observations in set-up rooms and gate development entries. Results compared within 10-15% for several points. A similar numerical model code was written for this research to apply vertical force vectors to simulate this increase in load bearing capacity of the gob as the material gets further behind the advancing face. Modeled load characteristics of the gob are shown in Figure 3.6.

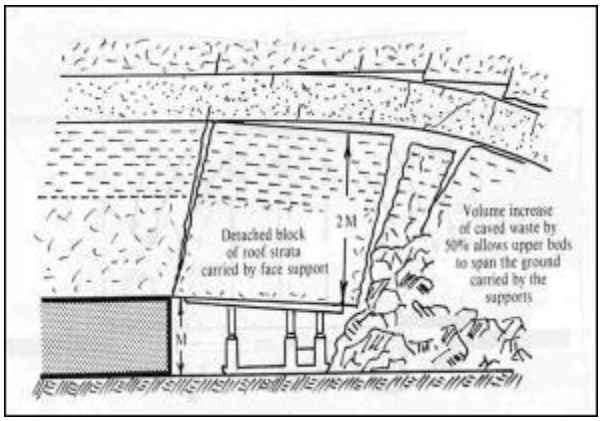

Figure 3.5: Side view of longwall hydraulic support (Whitaker and Reddish, 1989).

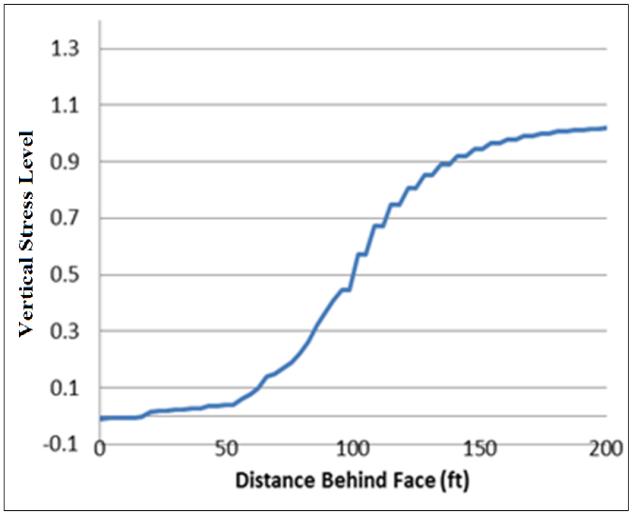

Figure 3.6: Gob loading characteristics simulated in numerical models.

The principal roof support mechanism used in coal mines are roof bolts, which come in many lengths and stiffness, and with many mechanical compositions. Multiple bolt types can be applied in the same mining environment; however, no roof bolts are used on an operating longwall face. Instead, workers in the extraction environment are protected from hundreds of feet of overburden by hydraulic steel supports. These supports use forward facing hydraulic jacks to push the longwall extraction apparatus forward and then pull themselves up to the apparatus, but their main purpose is supporting the overburden strata above the longwall face, which is achieved by massive upward facing hydraulic jacks. At the depths modeled, these jacks are predicted to have less than 200 psi (1.4 MPa) of pressure. This comes from the assumption for overburden density being 5 slugs per cubic foot (2577 kg per cubic meter). Within both models, vertical force vectors were used above and below the location of hydraulic supports to approximate this loading.

3.3.7 Stress Concentration Factors

Stress concentration factors (SCFs) represent stress levels at a given point once mining has begun as compared to stress levels before mining. The SCF at a given location is defined as a calculated ratio of stress at a point divided by the average stress applied initially before mining began. Several SCFs can be calculated by dividing stresses in the *x*, *y*, and *z* directions by the applied vertical stress. This same calculation can be performed to determine shear stress concentration factors (SSCF). In *x* and *y* directions, horizontal SCFs (HSCF) can be calculated by dividing measured post-mining stress by pre-mining vertical stress. The *z* direction represents the most critical SCF for this study. It is called the vertical stress concentration factor (VSCF).

$$Vertical\ stress\ concentration\ factor\ (VSCF) = \frac{\sigma_v}{S_v} \qquad \text{Eq. (3.10)}$$

$$Horizontal\ stress\ concentration\ factor\ (HSCF) = \frac{\sigma_h}{S_v} \qquad \text{Eq. (3.11)}$$

$$Shear\ stress\ concentration\ factor\ (SSCF) = \frac{\tau}{S_v} \qquad \text{Eq. (3.12)}$$

where S_v: Pre-mining applied vertical stress,

σ_v: Vertical stress at a point after excavation,

σ_h: Horizontal stress at a point after excavation, and

τ: Shear stress at a point after excavation.

3.3.8 Model Validation

One of the models in this study incorporated a UJRM fault plane within FLAC3D. It was created using SI units. The simulated set-up room geometry is shown in Figure 3.7. The UJRM representing the fault plane was aligned three-dimensionally with the UJRM set-up room model developed by Abbasi *et al*. (2014). The model in this study also used slightly smaller mesh

sizing than the Abbasi model to improve simulation accuracy. To validate the numerical model developed in this study, results were compared with Abbasi model along two (2) cross-sections as shown in Figures 3.8 and 3.9.

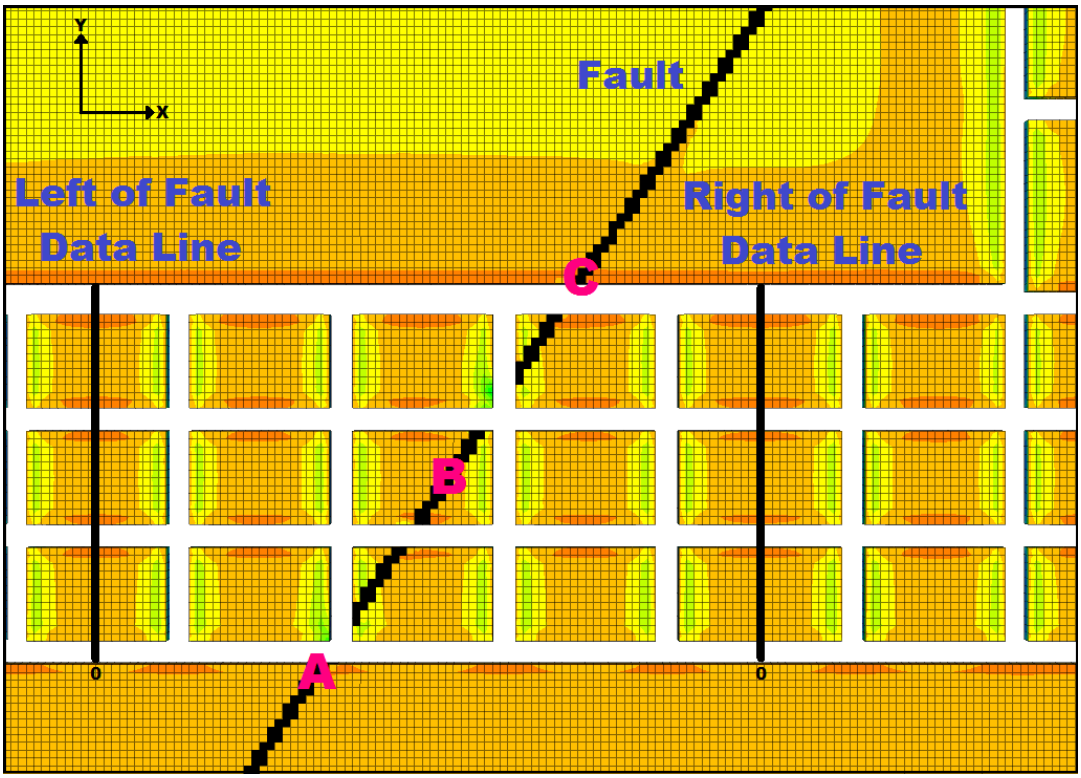

Figure 3.7: Set-up room geometry showing fault location and model validation cross-sections.

The comparison between these two (2) models was made after entries were developed and no advancement of face supports had occurred. Results are similar; however, some divergences exist. These differences are due to different mesh densities and numerical error in modeling. In *x* and *y* directions, the Carlton model used 6-ft (2-m) mesh densities where the Abbasi model used 10 feet (3 m). Displacements occurring at around 309 feet (94 m) of face advance are significantly larger in the base model since it took into consideration a wider set-up room of 26 feet (8 m) as opposed to the Abbasi model, which used a standard 20-ft (6-m) entry

width. The wider set-up room is more realistic and allows for correct spacing of longwall hydraulic supports.

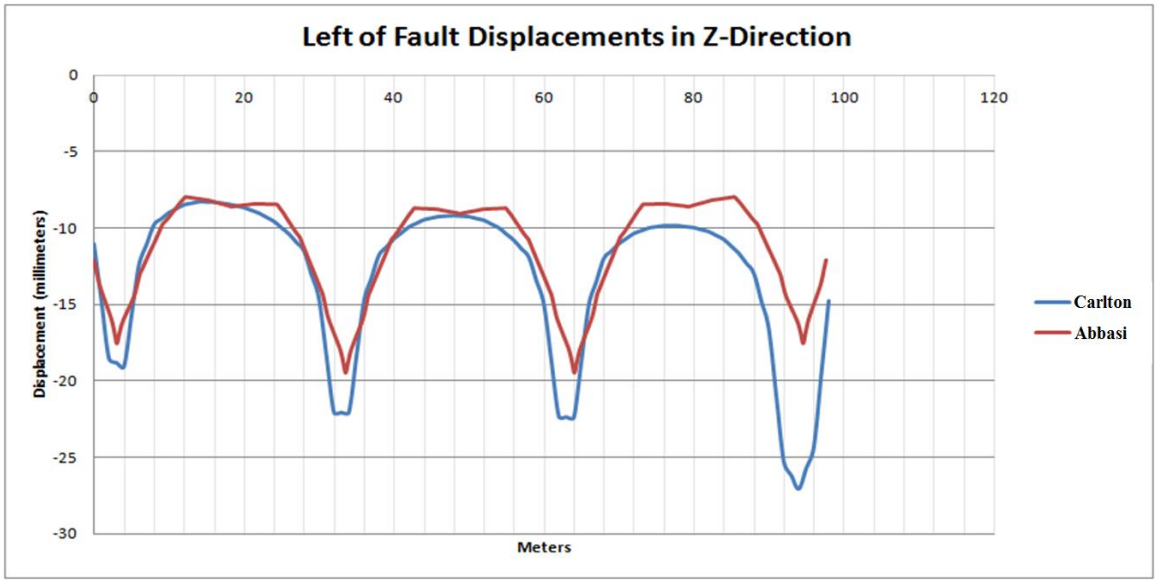

Figure 3.8: Validation comparison left of fault displacement in z-direction.

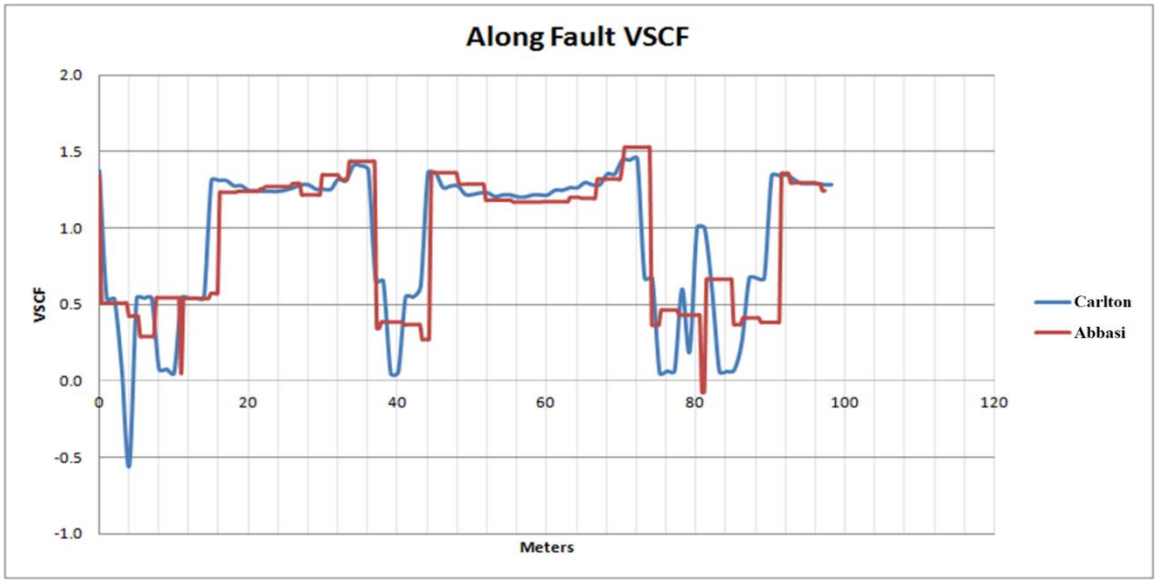

Figure 3.9: Comparison of VSC along the fault line (A-A').

3.3.9 Minimizing Modeling Errors

FLAC numerical models solve large sets of simultaneous equations, and repeat them until residual errors are within acceptable limits defined by the user. Reducing residual error limits increases processing time. Therefore, the author performed a study of acceptable residual error and processing time requirements with the developed models. The slope of the residual curve was achieved as a function of the number of iterations coupled with differences in values of vertical stress concentration factors. This was used to decide the residual error while minimizing the model run time. Residual error of 1 e-4 was selected since changes in stresses beyond this value were typically less than 1% (Figure 3.10).

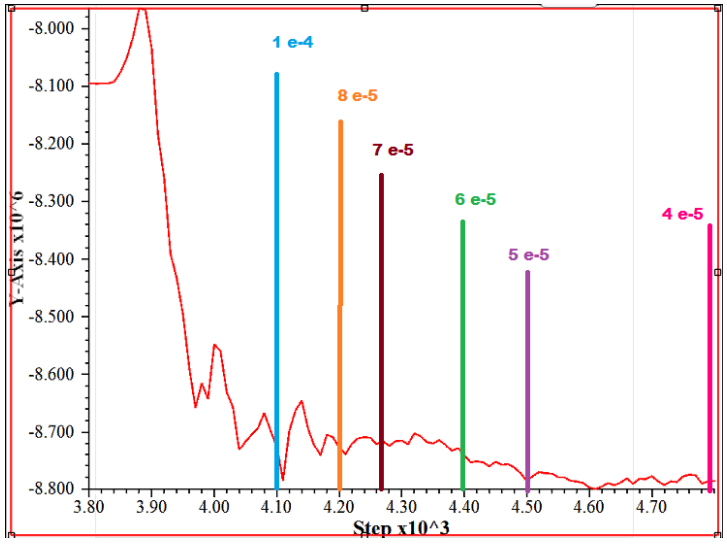

Figure 3.10: Residual error as a function of number of iterations.

3.4 In-Mine Geotechnical Studies

Using manual data collection methods, ground movements were monitored in the cooperating longwall mine located in southeastern Illinois (Figure 3.11). Methods included control points for roof-to-floor convergence (RF) and roof bolt rosettes (RR). Figure 3.12 shows

the formation of wooden cribs used for taking rosette measurements. Figure 3.13 provides an example of RF data. A total of 14 RF points and 6 RR points were set up (Figure 3.14). These points were monitored as the longwall face advanced from initial mining in set-up rooms through a total of 3,550 feet (1,082 m). For accuracy, each measurement was taken three (3) times and the average was used in model calculations.

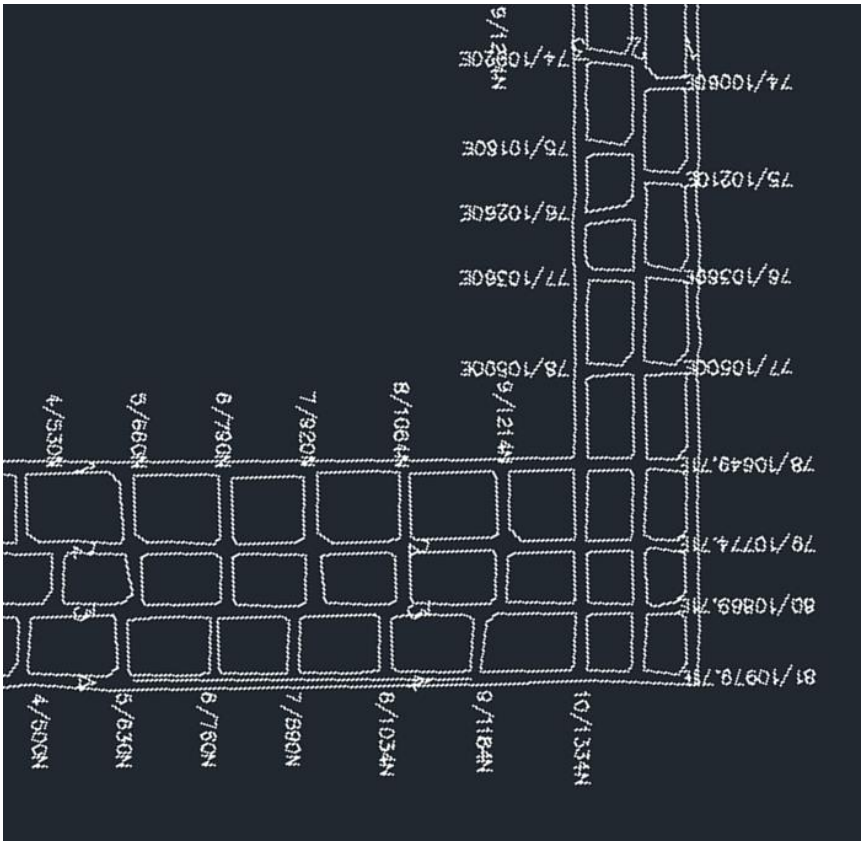

Figure 3.11: Southeastern Illinois mine panel where field observations were made.

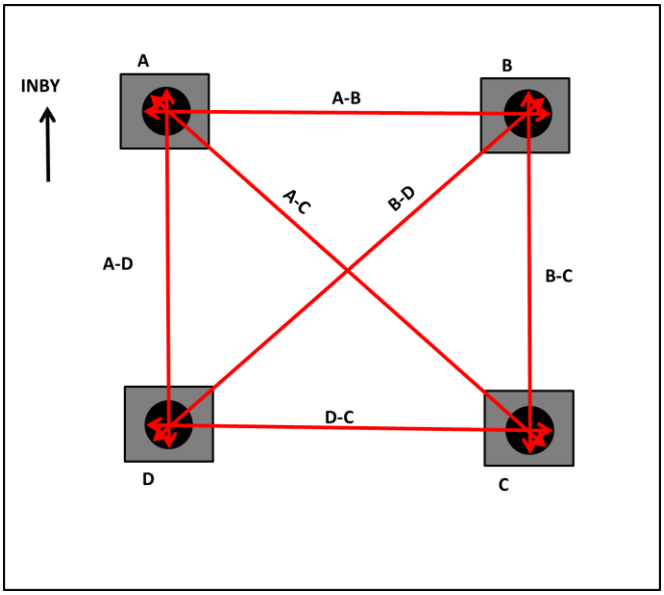

Figure 3.12: Example of crib rosette used for measuring rock mass distortion.

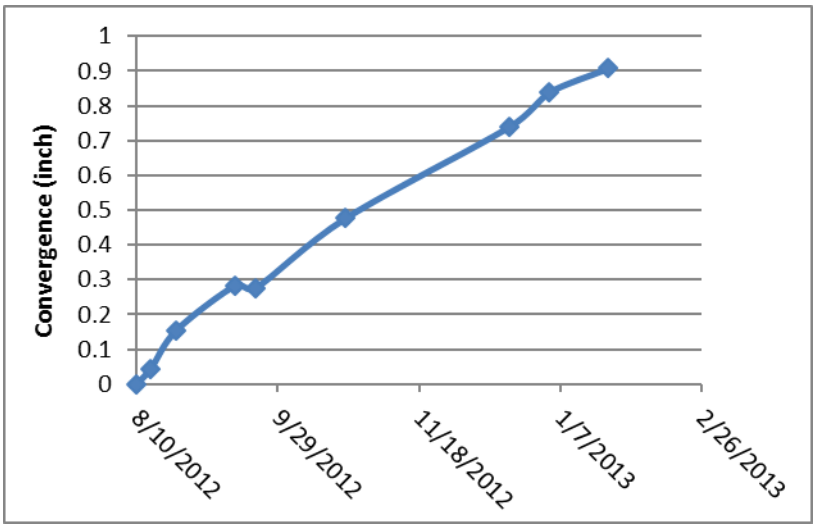

Figure 3.13: Example of roof-to-floor converge results as mining advances.

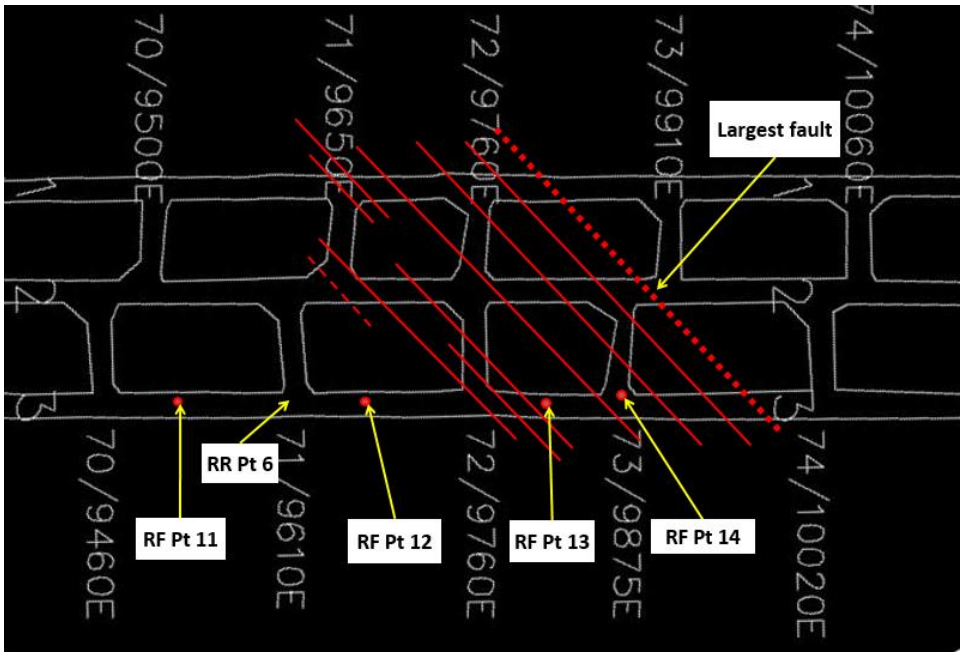

Figure 3.14: Location of faults and measurement points.

3.5 Limitations of Model Development and Analysis

Even though attempts were made to simulate the physical problem as accurately as possible, it is important to identify several important limitations of this effort. These include modeling limitations, such as model size and number of elements; however, the more significant limitations have to do with uncertainty in several model inputs. For example, there is uncertainty in modeling the geometry of the fault plane and adjoining rock mass, whose engineering properties affected faulting. There is uncertainty in estimating rock mass properties (*e.g.*, GSI values). There is uncertainty in defining engineering properties adjoining the fault plane and the variable lithology of immediate roof and floor strata. Despite these limitations, modeling provides significant insights into load transfer mechanisms between the longwall face, development gate entries, and the gob.

3.6 Analysis of Data from Numerical Modeling

For this study, a total of ten (10) data lines were analyzed from A-A' to J-J'. Data from both the roof above the coal seam and the floor below the coal seam was taken from data lines. Data lines B-B', C-C', and D-D' run along set-up room entries 1 foot (0.3 m) into coal pillars. Data line E-E' runs along the panel 1 foot (0.3 m) into the block of coal. Data lines F-F', G-G', H-H', and I-I' run along tailgate entries 1 foot (0.3 m) into coal pillars. Their locations were chosen because stresses redistribute based on geometry and concentrations of stresses occur at pillar edges. Data line A-A' runs along the fault. This is a data line for obtaining information critical to the project's purpose centering about the fault. All of the previously mentioned data lines are static throughout all analysis. J-J' is the only data line whose location changes depending on the location of the advancing face. This data line was always located 1foot (0.3 m) into the solid coal block in front of the advancing longwall face. The primary motive for using this data line was the redistribution of stresses due to caving behind the face. These data lines can be observed in the plan view of the coal seam level of the model in Figure 3.15.

3.6.1 Displacement Variables

In this study, displacements in both horizontal *x* and *y* directions and the vertical *z* direction were determined. Roof-to-floor convergence of the coal seam was calculated from vertical displacements of two (2) points; one (1) point in the roof and one (1) point in the floor with matching *x* and *y* coordinates. Incremental displacements were calculated by subtracting a point's displacement at a given face location from the displacement when the face was located at the previous location. Total displacement of a point was calculated by taking the square root of the sum of the squares for *x*-, *y*-, and *z*-direction displacements.

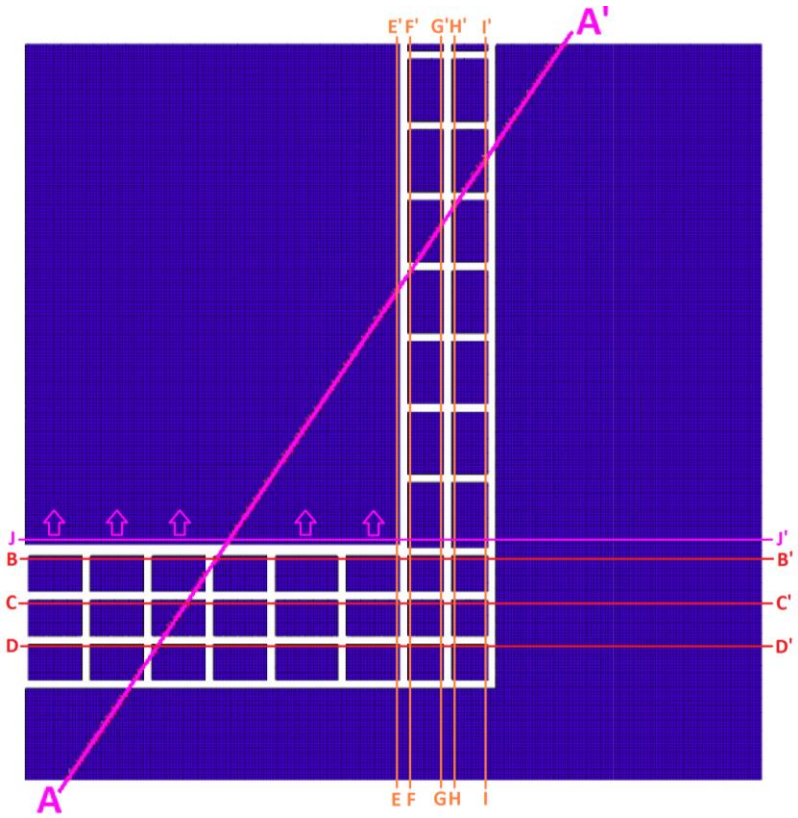

Figure 3.15: Modeled area with primary data lines used for analysis.

CHAPTER 4

ANALYTICAL STUDIES

4.1 Model Analysis

Two models were analyzed with the difference being that Model 1 did not include the fault zone and Model 2 did include the fault zone. Figure 4.1 shows principal data lines used in the analysis, as well as distances of longwall face advance within the model. This chapter presents results describing the effects of the fault on ground control in set-up rooms, the longwall face area, and longwall development areas on the headgate side.

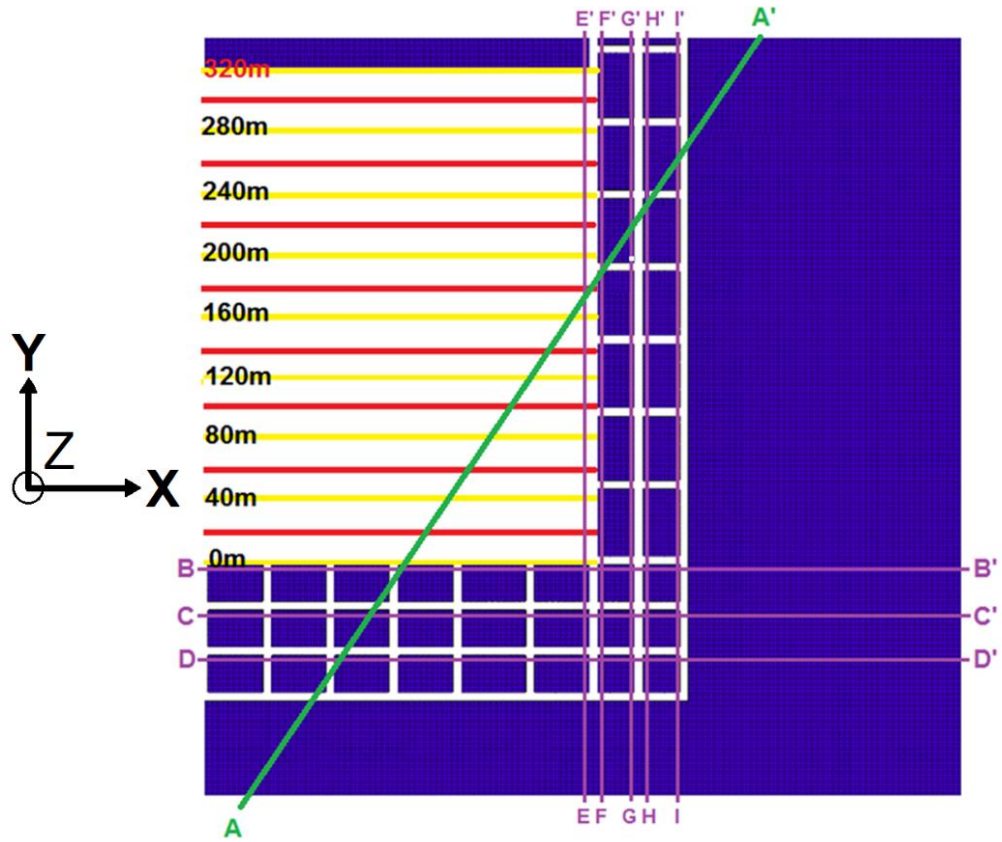

Figure 4.1: Model depiction with principal data lines (purple), fault zone (green), and face advance distances (red and yellow).

4.2 Analysis of Set-up Room Entries Intersected by the Fault

4.2.1 Model Comparisons at 100 feet (30 m) of Face Advance

Four (4) data lines were examined in the set-up room area: A-A' (fault), B-B' (first row of set-up room pillars), C-C' (second row of set-up room pillars), and J-J' (longwall face advanced 100 feet (30 m)). The amount of change (in percentage) between the two (2) models is shown where each data line intersects the fault (A-A' data line). In the case of the moving data line J-J', the intersection with A-A' moves with advance. The location of the fault is marked by a vertical purple line within each figure. The state of both models after 100 feet (30 m) of advance is shown in Figure 4.2. Other figures and summary tables show comparison data in the set-up room area for up to 200 feet (60 m) of advance.

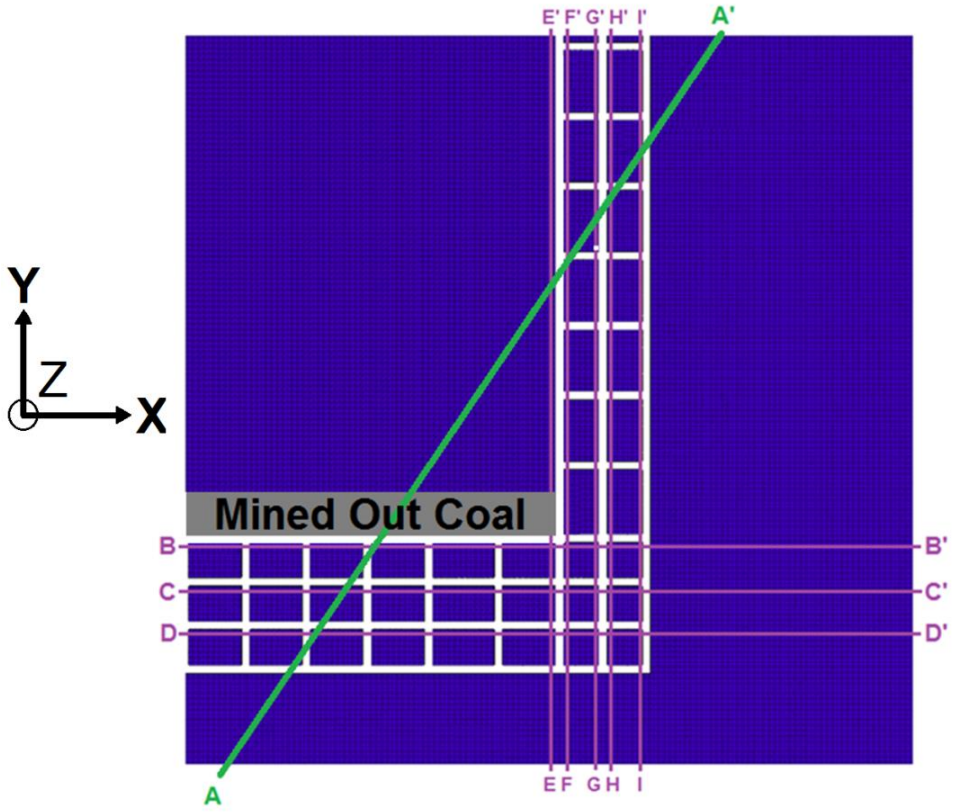

Figure 4.2: Data lines (purple) and fault (green) at 100 feet (30 m) of face advance (gray).

- B-B’ data line
    - Average VSCF-ZZ around the fault decreases 7% from 2.52 from 2.34. See Figure 4.3. Changes in HSCF-XX (2.4 average) and HSCF-YY (1.73 average) were minimal due to the presence of the fault.
    - X-displacements were small and increased 36% from -0.010 inches (-0.026 cm) to -0.014 inches (-0.035 cm) when the fault is present. See Figure 4.4.
    - Changes in Y-displacement and Z-displacement were minimal due to the presence of the fault. Displacements averaged 0.8 inches (2 cm) in the Y direction (see Figure 4.5) and 2.0 inches (5 cm) in the Z direction.

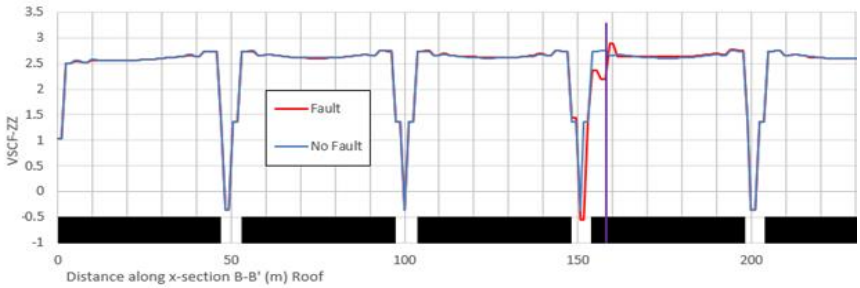

Figure 4.3: VSCF-ZZ in Models 1 and 2 along B-B’ after 100 feet (30 m) of face advance.

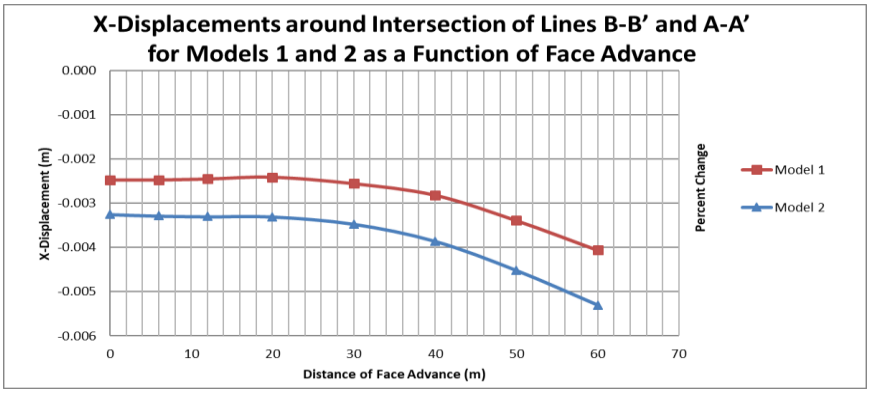

Figure 4.4: X-displacements in Models 1 and 2 at B-B’/A-A’ intersection for advancing face.

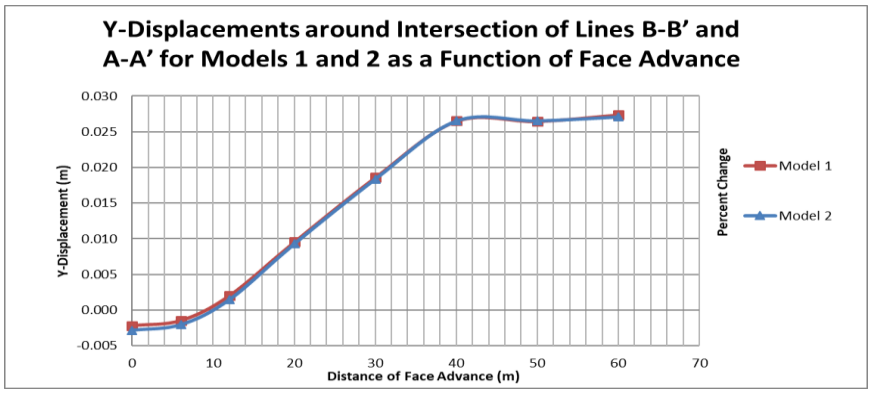

Figure 4.5: Y-displacements in Models 1 and 2 at B-B'/A-A' intersection for advancing face.

- C-C' data line
    - Changes in Z-displacement, HSCF-XX, HSCF-YY, and VSCF-ZZ were minimal due to the fault. Average values were: Z-displacement – 0.4 inches (1 cm), HSCF-XX – 2.1, HSCF-YY – 1.24, and VSCF-ZZ – 1.28.
    - X-displacements were small and only slightly changed due to the presence of the fault. See Figure 4.6.
    - Y-displacements increased 84% from 0.05 inches (0.13 cm) to 0.09 inches (0.24 cm) due to fault. See Figures 4.7 and 4.8.

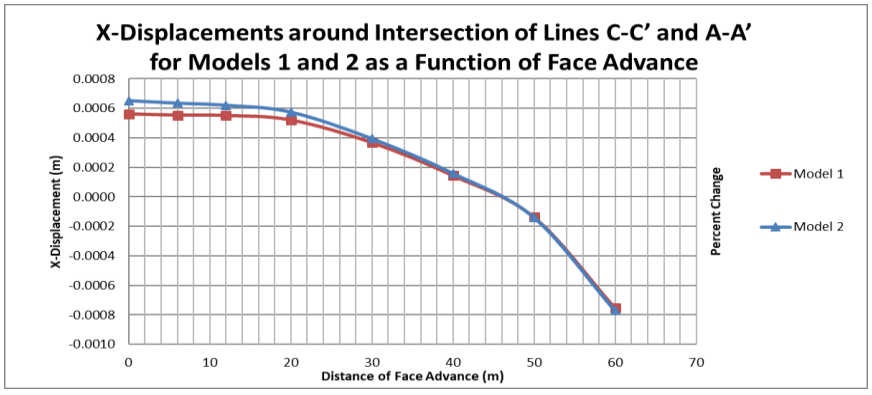

Figure 4.6: X-displacements in Models 1 and 2 at C-C'/A-A' intersection for advancing face.

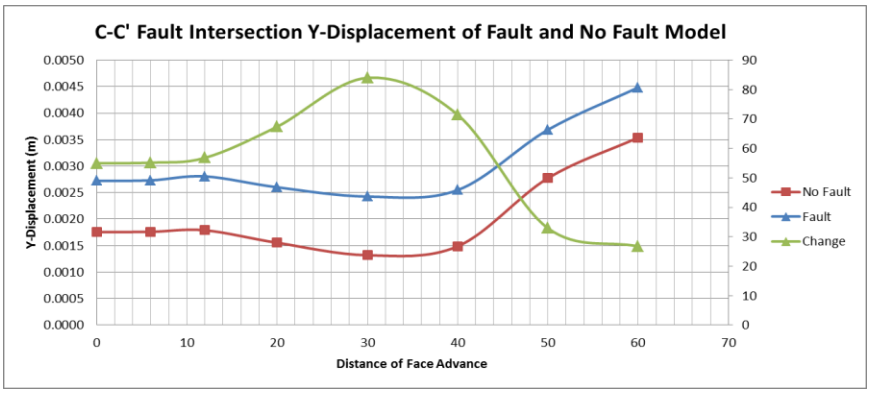

Figure 4.7: Y-displacements in Models 1 and 2 at C-C'/A-A' intersection for advancing face.

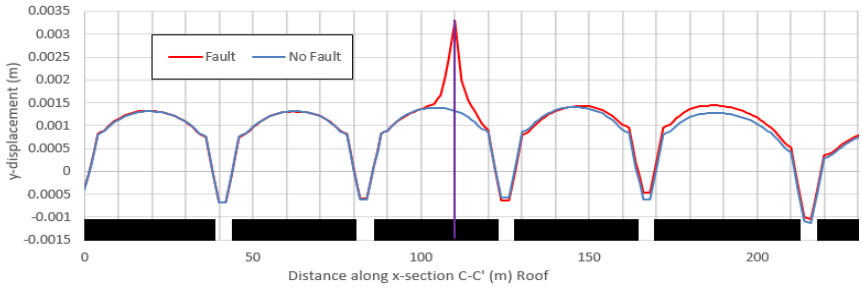

Figure 4.8: Y-displacements in Models 1 and 2 at C-C'/A-A' intersection after 100 feet (30 m) of face advance.

- A-A' data line
    - Changes in Y-displacement, Z-displacement, and HSCF-XX due to fault presence were minimal. Average values were 0.8 inches (2 cm), 2.4 inches (6 cm), and 2.07, respectively. X-displacements are small and decreased due to the fault. See Figures 4.9 and 4.10.
    - HSCF-YY decreased 15% from 1.50 down to 1.27.
    - VSCF-ZZ decreased 23% from 0.96 to 0.73. Beyond the immediate 10-foot (3 m) radius examined at the intersection of the fault and face, VSCF-ZZ increases up to 2.0 and then to 2.5. This is due to less confinement in the face area and lower

stiffness along the fault. The confined coal solid ahead of the face is picking up additional load not observed within the radius of examination. See Figure 4.11.

- Averaged VSCF-ZZ values were less than 1.25 for Model 2 and less than 1.13 for Model 1 for face advances of 0 to 200 feet (60 m). At 66 feet (20 m) of face advance, Model 2 experienced 15% higher VSCF-ZZ averages; and at 132 feet (40 m) of face advance, Model 2 experienced 23% higher VSCF-ZZ averages. Model 1 VSCF-ZZ averages were 23% lower at 98 feet (30 m) and 13% lower at 164 feet (50 m) and 197 feet (60 m).

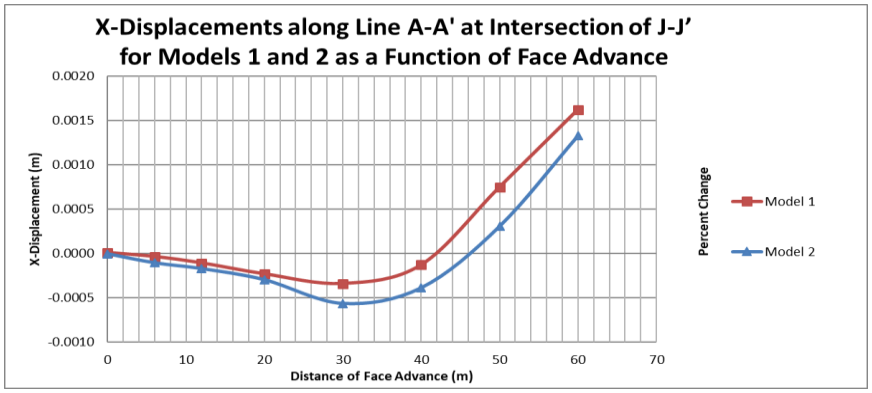

Figure 4.9: X-displacements in Models 1 and 2 at A-A'/J-J' intersection for advancing face.

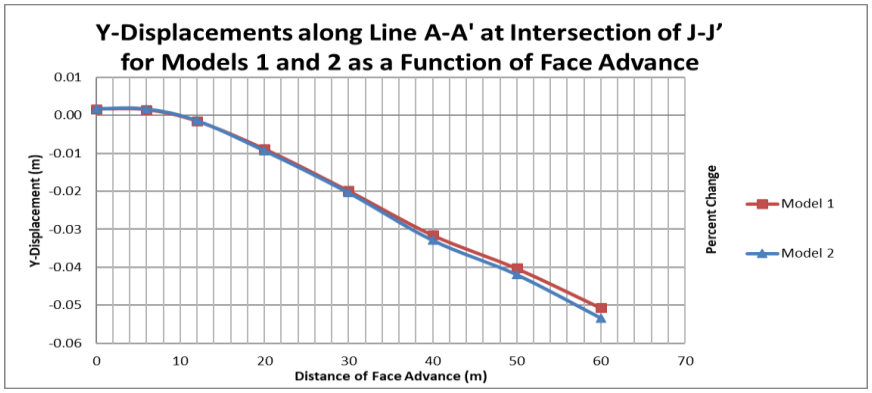

Figure 4.10: Y-displacements in Models 1 and 2 at A-A'/J-J' intersection for advancing face.

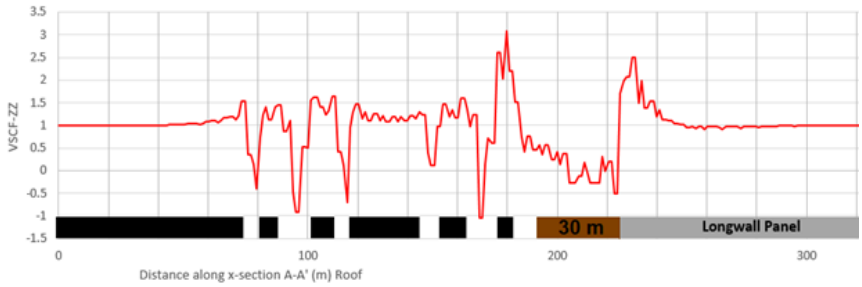

Figure 4.11: VSCF-ZZ in Model 2 along A-A' after 100 feet (30 m) of face advance.

- J-J' data line
    - Changes in Y-displacement, Z-displacement, and HSCF-XX were minimal due to fault presence. Average values were 0.75 inches (1.9 cm), -2.00 inches (-5 cm), and 2.52, respectively. X-displacements are small and decrease due to the fault from 0.059 inches (0.15 cm) for Model 1 to 0.0315 inches (0.08 cm) for Model 2. See Figures 4.12 through 4.14.
    - HSCF-YY decreased about 7% from 1.94 down to 1.8.
    - VSCF-ZZ decreased about 15% from 2.75 down to 2.47.

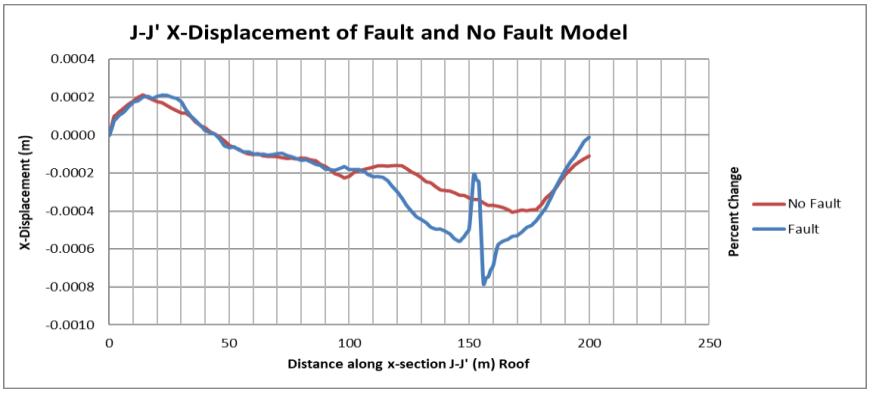

Figure 4.12: X-displacements in Models 1 and 2 along J-J' after 100 feet (30 m) of face advance.

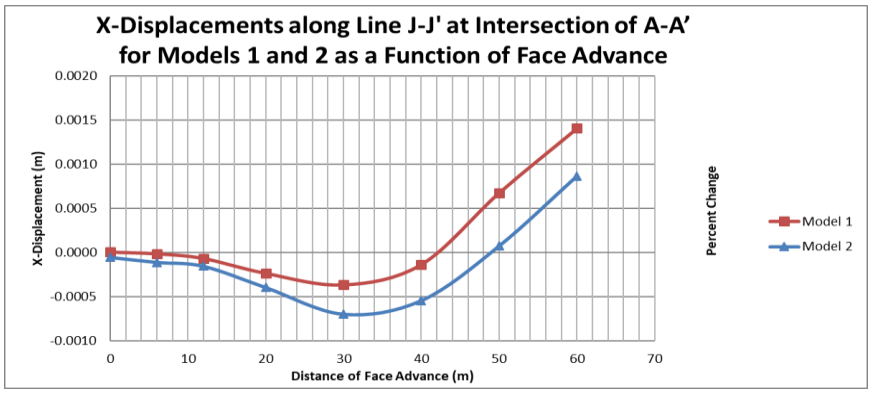

Figure 4.13: X-displacements in Models 1 and 2 at J-J'/A-A' intersection for advancing face.

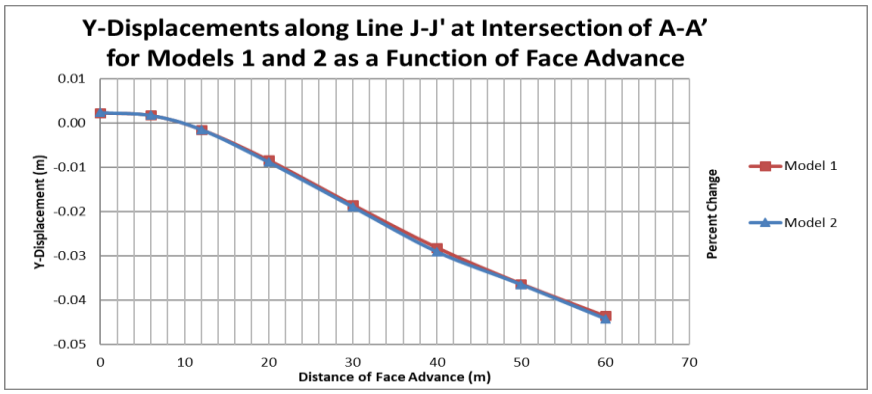

Figure 4.14: Y-displacements in Models 1 and 2 at J-J'/A-A' intersection for advancing face.

4.2.2 Results Summary of Set-up Room Analysis

- Data pertaining to areas where B-B', C-C', and J-J' intersect the fault and where A-A' intersects the moving face through 200 feet (60 m) of face advance are presented in Tables 4.1 through 4.4. Each table shows data from Model 1 in the top section, data from Model 2 in the middle section, and the percentage change from the base case (Model 1 with no fault) in the bottom section.

Table 4.1: Average results for B-B' data line within ±9.83 feet (3 m) of intersection with fault for 0 to 200 feet (60 m) of face advance.

Avg (± 3m) Model 1	B-B' x-disp (m)	B-B' y-disp (m)	B-B' z-disp (m)	B-B' HSCF-XX	B-B' HSCF-YY	B-B' VSCF-ZZ
0 m	-0.0025	-0.0022	-0.0105	2.02	1.06	1.24
6 m	-0.0025	-0.0015	-0.0137	2.07	1.08	1.43
12 m	-0.0025	0.0020	-0.0241	2.15	1.14	1.80
20 m	-0.0024	0.0095	-0.0399	2.29	1.37	2.32
30 m	-0.0026	0.0186	-0.0516	2.40	1.73	2.52
40 m	-0.0028	0.0265	-0.0576	2.55	2.18	2.82
50 m	-0.0034	0.0265	-0.0445	2.50	2.43	2.23
60 m	-0.0041	0.0274	-0.0425	2.52	2.56	2.16

Avg (± 3m) Model 2	B-B' x-disp (m)	B-B' y-disp (m)	B-B' z-disp (m)	B-B' HSCF-XX	B-B' HSCF-YY	B-B' VSCF-ZZ
0 m	-0.0033	-0.0028	-0.0107	1.99	1.08	1.21
6 m	-0.0033	-0.0020	-0.0141	2.05	1.13	1.38
12 m	-0.0033	0.0015	-0.0246	2.17	1.23	1.71
20 m	-0.0033	0.0093	-0.0409	2.35	1.46	2.17
30 m	-0.0035	0.0184	-0.0528	2.45	1.67	2.34
40 m	-0.0039	0.0265	-0.0590	2.60	1.96	2.61
50 m	-0.0045	0.0265	-0.0465	2.47	1.97	2.11
60 m	-0.0053	0.0270	-0.0439	2.47	2.02	2.03

Avg (± 3m) Change	B-B' x-disp (%)	B-B' y-disp (%)	B-B' z-disp (%)	B-B' HSCF-XX (%)	B-B' HSCF-YY (%)	B-B' VSCF-ZZ (%)
0 m	31	29	2	-1	2	-2
6 m	33	39	3	-1	4	-3
12 m	35	-26	2	1	8	-5
20 m	37	-3	2	2	6	-6
30 m	36	-1	2	2	-4	-7
40 m	37	0	2	2	-10	-7
50 m	33	0	5	-1	-19	-6
60 m	31	-1	3	-2	-21	-6

Table 4.2: Average results for C-C' data line within ±9.83 feet (3 m) of intersection with fault for 0 to 200 feet (60 m) of face advance.

Avg (± 3m) Model 1	C-C' x-disp (m)	C-C' y-disp (m)	C-C' z-disp (m)	C-C' HSCF-XX	C-C' HSCF-YY	C-C' VSCF-ZZ
0 m	0.0006	0.0018	-0.0105	2.01	1.11	1.36
6 m	0.0006	0.0018	-0.0109	2.02	1.12	1.37
12 m	0.0005	0.0018	-0.0108	2.02	1.17	1.37
20 m	0.0005	0.0016	-0.0100	2.04	1.25	1.35
30 m	0.0004	0.0013	-0.0087	2.04	1.31	1.31
40 m	0.0001	0.0015	-0.0076	2.04	1.33	1.28
50 m	-0.0001	0.0028	-0.0072	2.03	1.27	1.27
60 m	-0.0008	0.0035	-0.0069	2.03	1.27	1.26

Avg (± 3m) Model 2	C-C' x-disp (m)	C-C' y-disp (m)	C-C' z-disp (m)	C-C' HSCF-XX	C-C' HSCF-YY	C-C' VSCF-ZZ
0 m	0.0007	0.0027	-0.0106	2.09	1.17	1.36
6 m	0.0006	0.0027	-0.0110	2.09	1.17	1.37
12 m	0.0006	0.0028	-0.0109	2.09	1.20	1.36
20 m	0.0006	0.0026	-0.0101	2.10	1.23	1.34
30 m	0.0004	0.0024	-0.0088	2.10	1.24	1.28
40 m	0.0002	0.0025	-0.0077	2.09	1.24	1.26
50 m	-0.0001	0.0037	-0.0073	2.08	1.21	1.25
60 m	-0.0008	0.0045	-0.0070	2.08	1.20	1.24

Avg (± 3m) Change	C-C' x-disp (%)	C-C' y-disp (%)	C-C' z-disp (%)	C-C' HSCF-XX (%)	C-C' HSCF-YY (%)	C-C' VSCF-ZZ (%)
0 m	16	55	1	4	5	0
6 m	15	55	1	4	5	-1
12 m	13	57	1	3	3	-1
20 m	10	67	1	3	-1	0
30 m	8	84	1	3	-5	-2
40 m	11	71	1	3	-7	-2
50 m	2	33	1	3	-5	-2
60 m	3	27	1	3	-5	-2

Table 4.3: Average results for A-A' data line within ±9.83 feet (3 m) of intersection with face for 0 to 200 feet (60 m) of face advance.

Avg (± 3m) Model 1	A-A' x-disp (m)	A-A' y-disp (m)	A-A' z-disp (m)	A-A' HSCF-XX	A-A' HSCF-YY	A-A' VSCF-ZZ
0 m	0.0000	0.0017	-0.0065	1.98	1.19	0.82
6 m	0.0000	0.0015	-0.0061	2.04	1.24	1.02
12 m	-0.0001	-0.0015	-0.0137	2.09	1.36	1.13
20 m	-0.0002	-0.0088	-0.0343	2.07	1.34	1.09
30 m	-0.0003	-0.0198	-0.0581	2.07	1.49	0.96
40 m	-0.0001	-0.0315	-0.0850	2.03	1.55	0.65
50 m	0.0007	-0.0403	-0.1036	2.09	1.76	0.70
60 m	0.0016	-0.0507	-0.1342	2.01	1.53	0.44

Avg (± 3m) Model 2	A-A' x-disp (m)	A-A' y-disp (m)	A-A' z-disp (m)	A-A' HSCF-XX	A-A' HSCF-YY	A-A' VSCF-ZZ
0 m	0.0000	0.0018	-0.0067	1.95	1.19	0.80
6 m	-0.0001	0.0017	-0.0064	2.02	1.16	0.98
12 m	-0.0002	-0.0014	-0.0141	2.08	1.31	1.16
20 m	-0.0003	-0.0093	-0.0355	2.04	1.38	1.25
30 m	-0.0006	-0.0204	-0.0600	2.01	1.27	0.73
40 m	-0.0004	-0.0329	-0.0882	1.87	1.43	0.80
50 m	0.0003	-0.0420	-0.1062	1.89	1.17	0.60
60 m	0.0013	-0.0534	-0.1387	1.75	1.09	0.26

Avg (± 3m) Change	A-A' x-disp (%)	A-A' y-disp (%)	A-A' z-disp (%)	A-A' HSCF-XX (%)	A-A' HSCF-YY (%)	A-A' VSCF-ZZ (%)
0 m	-214	6	3	-1	-1	-3
6 m	178	12	5	-1	-6	-4
12 m	57	-8	3	0	-4	2
20 m	28	6	4	-2	3	15
30 m	65	3	3	-3	-15	-23
40 m	195	4	4	-8	-8	23
50 m	-60	4	3	-10	-34	-13
60 m	-18	5	3	-13	-29	-40

Table 4.4: Average results for J-J' data line within ±9.83 feet (3 m) of intersection with fault for 0 to 200 feet (60 m) of face advance.

Avg (± 3m)	J-J'	J-J'	J-J'	J-J'	J-J'	J-J'
Model 1	x-disp (m)	y-disp (m)	z-disp (m)	HSCF-XX	HSCF-YY	VSCF-ZZ
0 m	0.0000	0.0023	-0.0051	2.11	1.20	1.42
6 m	0.0000	0.0017	-0.0065	2.15	1.24	1.57
12 m	-0.0001	-0.0015	-0.0156	2.24	1.35	1.94
20 m	-0.0002	-0.0084	-0.0344	2.33	1.49	2.24
30 m	-0.0004	-0.0185	-0.0498	2.52	1.94	2.75
40 m	-0.0001	-0.0281	-0.0626	2.70	2.39	3.18
50 m	0.0007	-0.0363	-0.0767	2.87	2.76	3.64
60 m	0.0014	-0.0436	-0.0859	3.03	3.19	3.95

Avg (± 3m)	J-J'	J-J'	J-J'	J-J'	J-J'	J-J'
Model 2	x-disp (m)	y-disp (m)	z-disp (m)	HSCF-XX	HSCF-YY	VSCF-ZZ
0 m	-0.0001	0.0024	-0.0052	2.11	1.21	1.37
6 m	-0.0001	0.0017	-0.0067	2.16	1.24	1.58
12 m	-0.0002	-0.0015	-0.0164	2.26	1.35	1.91
20 m	-0.0004	-0.0088	-0.0356	2.37	1.51	2.18
30 m	-0.0007	-0.0189	-0.0514	2.57	1.80	2.47
40 m	-0.0005	-0.0291	-0.0647	2.79	2.15	2.99
50 m	0.0001	-0.0365	-0.0777	2.98	2.40	3.47
60 m	0.0009	-0.0442	-0.0878	3.05	2.51	3.34

Avg (± 3m)	J-J'	J-J'	J-J'	J-J'	J-J'	J-J'
Change	x-disp (%)	y-disp (%)	z-disp (%)	HSCF-XX (%)	HSCF-YY (%)	VSCF-ZZ (%)
0 m	-1675	2	2	0	1	-3
6 m	642	0	3	0	1	0
12 m	132	0	5	1	0	-1
20 m	68	5	4	2	1	-3
30 m	90	3	3	2	-7	-10
40 m	297	3	3	3	-10	-6
50 m	-89	0	1	4	-13	-5
60 m	-39	1	2	1	-21	-15

- X-displacements were relatively small in the set-up room area for all data lines in both models. Generally, Model 2 X-displacements around the fault experienced a decrease compared to Model 1 with a few exceptions.
- Support mechanisms used around first row set-up room pillar should focus on mitigating the rise in X-displacements in the negative x-direction where an additional 0.04 inches (0.1 cm.) of movement occurs.
- In the set-up room along B-B', supports should be placed to mitigate Y-displacements around the fault for the first 39 feet (12 m) of face advance.
- Along C-C', supports should be designed to mitigate post-development Y-displacements around the fault.
- X-displacements are greater in the negative X-direction by approximately 35% in Model 2 from 20 feet (6 m) to 200 feet (60 m) of face advance.
- At the intersection of the fault with B-B' and C-C', VSCF-ZZ decreased similarly when the face advanced and the gob took on more loading.
- At intersection of C-C' with A-A', Y-displacements were significantly larger in Model 2 and in the positive Y-direction towards the mined-out coal. Incremental increases grew larger from 0 to 100 feet (30 m) of face advance, then decreased from 100 feet (30 m) to 200 feet (60 m) of face advance.
- Z-displacements were similar in both models.
- Changes in horizontal stress concentrations (HSCF-XX and HSCF-YY) either decreased or stayed the same from Model 1 to Model 2 when examined within a 10-foot (3-m) radius. This can be seen for all data lines in the set-up room area. Fault rock mass

material has a lower stiffness than surrounding rock mass and shifts loading around the geologic anomaly.

- In this specific fault angle and intersection case, horizontal displacements around the fault are more critical and can show signs of increasing compared to Model 1 whereas SCF values either stay similar between models or decrease in Model 2.
- The A-A'/J-J' intersection as well as B-B' and C-C' experienced less HSCF-YY in Model 2 relative to Model 1 with more face advance. For J-J', after 200 feet (60 m) of face advance, VSCF-ZZ decreased from Model 1 to Model 2 by 0.6 at the face/fault intersection.
- SCF increases are very small and in general decrease due to the presence of the fault. Therefore, enhanced yielding of the rock mass due to changes in SCF values are highly unlikely.
- On a percentage basis, incremental displacements due to fault can be very large. Thus, ground control must involve displacement control support measures. Applying high stiffness control measures can result in the need for high capacity supports. Appropriate control measures should consist of medium stiffness support systems that will have increasing resistance and will continue to provide resistance beyond yield. Thus, a strain hardening model for supports up to the maximum desired value of displacements should be considered.
- Supports should be installed well ahead of when the following maximum displacements are likely to occur:
    - For the fault/face (A-A'/J-J') intersection, maximum X-displacement due to the fault occurs at 98 feet (30 m) of face advance.

- For the fault/face (A-A'/J-J') intersection, maximum Y-displacement due to the fault occurs at 200 feet (60 m) of face advance.
- For the fault (A-A')/B-B' intersection, maximum X-displacement due to the fault occurs at 200 feet (60 m) of face advance.
- For the fault (A-A')/B-B' intersection, maximum Y-displacement due to the fault occurs between 131 feet (40 m) and 200 feet (60 m) of face advance.
- For the fault (A-A')/C-C' intersection, maximum X-displacement due to the fault occurs at 200 feet (60 m) of face advance.
- For the fault (A-A')/C-C' intersection, maximum Y-displacement due to the fault occurs between 164 feet (50 m) and 200 feet (60 m) of face advance.

4.3 Analysis of Gate Entries Intersected by the Fault

4.3.1 Model Comparisons at 558 feet (170 m) of Face Advance

This face advance distance is considered critical for examination as it is where the fault, the face, and development gate entries intersect. Most development gate entry mechanized mining units consist of three (3) entries. They are commonly known as the belt entry next to the block of coal being mined by the longwall, the intake entry in the center, and the return entry on the outside. At the fault's intersection with the three (3) development gate entries, seven (7) data lines were examined. Shown in Figures 4.1 and 4.2, they are: E-E' on the inner (next to the longwall block) side of the belt entry, F-F' on the outer side of the belt entry, G-G' on the inner side of the intake entry, H-H' on the outer side of the intake entry, I-I' on the inner side of the return entry, and the fault and face data lines, A-A' and J-J', respectively. Changes between the

two (2) models are described for the location where each data line intersects the fault in Model 1. Comparisons are given first in the form of figures, then in data tables.

- A-A' data line
    - Displacements changed significantly at the fault/face/gate entry intersection. X-displacement decreased from a peak of -3.1 inches (-8.0 cm) to -2.4 inches (-6.2 cm), Y-displacement are in the negative direction towards the void and decreased in the fault model due to the fault's dip having a positive y-direction orientation, and Z-displacement did not show significant changes while the portion of the panel being mined included the fault. See Figures 4.15, 4.16, and 4.17.
    - Stresses decreased at the fault/face/gate entry intersection. HSCF-XX decreased 49% to 1.28, HSCF-YY decreased 90% to 0.33, and VSCF-ZZ decreased 104% to -0.09. See Figure 4.18

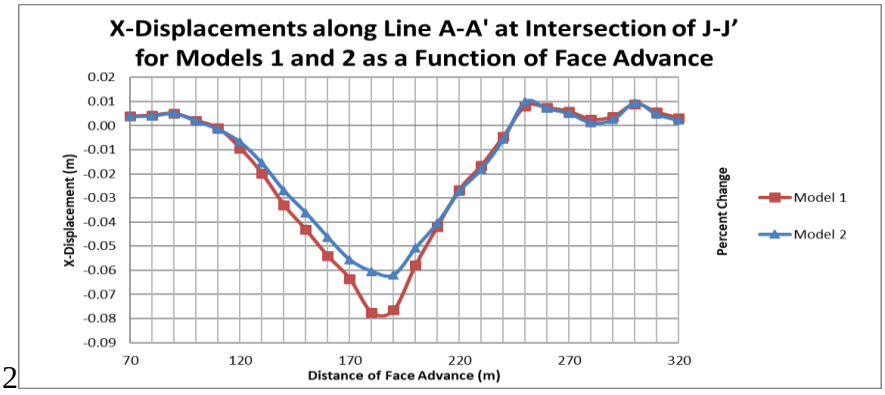

2

Figure 4.15: X-displacements in Models 1 and 2 at the fault/face intersection for face advancing from 230 feet (70 m) through 1050 feet (320 m).

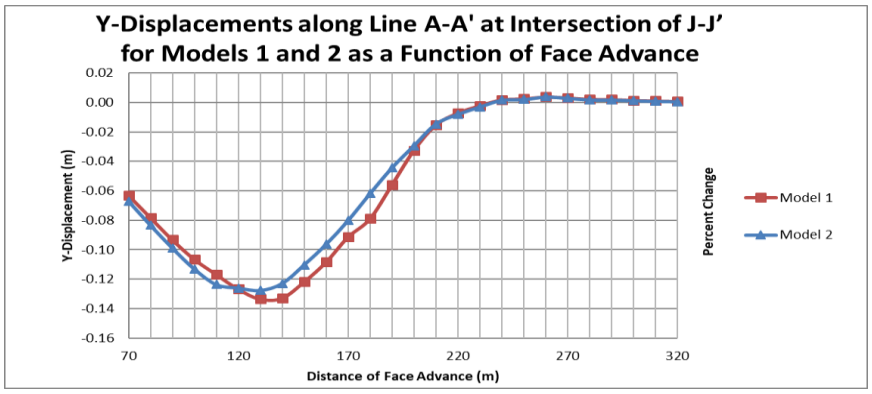

Figure 4.16: Y-displacements in Models 1 and 2 at the fault/face intersection for face advancing from 230 feet (70 m) through 1050 feet (320 m).

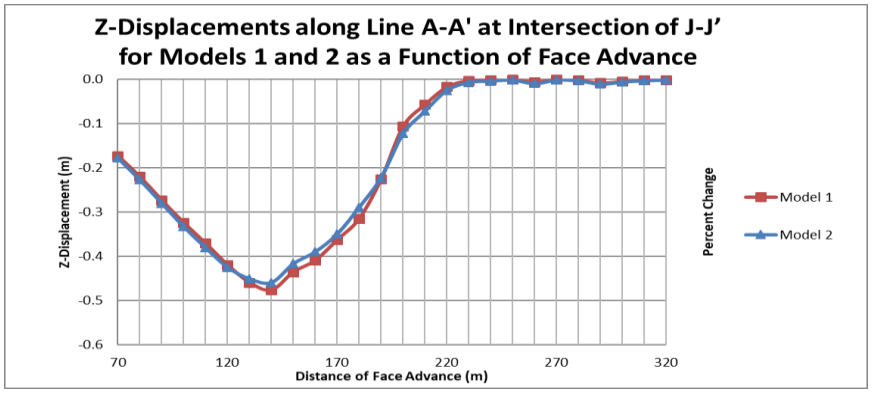

Figure 4.17: Z-displacements in Models 1 and 2 at the fault/face intersection for face advancing from 230 feet (70 m) through 1050 feet (320 m).

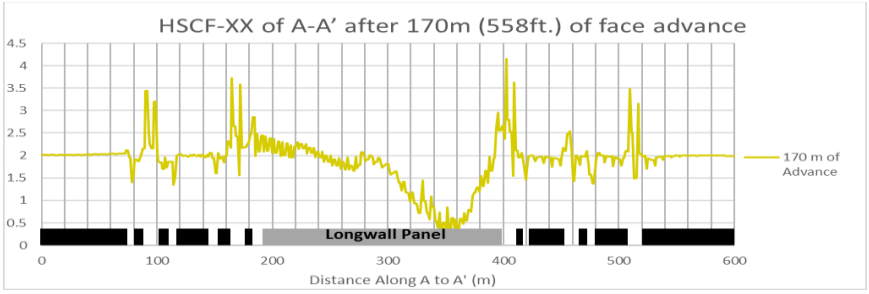

Figure 4.18: HSCF-XX for A-A’ after 558 feet (170 m) of face advance.

- J-J’ data line
    - Y-displacements, Z-displacements, and HSCF-XX did not show significant change between the two (2) models. See Figures 4.19, 4.20, and 4.21.
    - X-displacements decreased 20% to 0.8 inches (2 cm) as the face advanced past the gate-entry/fault intersection. A peak value of 1 inch (2.5 cm) occurred when the face had advanced 230 feet (70 m) past where the fault intersected the gate entries. Horizontal displacements around face/fault/gate entry intersection locations were slightly less in Model 2 than in Model 1. Therefore, the inclusion of the weak plane resulted in less horizontal movement around this location. A slight increase in z-directions occurred.
    - Stresses decreased at the intersection. HSCF-YY decreased 10% to 4.12 and VSCF-ZZ decreased 11% to 4.11.

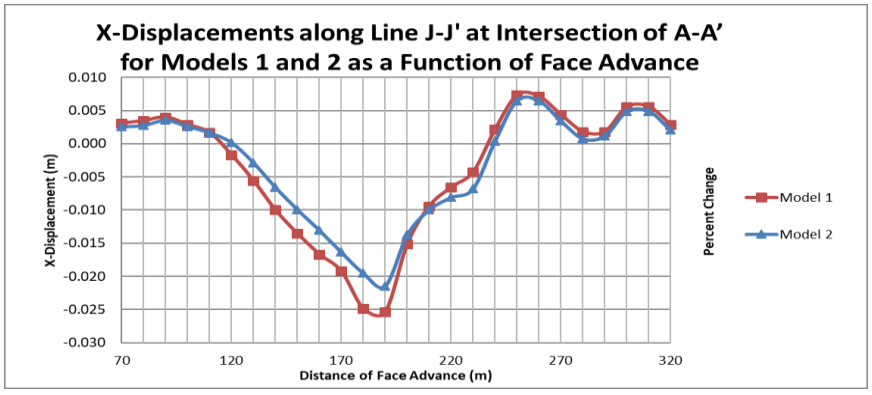

Figure 4.19: X-displacements in Models 1 and 2 at the face/fault intersection for face advancing from 230 feet (70 m) through 1050 feet (320 m).

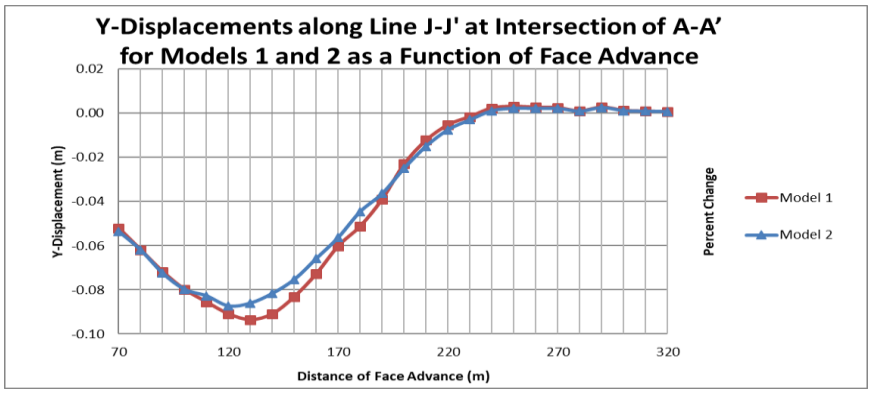

Figure 4.20: Y-displacements in Models 1 and 2 at the face/fault intersection for face advancing from 230 feet (70 m) through 1050 feet (320 m).

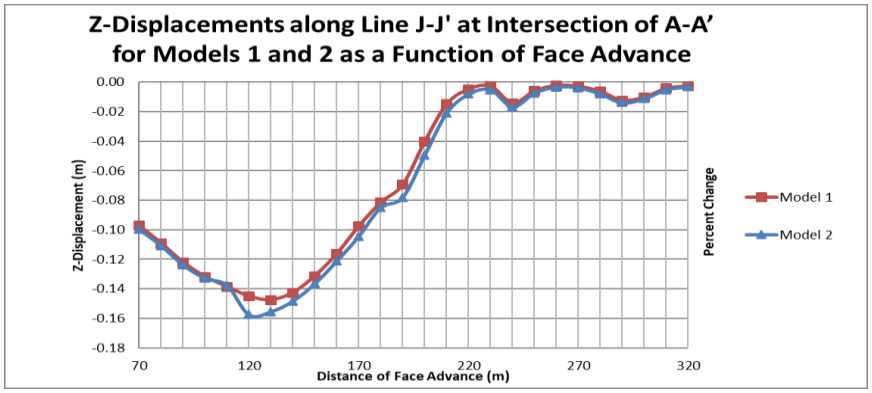

Figure 4.21: Z-displacements in Models 1 and 2 at the face/fault intersection for face advancing from 230 feet (70 m) through 1050 feet (320 m).

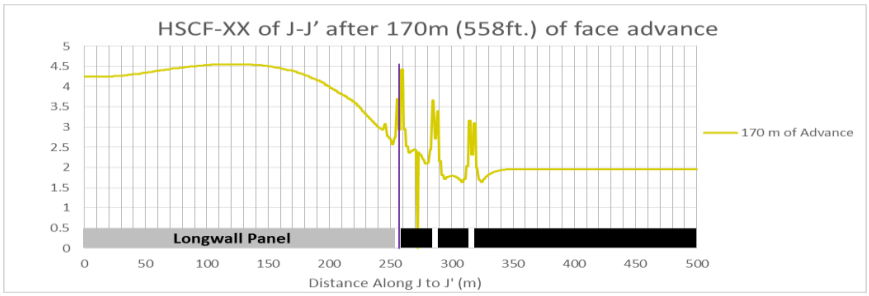

Figure 4.22: HSCF-XX for J-J' after 558 feet (170 m) of face advance.

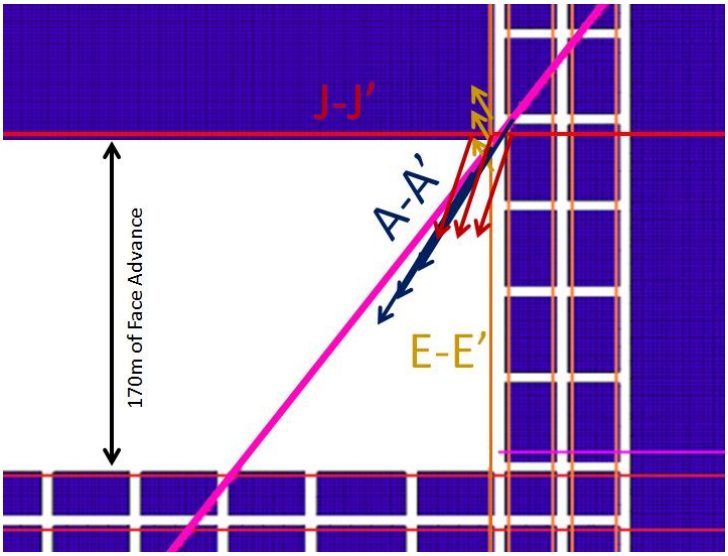

Figure 4.23: Model 2 vectors showing horizontal displacement around face/fault intersection for 558 feet (170 m) of face advance.

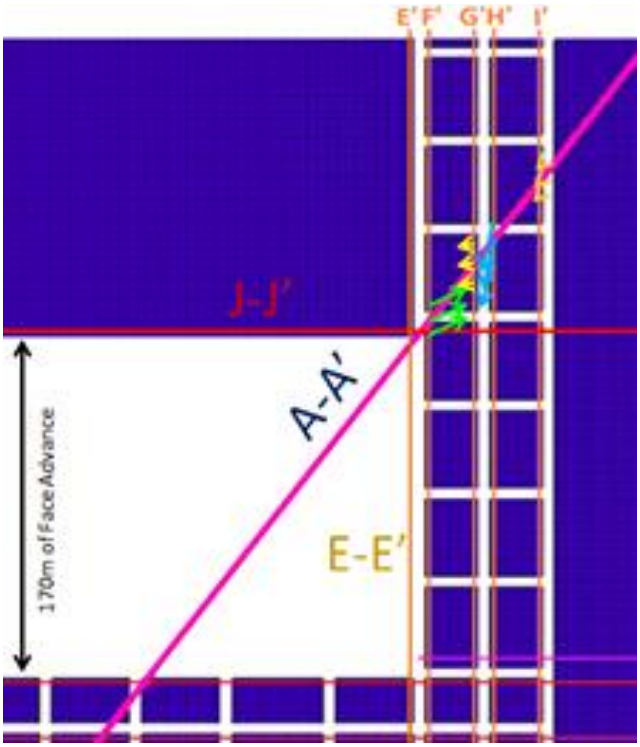

Figure 4.24: Model 2 vectors showing horizontal displacement around gate-entry intersection with fault for 558 feet (170 m) of face advance.

- E-E’ data line
    - VSCF-ZZ did not show any significant change.
    - Displacements in all directions were near zero for Model 1 making the percentage change large in all directions. X-displacement change was positive, and displacement reached 0.5 inches (1.2 cm) in Model 2. Y- and Z-displacements were 0.8 inches (2.1 cm) and -1.1 inches (-2.8 cm), respectively, in Model 2. See Figures 4.23 through 4.26.
    - HSCF-XX and HSCF-YY both increased. HSCF-XX increased by 17% to 2.67 and HSCF-YY increased by 35% to 2.63.

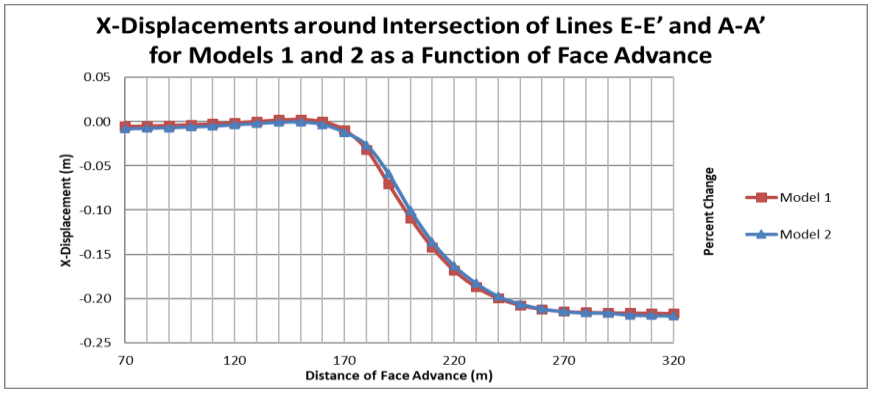

Figure 4.25: X-displacements in Models 1 and 2 at the face/fault intersection of E-E’ for face advancing from 230 feet (70 m) through 1050 feet (320 m).

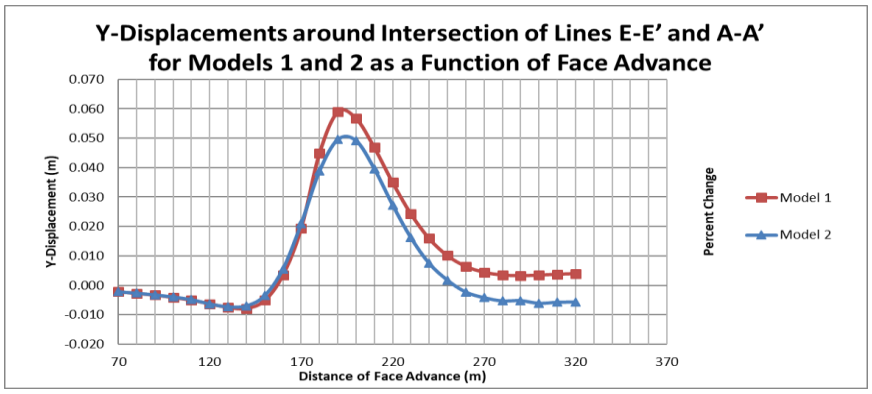

Figure 4.26: Y-displacements in Models 1 and 2 at the face/fault intersection of E-E' for face advancing from 230 feet (70 m) through 1050 feet (320 m).

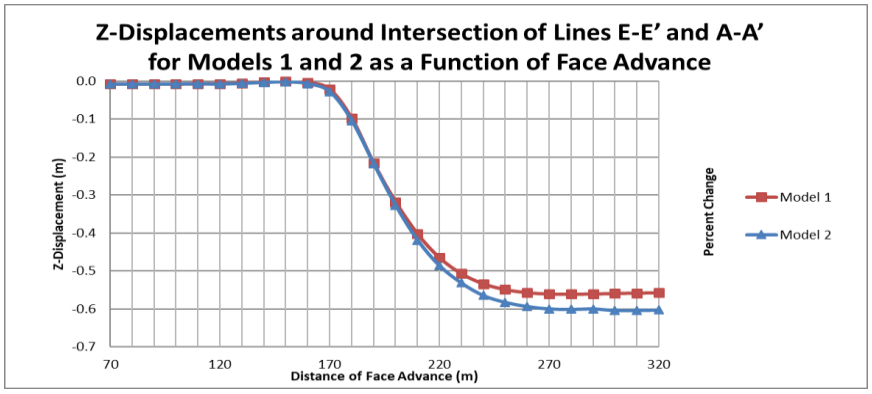

Figure 4.27: Z-displacements in Models 1 and 2 at the face/fault intersection of E-E' for face advancing from 230 feet (70 m) through 1050 feet (320 m).

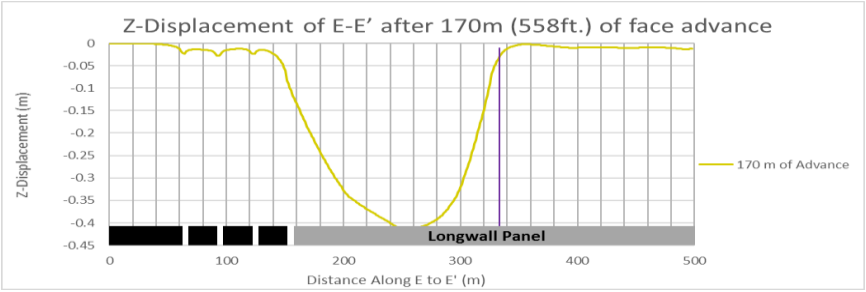

Figure 4.28: Z-displacement of E-E' after 558 feet (170 m) of face advance.

- F-F’ data line
    - As shown in Figures 4.27, 4.28, and 4.29, X- and Y-displacements increased 16% and 86% to 0.43 inches (1.1 cm) and 168% to 0.2 inches (0.5 cm), respectively, while Z-displacements increased 56% to -0.49 inches (-1.24 cm).
    - All horizontal SCFs remained similar between models. VSCF-ZZ increased 13% to 1.45.

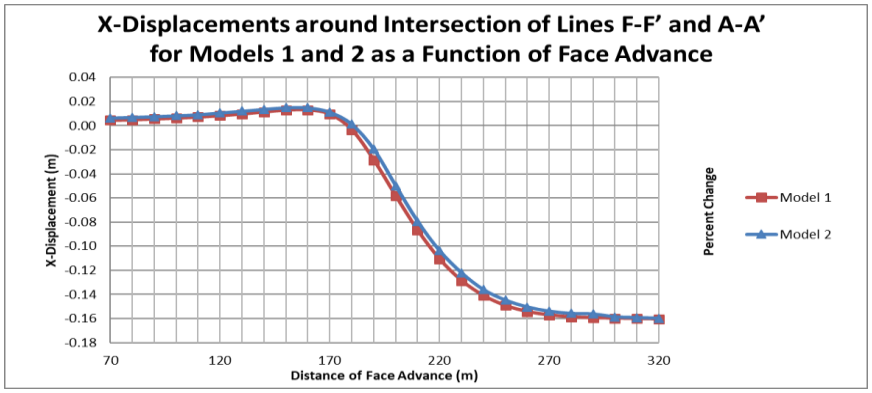

Figure 4.29: X-displacements in Models 1 and 2 at the face/fault intersection of F-F’ for face advancing from 230 feet (70 m) through 1050 feet (320 m).

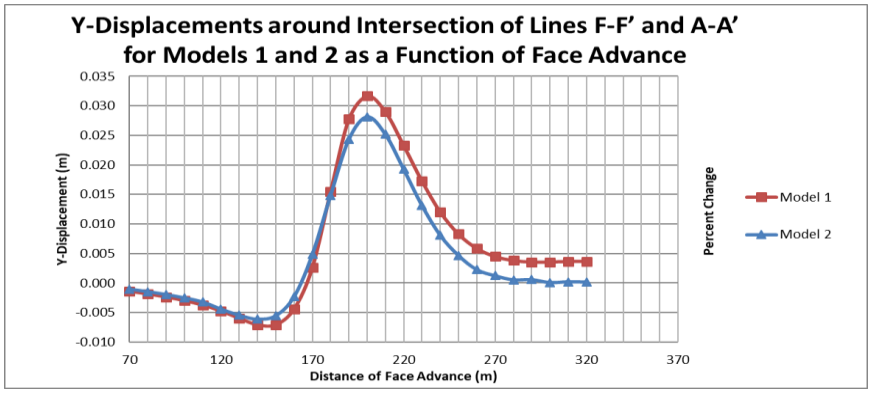

Figure 4.30: Y-displacements in Models 1 and 2 at the face/fault intersection of F-F’ for face advancing from 230 feet (70 m) through 1050 feet (320 m).

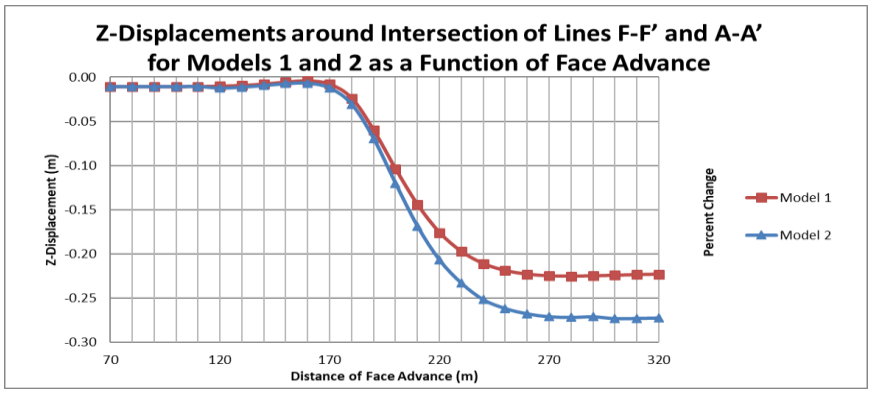

Figure 4.31: Z-displacements in Models 1 and 2 at the face/fault intersection of F-F' for face advancing from 230 feet (70 m) through 1050 feet (320 m).

- G-G' data line
    - All horizontal displacements decreased significantly. X-displacement decreased 131% to -0.04 inches (-0.1 cm), Y-displacement decreased 11% to -0.2 inches (-0.5 cm), and Z-displacement increased 20% to -0.5 inches (-1.2 cm). See Figures 4.30, 4.31, and 4.32
    - None of the SCFs values showed significant change. See Figure 4.33.

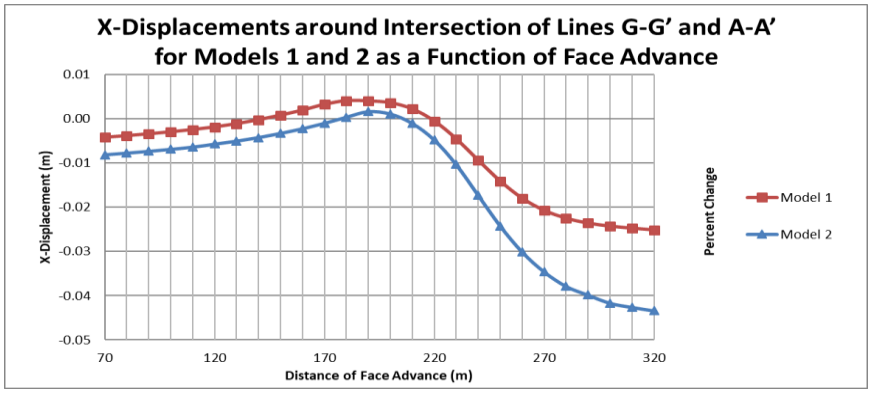

Figure 4.32: X-displacements in Models 1 and 2 at the face/fault intersection of G-G' for face advancing from 230 feet (70 m) through 1050 feet (320 m).

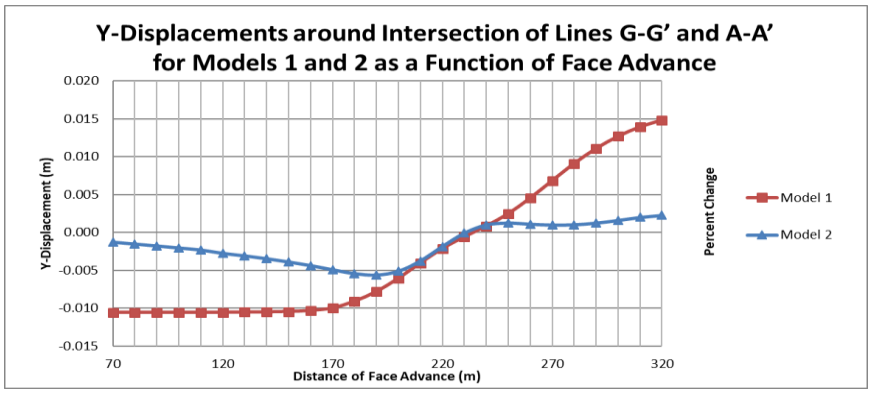

Figure 4.33 Y-displacements in Models 1 and 2 at the face/fault intersection of G-G' for face advancing from 230 feet (70 m) through 1050 feet (320 m).

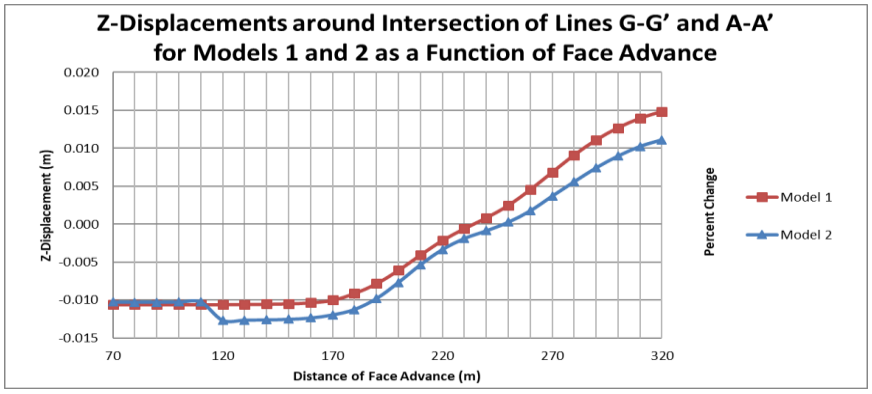

Figure 4.34: Z-displacements in Models 1 and 2 at the face/fault intersection of G-G' for face advancing from 230 feet (70 m) through 1050 feet (320 m).

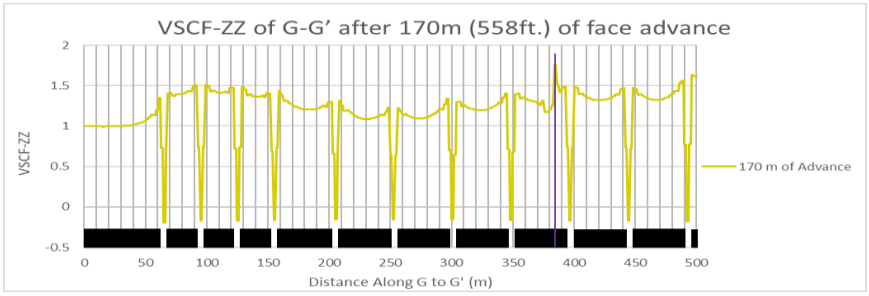

Figure 4.35: VSCF-ZZ of G-G' after 558 feet (170 m) of face advance.

- H-H’ data line
    - X-displacement increased 20% to -0.7 inches (-1.5 cm), Y-displacements decreased 17% to -0.2 inches (-0.4 cm) and Z-displacement increased 24% to -0.7 inches (-1.5 cm). See Figures 4.34, 4.35, and 4.36.
    - SCFs did not show significant change between models.

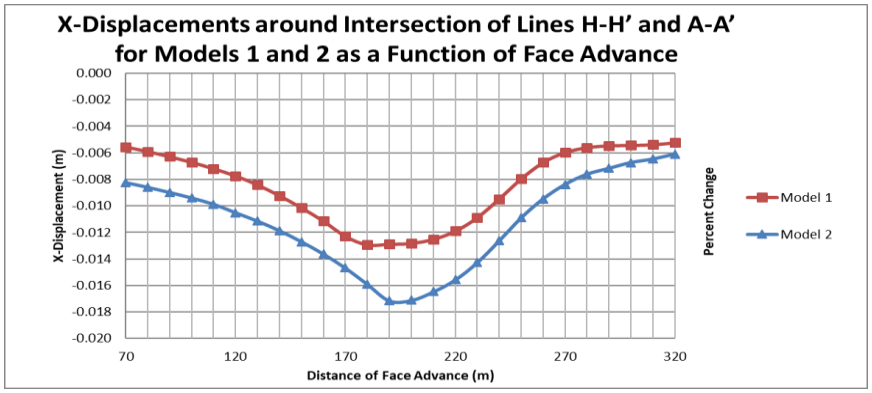

Figure 4.36: X-displacements in Models 1 and 2 at the face/fault intersection of H-H’ for face advancing from 230 feet (70 m) through 1050 feet (320 m).

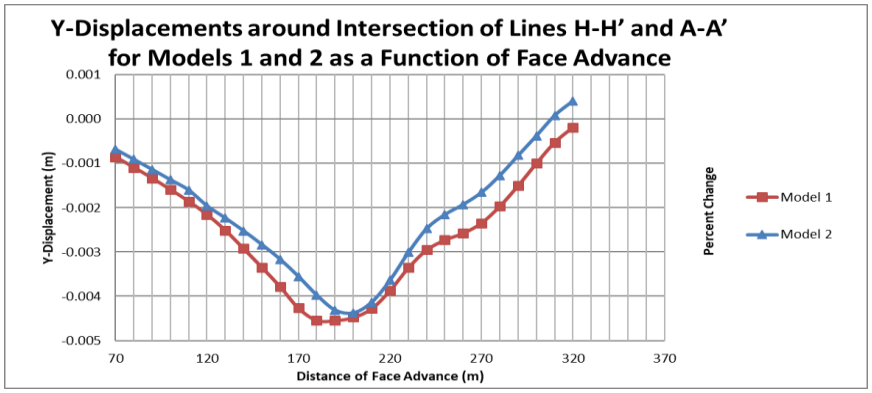

Figure 4.37: Y-displacements between Models 1 and 2 at the face/fault intersection of H-H’ for face advancing from 230 feet (70 m) through 1050 feet (320 m).

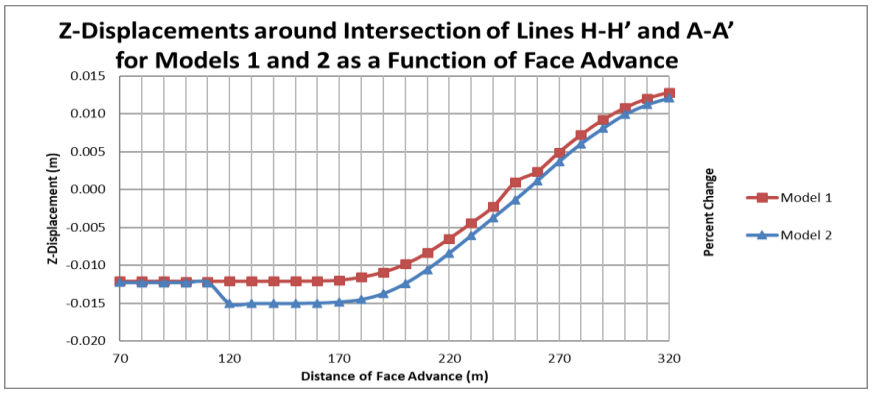

Figure 4.38: Z-displacements in Models 1 and 2 at the face/fault intersection of H-H' for face advancing from 230 feet (70 m) through 1050 feet (320 m).

- I-I' data line
  - X-displacement decreased 204% to -0.01 inches (-0.02 cm), Y-displacements decreased 14% to -0.1 inches (-0.2 cm), and Z-displacement increased 24% to -0.4 inches (-1.1 cm). See Figures 4.37, 4.38, and 4.39.
  - SCFs did not show significant change between models. See Figure 4.38.

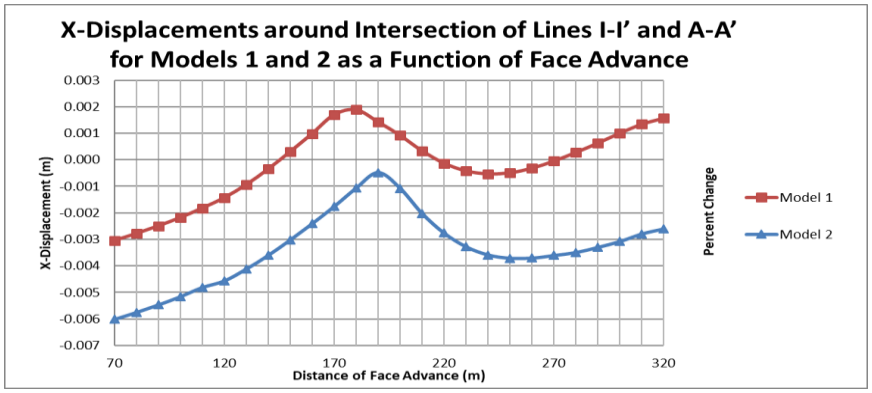

Figure 4.39: X-displacements in Models 1 and 2 at the face/fault intersection of I-I' for face advancing from 230 feet (70 m) through 1050 feet (320 m).

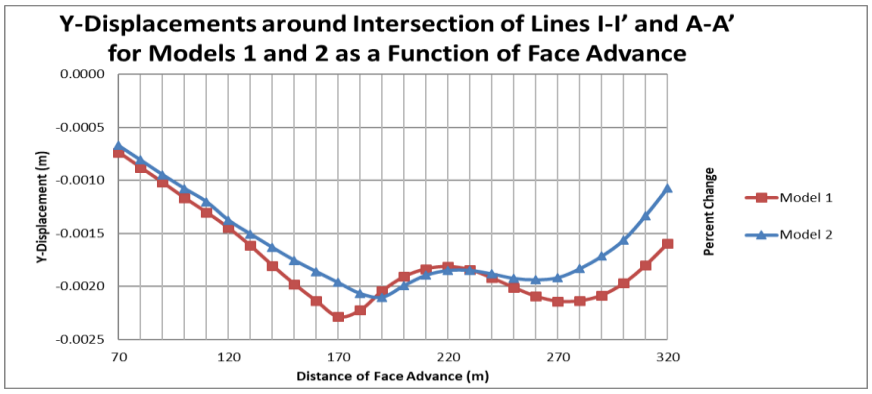

Figure 4.40: Y-displacements in Models 1 and 2 at the face/fault intersection of I-I' for face advancing from 230 feet (70 m) through 1050 feet (320 m).

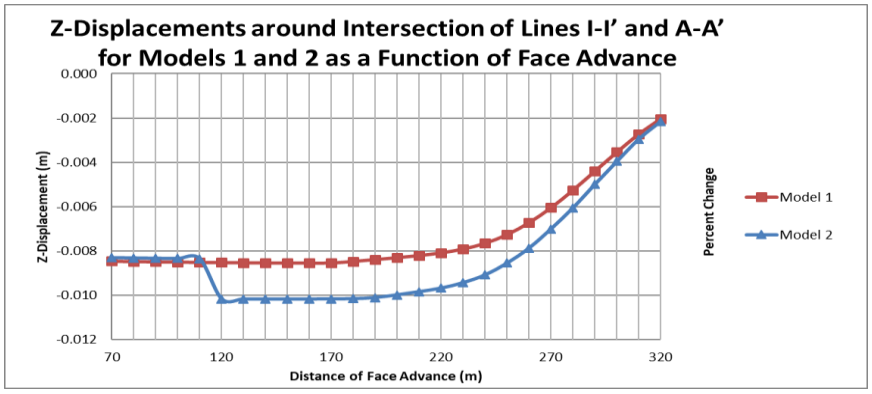

Figure 4.41: Z-displacements in Models 1 and 2 at the face/fault intersection of I-I' for face advancing from 230 feet (70 m) through 1050 feet (320 m).

Table 4.5: Average results for A-A’ data line within ±9.83 feet (3 m) of intersection with the lateral face location for Model 1 advancing from 230 feet (70 m) through 1050 feet (320 m).

Avg (± 3m) Model 1	A-A' x-disp (m)	A-A' y-disp (m)	A-A' z-disp (m)	A-A' HSCF-XX	A-A' HSCF-YY	A-A' VSCF-ZZ
70 m	0.0039	-0.0630	-0.1730	1.88	1.13	0.11
80 m	0.0043	-0.0782	-0.2203	1.84	1.17	0.13
90 m	0.0051	-0.0933	-0.2734	1.71	1.05	0.15
100 m	0.0021	-0.1065	-0.3243	1.57	1.05	0.09
110 m	-0.0011	-0.1168	-0.3709	1.35	0.94	0.04
120 m	-0.0094	-0.1267	-0.4197	1.17	0.91	0.04
130 m	-0.0198	-0.1335	-0.4595	0.96	0.78	0.04
140 m	-0.0330	-0.1328	-0.4765	0.87	0.69	0.04
150 m	-0.0432	-0.1218	-0.4359	0.89	0.77	0.05
160 m	-0.0541	-0.1084	-0.4094	0.94	0.58	0.03
170 m	-0.0635	-0.0914	-0.3631	1.25	0.54	0.02
180 m	-0.0775	-0.0790	-0.3151	2.04	0.72	0.01
190 m	-0.0766	-0.0560	-0.2258	3.14	0.98	0.01
200 m	-0.0579	-0.0326	-0.1071	6.21	1.92	2.37
210 m	-0.0419	-0.0153	-0.0576	4.68	2.03	1.19
220 m	-0.0265	-0.0072	-0.0177	4.00	1.37	1.66
220 m	-0.0165	-0.0022	-0.0036	3.28	1.32	1.09
240 m	-0.0046	0.0018	-0.0016	3.68	1.37	0.72
250 m	0.0080	0.0025	-0.0006	2.97	1.20	0.90
260 m	0.0074	0.0038	-0.0071	2.06	1.28	0.47
270 m	0.0058	0.0032	-0.0010	1.87	0.95	1.08
280 m	0.0026	0.0022	-0.0024	1.70	1.02	1.06
290 m	0.0037	0.0021	-0.0089	2.57	1.17	0.84
300 m	0.0090	0.0015	-0.0053	2.36	1.15	1.00
310 m	0.0055	0.0011	-0.0029	1.68	1.04	1.10
320 m	0.0032	0.0008	-0.0015	1.85	1.06	1.06

Table 4.6: Average results for A-A' data line within ±9.83 feet (3 m) of intersection with the lateral face location for Model 2 advancing from 230 feet (70 m) through 1050 feet (320 m).

Avg (± 3m)	A-A'	A-A'	A-A'	A-A'	A-A'	A-A'
Model 2	x-disp (m)	y-disp (m)	z-disp (m)	HSCF-XX	HSCF-YY	VSCF-ZZ
70 m	0.0038	-0.0670	-0.1789	1.56	0.68	0.10
80 m	0.0041	-0.0834	-0.2277	1.54	0.75	0.12
90 m	0.0051	-0.0989	-0.2809	1.49	0.67	0.07
100 m	0.0019	-0.1131	-0.3339	1.48	0.86	-0.17
110 m	-0.0015	-0.1237	-0.3813	1.31	0.66	-0.30
120 m	-0.0068	-0.1261	-0.4257	1.20	0.61	-0.30
130 m	-0.0155	-0.1277	-0.4517	1.02	0.42	-0.07
140 m	-0.0269	-0.1230	-0.4601	0.93	0.28	-0.06
150 m	-0.0361	-0.1104	-0.4174	0.95	0.29	-0.10
160 m	-0.0463	-0.0964	-0.3905	1.09	0.32	-0.12
170 m	-0.0556	-0.0803	-0.3502	1.28	0.33	-0.09
180 m	-0.0604	-0.0620	-0.2897	1.68	0.38	-0.18
190 m	-0.0619	-0.0444	-0.2225	2.17	0.57	-0.10
200 m	-0.0508	-0.0294	-0.1235	4.24	1.42	1.99
210 m	-0.0403	-0.0146	-0.0725	3.23	1.43	0.65
220 m	-0.0272	-0.0080	-0.0254	3.48	1.38	1.84
220 m	-0.0180	-0.0030	-0.0075	2.81	1.27	1.17
240 m	-0.0056	0.0016	-0.0045	2.87	1.27	0.79
250 m	0.0100	0.0021	-0.0022	2.10	1.00	0.81
260 m	0.0071	0.0038	-0.0103	1.75	0.98	0.50
270 m	0.0051	0.0030	-0.0022	1.98	1.04	1.05
280 m	0.0013	0.0018	-0.0038	1.88	1.05	1.04
290 m	0.0025	0.0018	-0.0115	2.32	1.14	0.93
300 m	0.0095	0.0013	-0.0065	2.05	1.05	0.82
310 m	0.0047	0.0009	-0.0037	1.88	1.07	1.06
320 m	0.0022	0.0006	-0.0019	1.94	1.09	1.06

Table 4.7: Percent change between Models 1 and 2 for A-A' data line within ±9.83 feet (3 m) of Model 2 fault intersection for face advancing from 230 feet (70 m) through 1050 feet (320 m).

Avg (± 3m) Change	A-A' x-disp (%)	A-A' y-disp (%)	A-A' z-disp (%)	A-A' HSCF-XX (%)	A-A' HSCF-YY (%)	A-A' VSCF-ZZ (%)
70 m	-1	6	3	-17	-40	-10
80 m	-5	7	3	-17	-36	-9
90 m	0	6	3	-13	-36	-55
100 m	-11	6	3	-6	-18	-287
110 m	33	6	3	-3	-30	-812
120 m	-28	0	1	3	-33	-862
130 m	-22	-4	-2	6	-47	-267
140 m	-18	-7	-3	7	-59	-271
150 m	-16	-9	-4	6	-62	-323
160 m	-14	-11	-5	15	-45	-497
170 m	-12	-12	-4	3	-39	-586
180 m	-22	-22	-8	-18	-47	-1470
190 m	-19	-21	-1	-31	-42	-747
200 m	-12	-10	15	-32	-26	-16
210 m	-4	-4	26	-31	-30	-45
220 m	3	12	44	-13	1	11
230 m	9	36	111	-14	-4	7
240 m	23	-14	177	-22	-7	10
250 m	25	-18	280	-29	-16	-10
260 m	-4	0	45	-15	-23	5
270 m	-13	-8	120	6	9	-2
280 m	-52	-17	57	11	3	-2
290 m	-32	-12	29	-10	-3	12
300 m	6	-14	24	-13	-9	-18
310 m	-14	-17	27	12	3	-3
320 m	-30	-22	28	5	2	0

Table 4.8: Average results for Model 1 J-J' data line within ±9.83 feet (3 m) of intersection with Model 2 fault for face advancing from 230 feet (70 m) through 1050 feet (320 m).

Avg (± 3m)	J-J'	J-J'	J-J'	J-J'	J-J'	J-J'
Model 1	x-disp (m)	y-disp (m)	z-disp (m)	HSCF-XX	HSCF-YY	VSCF-ZZ
70 m	0.0031	-0.0520	-0.0971	3.20	3.64	4.33
80 m	0.0035	-0.0619	-0.1090	3.36	4.19	4.74
90 m	0.0040	-0.0717	-0.1219	3.50	4.72	5.18
100 m	0.0029	-0.0798	-0.1317	3.62	5.18	5.53
110 m	0.0016	-0.0855	-0.1385	3.68	5.53	5.77
120 m	-0.0017	-0.0909	-0.1451	3.73	5.90	6.03
130 m	-0.0056	-0.0935	-0.1475	3.73	6.12	6.16
140 m	-0.0100	-0.0908	-0.1426	3.67	6.09	6.05
150 m	-0.0136	-0.0831	-0.1313	3.54	5.76	5.71
160 m	-0.0167	-0.0727	-0.1162	3.38	5.29	5.25
170 m	-0.0192	-0.0601	-0.0976	3.20	4.70	4.66
180 m	-0.0248	-0.0512	-0.0815	3.08	4.22	4.12
190 m	-0.0254	-0.0389	-0.0694	3.01	3.33	3.09
200 m	-0.0152	-0.0230	-0.0403	3.76	2.55	0.97
210 m	-0.0094	-0.0123	-0.0148	2.72	1.94	1.55
220 m	-0.0066	-0.0053	-0.0046	2.53	1.55	1.16
230 m	-0.0043	-0.0016	-0.0025	2.35	1.20	1.07
240 m	0.0021	0.0023	-0.0141	2.49	1.49	0.53
250 m	0.0073	0.0030	-0.0058	2.85	1.15	0.60
260 m	0.0071	0.0026	-0.0021	1.82	1.07	1.04
270 m	0.0044	0.0024	-0.0027	1.80	1.04	1.09
280 m	0.0018	0.0009	-0.0060	1.78	0.98	1.21
290 m	0.0018	0.0027	-0.0122	2.05	1.05	1.24
300 m	0.0055	0.0012	-0.0100	2.58	1.11	0.63
310 m	0.0056	0.0008	-0.0041	1.78	1.07	1.12
320 m	0.0029	0.0006	-0.0024	1.82	1.06	1.08

Table 4.9: Average results for Model 2 J-J' data line within ±9.83 feet (3 m) of intersection with Model 2 fault for face advancing from 230 feet (70 m) through 1050 feet (320 m).

Avg (± 3m) Model 2	J-J' x-disp (m)	J-J' y-disp (m)	J-J' z-disp (m)	J-J' HSCF-XX	J-J' HSCF-YY	J-J' VSCF-ZZ
70 m	0.0026	-0.0536	-0.0997	3.35	3.12	4.33
80 m	0.0028	-0.0620	-0.1107	3.50	3.45	4.85
90 m	0.0035	-0.0725	-0.1238	3.59	3.65	4.67
100 m	0.0026	-0.0798	-0.1327	3.77	4.67	5.99
110 m	0.0017	-0.0828	-0.1375	3.85	4.81	6.15
120 m	0.0002	-0.0873	-0.1576	3.65	4.81	5.27
130 m	-0.0029	-0.0860	-0.1554	3.61	5.36	5.77
140 m	-0.0066	-0.0816	-0.1482	3.52	5.23	5.56
150 m	-0.0099	-0.0753	-0.1365	3.35	4.94	5.01
160 m	-0.0131	-0.0658	-0.1212	3.18	4.56	4.59
170 m	-0.0164	-0.0563	-0.1044	3.00	4.12	4.11
180 m	-0.0195	-0.0446	-0.0849	2.75	3.58	3.57
190 m	-0.0215	-0.0365	-0.0780	2.79	2.98	2.81
200 m	-0.0138	-0.0250	-0.0496	3.73	2.49	0.97
210 m	-0.0100	-0.0150	-0.0210	2.75	1.97	1.60
220 m	-0.0081	-0.0075	-0.0081	2.57	1.61	1.23
230 m	-0.0068	-0.0031	-0.0051	2.37	1.24	1.10
240 m	0.0004	0.0010	-0.0167	2.56	1.56	0.54
250 m	0.0065	0.0021	-0.0074	2.94	1.18	0.61
260 m	0.0065	0.0020	-0.0033	1.85	1.09	1.04
270 m	0.0034	0.0021	-0.0038	1.79	1.06	1.10
280 m	0.0008	0.0008	-0.0079	1.76	0.98	1.18
290 m	0.0012	0.0024	-0.0140	2.05	1.05	1.22
300 m	0.0049	0.0011	-0.0113	2.59	1.12	0.64
310 m	0.0049	0.0008	-0.0052	1.78	1.07	1.11
320 m	0.0020	0.0006	-0.0031	1.81	1.07	1.09

Table 4.10: Percent change in J-J' data line within ±9.83 feet (3 m) of Model 2 fault intersection for face advancing from 230 feet (70 m) through 1050 feet (320 m).

Avg (± 3m) Change	J-J' x-disp (%)	J-J' y-disp (%)	J-J' z-disp (%)	J-J' HSCF-XX (%)	J-J' HSCF-YY (%)	J-J' VSCF-ZZ (%)
70 m	-17	3	3	5	-14	0
80 m	-20	0	2	4	-18	2
90 m	-12	1	2	3	-23	-10
100 m	-10	0	1	4	-10	8
110 m	1	-3	-1	5	-13	7
120 m	-110	-4	9	-2	-18	-13
130 m	-48	-8	5	-3	-13	-6
140 m	-34	-10	4	-4	-14	-8
150 m	-27	-9	4	-5	-14	-12
160 m	-22	-9	4	-6	-14	-13
170 m	-15	-6	7	-6	-12	-12
180 m	-21	-13	4	-11	-15	-13
190 m	-15	-6	12	-7	-11	-9
200 m	-9	8	23	-1	-3	0
210 m	6	22	42	1	2	3
220 m	23	42	75	2	4	6
230 m	59	92	104	1	3	2
240 m	-82	-55	19	2	4	2
250 m	-11	-29	28	3	3	2
260 m	-9	-23	58	2	2	0
270 m	-22	-15	41	-1	2	1
280 m	-58	-14	31	-1	0	-3
290 m	-36	-8	14	0	0	-2
300 m	-12	-11	12	0	1	0
310 m	-12	-3	25	0	0	-1
320 m	-29	4	27	-1	0	1

Table 4.11: Average results for Model 1 E-E' data line within ±9.83 feet (3 m) of intersection with Model 2 fault for face advancing from 230 feet (70 m) through 1050 feet (320 m).

Avg (± 3m)	E-E'	E-E'	E-E'	E-E'	E-E'	E-E'
Model 1	x-disp (m)	y-disp (m)	z-disp (m)	HSCF-XX	HSCF-YY	VSCF-ZZ
70 m	-0.0053	-0.0022	-0.0079	2.08	1.15	1.27
80 m	-0.0047	-0.0027	-0.0079	2.08	1.14	1.27
90 m	-0.0040	-0.0033	-0.0079	2.08	1.14	1.27
100 m	-0.0032	-0.0041	-0.0078	2.08	1.12	1.27
110 m	-0.0023	-0.0050	-0.0075	2.08	1.11	1.26
120 m	-0.0010	-0.0063	-0.0067	2.08	1.10	1.25
130 m	0.0006	-0.0075	-0.0051	2.08	1.13	1.21
140 m	0.0021	-0.0079	-0.0026	2.11	1.25	1.15
150 m	0.0027	-0.0051	-0.0005	2.18	1.56	1.11
160 m	0.0002	0.0035	-0.0034	2.35	2.13	1.23
170 m	-0.0092	0.0194	-0.0219	2.60	2.58	1.98
180 m	-0.0315	0.0449	-0.0983	2.85	2.38	0.26
190 m	-0.0705	0.0589	-0.2165	3.07	1.13	-0.02
200 m	-0.1092	0.0567	-0.3189	3.47	0.57	-0.03
210 m	-0.1425	0.0468	-0.4032	3.89	0.42	-0.03
220 m	-0.1686	0.0349	-0.4656	4.28	0.53	-0.04
230 m	-0.1872	0.0243	-0.5077	4.34	0.91	-0.04
240 m	-0.1997	0.0159	-0.5340	4.55	1.11	-0.04
250 m	-0.2076	0.0101	-0.5494	4.69	1.27	-0.04
260 m	-0.2122	0.0065	-0.5573	4.76	1.39	-0.05
270 m	-0.2145	0.0045	-0.5608	4.80	1.46	-0.05
280 m	-0.2156	0.0035	-0.5615	4.81	1.51	-0.05
290 m	-0.2161	0.0033	-0.5607	4.82	1.54	-0.05
300 m	-0.2163	0.0035	-0.5594	4.82	1.55	-0.05
310 m	-0.2165	0.0038	-0.5583	4.81	1.54	-0.05
320 m	-0.2169	0.0040	-0.5574	4.81	1.53	-0.05

Table 4.12: Average results for Model 2 E-E' data line within ±9.83 feet (3 m) of intersection with Model 2 fault for face advancing from 230 feet (70 m) through 1050 feet (320 m).

Avg (± 3m) Model 2	E-E' x-disp (m)	E-E' y-disp (m)	E-E' z-disp (m)	E-E' HSCF-XX	E-E' HSCF-YY	E-E' VSCF-ZZ
70 m	-0.0081	-0.0022	-0.0079	2.02	1.13	1.16
80 m	-0.0075	-0.0027	-0.0079	2.02	1.13	1.16
90 m	-0.0069	-0.0032	-0.0078	2.02	1.13	1.16
100 m	-0.0061	-0.0039	-0.0077	2.02	1.12	1.16
110 m	-0.0051	-0.0048	-0.0074	2.02	1.11	1.15
120 m	-0.0035	-0.0063	-0.0079	2.02	1.11	1.13
130 m	-0.0021	-0.0073	-0.0061	2.02	1.12	1.10
140 m	-0.0008	-0.0069	-0.0036	2.03	1.17	1.06
150 m	-0.0005	-0.0035	-0.0022	2.05	1.29	1.05
160 m	-0.0032	0.0056	-0.0069	2.21	1.61	1.21
170 m	-0.0122	0.0210	-0.0282	2.38	1.87	1.87
180 m	-0.0264	0.0388	-0.1044	1.72	1.01	0.14
190 m	-0.0588	0.0495	-0.2181	1.77	0.48	-0.04
200 m	-0.1006	0.0491	-0.3278	2.01	0.34	-0.04
210 m	-0.1361	0.0395	-0.4193	2.23	0.34	-0.04
220 m	-0.1632	0.0273	-0.4865	2.41	0.44	-0.03
230 m	-0.1828	0.0162	-0.5321	4.67	0.55	-0.08
240 m	-0.1974	0.0075	-0.5651	4.99	0.82	-0.07
250 m	-0.2061	0.0018	-0.5829	5.36	1.06	-0.04
260 m	-0.2116	-0.0022	-0.5939	5.49	1.18	-0.04
270 m	-0.2148	-0.0041	-0.6000	5.56	1.30	-0.03
280 m	-0.2162	-0.0053	-0.6013	5.60	1.39	-0.03
290 m	-0.2164	-0.0052	-0.6000	5.61	1.43	-0.03
300 m	-0.2187	-0.0061	-0.6043	5.63	1.44	-0.02
310 m	-0.2192	-0.0057	-0.6040	5.62	1.44	-0.03
320 m	-0.2198	-0.0056	-0.6032	5.62	1.43	-0.03

Table 4.13: Percent change on E-E' within ±9.83 feet (3 m) of intersection with Model 2 fault for face advancing from 230 feet (70 m) through 1050 feet (320 m).

Avg (± 3m) Change	E-E' x-disp (%)	E-E' y-disp (%)	E-E' z-disp (%)	E-E' HSCF-XX (%)	E-E' HSCF-YY (%)	E-E' VSCF-ZZ (%)
70 m	53	-1	-1	-3	-2	-9
80 m	60	-2	-1	-3	-1	-9
90 m	70	-3	-1	-3	-1	-9
100 m	88	-3	-1	-3	0	-9
110 m	125	-4	-1	-3	0	-9
120 m	254	1	18	-3	1	-9
130 m	-477	-3	20	-3	-1	-9
140 m	-135	-12	39	-4	-7	-8
150 m	-118	-32	315	-6	-18	-5
160 m	-2135	59	100	-6	-24	-2
170 m	32	8	29	-8	-28	-5
180 m	-16	-14	6	-40	-57	-48
190 m	-17	-16	1	-43	-58	68
200 m	-8	-13	3	-42	-41	43
210 m	-4	-16	4	-43	-19	6
220 m	-3	-22	4	-44	-16	-20
230 m	-2	-33	5	8	-40	102
240 m	-1	-53	6	10	-26	64
250 m	-1	-82	6	14	-17	-20
260 m	0	-135	7	15	-15	-16
270 m	0	-193	7	16	-11	-29
280 m	0	-248	7	16	-8	-38
290 m	0	-255	7	16	-7	-41
300 m	1	-273	8	17	-7	-47
310 m	1	-250	8	17	-7	-46
320 m	1	-240	8	17	-7	-45

Table 4.14: Average results for Model 1 F-F' data line within ±9.83 feet (3 m) of intersection with Model 2 fault for face advancing from 230 feet (70 m) through 1050 feet (320 m).

Avg (± 3m) Model 1	F-F' x-disp (m)	F-F' y-disp (m)	F-F' z-disp (m)	F-F' HSCF-XX	F-F' HSCF-YY	F-F' VSCF-ZZ
70 m	0.0044	-0.0014	-0.0108	2.05	1.09	1.34
80 m	0.0049	-0.0019	-0.0108	2.05	1.08	1.34
90 m	0.0055	-0.0024	-0.0108	2.05	1.08	1.34
100 m	0.0062	-0.0030	-0.0107	2.04	1.07	1.34
110 m	0.0071	-0.0037	-0.0106	2.04	1.06	1.34
120 m	0.0082	-0.0047	-0.0103	2.03	1.04	1.33
130 m	0.0097	-0.0060	-0.0094	2.02	1.04	1.30
140 m	0.0114	-0.0071	-0.0078	2.00	1.07	1.26
150 m	0.0129	-0.0071	-0.0056	2.02	1.17	1.19
160 m	0.0131	-0.0044	-0.0042	2.09	1.39	1.15
170 m	0.0096	0.0026	-0.0080	2.37	1.73	1.28
180 m	-0.0035	0.0154	-0.0240	3.03	2.07	1.94
190 m	-0.0285	0.0277	-0.0603	4.26	2.17	3.39
200 m	-0.0583	0.0317	-0.1043	5.62	2.28	4.90
210 m	-0.0869	0.0290	-0.1446	6.89	2.54	6.19
220 m	-0.1107	0.0233	-0.1760	7.93	2.88	7.16
230 m	-0.1286	0.0173	-0.1976	8.72	3.21	7.82
240 m	-0.1411	0.0120	-0.2112	9.26	3.49	8.23
250 m	-0.1493	0.0083	-0.2190	9.61	3.69	8.47
260 m	-0.1543	0.0059	-0.2231	9.80	3.82	8.58
270 m	-0.1572	0.0045	-0.2250	9.90	3.89	8.63
280 m	-0.1586	0.0038	-0.2254	9.93	3.93	8.63
290 m	-0.1594	0.0035	-0.2250	9.93	3.94	8.62
300 m	-0.1598	0.0035	-0.2243	9.91	3.94	8.60
310 m	-0.1601	0.0036	-0.2236	9.89	3.92	8.58
320 m	-0.1604	0.0037	-0.2231	9.87	3.91	8.56

Table 4.15: Average results for Model 2 F-F' data line within ±9.83 feet (3 m) of intersection with Model 2 fault for face advancing from 230 feet (70 m) through 1050 feet (320 m).

Avg (± 3m) Model 2	F-F' x-disp (m)	F-F' y-disp (m)	F-F' z-disp (m)	F-F' HSCF-XX	F-F' HSCF-YY	F-F' VSCF-ZZ
70 m	0.0064	-0.0011	-0.0109	1.91	1.08	1.50
80 m	0.0069	-0.0015	-0.0109	1.91	1.08	1.50
90 m	0.0075	-0.0020	-0.0109	1.91	1.07	1.50
100 m	0.0082	-0.0025	-0.0108	1.90	1.06	1.50
110 m	0.0091	-0.0032	-0.0107	1.90	1.05	1.49
120 m	0.0106	-0.0044	-0.0124	1.89	1.03	1.47
130 m	0.0120	-0.0055	-0.0114	1.88	1.03	1.44
140 m	0.0136	-0.0061	-0.0095	1.87	1.07	1.39
150 m	0.0149	-0.0055	-0.0074	1.88	1.18	1.33
160 m	0.0148	-0.0023	-0.0069	1.96	1.39	1.31
170 m	0.0112	0.0048	-0.0124	2.23	1.71	1.45
180 m	0.0011	0.0148	-0.0309	2.75	1.93	2.08
190 m	-0.0195	0.0243	-0.0699	3.75	1.96	3.39
200 m	-0.0499	0.0282	-0.1208	5.02	2.08	4.81
210 m	-0.0795	0.0252	-0.1692	6.15	2.31	6.00
220 m	-0.1038	0.0193	-0.2071	7.05	2.60	6.88
230 m	-0.1222	0.0131	-0.2333	7.69	2.83	7.42
240 m	-0.1361	0.0081	-0.2519	8.20	3.13	7.92
250 m	-0.1448	0.0047	-0.2618	8.50	3.32	8.14
260 m	-0.1505	0.0023	-0.2679	8.65	3.43	8.34
270 m	-0.1540	0.0012	-0.2710	8.62	3.50	8.47
280 m	-0.1558	0.0005	-0.2718	8.66	3.54	8.49
290 m	-0.1563	0.0006	-0.2711	8.65	3.54	8.46
300 m	-0.1586	0.0001	-0.2732	8.78	3.63	8.83
310 m	-0.1592	0.0002	-0.2730	8.77	3.62	8.82
320 m	-0.1598	0.0001	-0.2725	8.76	3.61	8.81

Table 4.16: Percent change on F-F' within ±9.83 feet (3 m) of intersection with Model 2 fault for face advancing from 230 feet (70 m) through 1050 feet (320 m).

Avg (± 3m) Change	F-F' x-disp (%)	F-F' y-disp (%)	F-F' z-disp (%)	F-F' HSCF-XX (%)	F-F' HSCF-YY (%)	F-F' VSCF-ZZ (%)
70 m	46	-25	1	-7	-1	11
80 m	41	-20	1	-7	-1	11
90 m	36	-17	1	-7	-1	11
100 m	32	-15	1	-7	-1	11
110 m	28	-13	1	-7	-1	11
120 m	29	-7	21	-7	-1	11
130 m	24	-8	21	-7	-1	11
140 m	19	-13	22	-7	0	11
150 m	15	-22	34	-7	1	12
160 m	13	-47	63	-7	1	14
170 m	16	86	56	-6	-1	13
180 m	-133	-4	28	-9	-7	7
190 m	-32	-12	16	-12	-9	0
200 m	-14	-11	16	-11	-9	-2
210 m	-9	-13	17	-11	-9	-3
220 m	-6	-17	18	-11	-10	-4
230 m	-5	-24	18	-12	-12	-5
240 m	-4	-33	19	-11	-10	-4
250 m	-3	-44	20	-12	-10	-4
260 m	-2	-62	20	-12	-10	-3
270 m	-2	-73	20	-13	-10	-2
280 m	-2	-86	21	-13	-10	-2
290 m	-2	-84	20	-13	-10	-2
300 m	-1	-98	22	-11	-8	3
310 m	-1	-94	22	-11	-8	3
320 m	0	-96	22	-11	-8	3

Table 4.17: Average results for Model 1 G-G' data line within ±9.83 feet (3 m) of intersection with Model 2 fault for face advancing from 230 feet (70 m) through 1050 feet (320 m).

Avg (± 3m) Model 1	G-G' x-disp (m)	G-G' y-disp (m)	G-G' z-disp (m)	G-G' HSCF-XX	G-G' HSCF-YY	G-G' VSCF-ZZ
70 m	-0.0042	-0.0013	-0.0106	2.07	1.16	1.33
80 m	-0.0038	-0.0016	-0.0106	2.07	1.16	1.33
90 m	-0.0034	-0.0019	-0.0106	2.07	1.15	1.33
100 m	-0.0030	-0.0022	-0.0106	2.07	1.15	1.33
110 m	-0.0024	-0.0025	-0.0106	2.07	1.15	1.33
120 m	-0.0019	-0.0028	-0.0106	2.07	1.15	1.33
130 m	-0.0011	-0.0033	-0.0106	2.06	1.14	1.33
140 m	-0.0002	-0.0038	-0.0105	2.06	1.14	1.33
150 m	0.0008	-0.0043	-0.0105	2.06	1.13	1.33
160 m	0.0019	-0.0049	-0.0103	2.06	1.12	1.33
170 m	0.0033	-0.0056	-0.0100	2.05	1.12	1.33
180 m	0.0041	-0.0060	-0.0091	2.05	1.11	1.31
190 m	0.0040	-0.0059	-0.0078	2.07	1.13	1.29
200 m	0.0036	-0.0053	-0.0061	2.11	1.17	1.25
210 m	0.0022	-0.0042	-0.0041	2.22	1.23	1.20
220 m	-0.0005	-0.0027	-0.0022	2.43	1.27	1.16
230 m	-0.0045	-0.0014	-0.0006	2.72	1.29	1.11
240 m	-0.0094	-0.0007	0.0008	3.07	1.31	1.07
250 m	-0.0141	-0.0008	0.0025	3.41	1.34	1.01
260 m	-0.0180	-0.0011	0.0045	3.70	1.39	0.96
270 m	-0.0207	-0.0013	0.0068	3.92	1.43	0.90
280 m	-0.0225	-0.0013	0.0091	4.08	1.46	0.85
290 m	-0.0236	-0.0010	0.0111	4.19	1.48	0.81
300 m	-0.0243	-0.0007	0.0127	4.25	1.49	0.78
310 m	-0.0247	-0.0003	0.0139	4.29	1.49	0.76
320 m	-0.0251	0.0000	0.0148	4.32	1.48	0.75

Table 4.18: Average results for Model 2 G-G' data line within ±9.83 feet (3 m) of intersection with Model 2 fault for face advancing from 230 feet (70 m) through 1050 feet (320 m).

Avg (± 3m) Model 2	G-G' x-disp (m)	G-G' y-disp (m)	G-G' z-disp (m)	G-G' HSCF-XX	G-G' HSCF-YY	G-G' VSCF-ZZ
70 m	-0.0081	-0.0013	-0.0103	1.95	1.14	1.20
80 m	-0.0077	-0.0015	-0.0103	1.95	1.13	1.20
90 m	-0.0073	-0.0018	-0.0103	1.95	1.13	1.20
100 m	-0.0069	-0.0021	-0.0103	1.95	1.13	1.20
110 m	-0.0064	-0.0023	-0.0103	1.95	1.13	1.20
120 m	-0.0057	-0.0028	-0.0127	1.96	1.14	1.22
130 m	-0.0050	-0.0031	-0.0127	1.96	1.14	1.22
140 m	-0.0042	-0.0035	-0.0126	1.96	1.14	1.22
150 m	-0.0033	-0.0039	-0.0125	1.96	1.14	1.22
160 m	-0.0022	-0.0044	-0.0124	1.96	1.13	1.21
170 m	-0.0010	-0.0049	-0.0120	1.96	1.13	1.21
180 m	0.0004	-0.0055	-0.0112	1.96	1.13	1.20
190 m	0.0016	-0.0057	-0.0098	1.96	1.13	1.18
200 m	0.0011	-0.0052	-0.0077	1.97	1.13	1.16
210 m	-0.0010	-0.0038	-0.0054	2.00	1.14	1.13
220 m	-0.0048	-0.0019	-0.0034	2.05	1.15	1.10
230 m	-0.0103	-0.0001	-0.0019	2.14	1.14	1.06
240 m	-0.0173	0.0010	-0.0009	2.20	1.14	1.03
250 m	-0.0242	0.0012	0.0003	2.22	1.14	1.02
260 m	-0.0301	0.0011	0.0017	2.22	1.15	1.00
270 m	-0.0346	0.0010	0.0037	2.22	1.15	0.98
280 m	-0.0379	0.0010	0.0056	2.20	1.15	0.97
290 m	-0.0399	0.0012	0.0074	2.19	1.14	0.95
300 m	-0.0417	0.0016	0.0090	2.18	1.14	0.94
310 m	-0.0426	0.0020	0.0102	2.18	1.14	0.93
320 m	-0.0434	0.0022	0.0111	2.17	1.13	0.93

Table 4.19: Percent change on G-G' within ±9.83 feet (3 m) of intersection with Model 2 fault for face advancing from 230 feet (70 m) through 1050 feet (320 m).

Avg (± 3m) Change	G-G' x-disp (%)	G-G' y-disp (%)	G-G' z-disp (%)	G-G' HSCF-XX (%)	G-G' HSCF-YY (%)	G-G' VSCF-ZZ (%)
70 m	94	-3	-3	-6	-2	-10
80 m	102	-4	-3	-6	-2	-10
90 m	115	-4	-3	-6	-2	-10
100 m	133	-5	-3	-5	-2	-10
110 m	161	-6	-3	-5	-1	-10
120 m	208	-2	20	-5	-1	-9
130 m	349	-4	20	-5	0	-9
140 m	1774	-7	20	-5	0	-9
150 m	-516	-9	20	-5	0	-9
160 m	-215	-11	20	-5	1	-9
170 m	-131	-11	20	-4	1	-9
180 m	-91	-9	23	-5	1	-9
190 m	-60	-4	25	-5	0	-8
200 m	-70	-3	26	-7	-4	-7
210 m	-147	-10	32	-10	-7	-6
220 m	848	-31	55	-15	-10	-5
230 m	128	-92	218	-22	-12	-5
240 m	85	-234	-206	-28	-13	-3
250 m	72	-256	-90	-35	-15	0
260 m	68	-198	-61	-40	-17	4
270 m	67	-174	-46	-43	-20	9
280 m	68	-180	-39	-46	-22	13
290 m	69	-221	-33	-48	-23	17
300 m	72	-337	-29	-49	-24	20
310 m	72	-750	-26	-49	-24	22
320 m	73	-5558	-25	-50	-24	24

Table 4.20: Average results for Model 1 H-H' data line within ±9.83 feet (3 m) of intersection with Model 2 fault for face advancing from 230 feet (70 m) through 1050 feet (320 m).

Avg (± 3m)	H-H'	H-H'	H-H'	H-H'	H-H'	H-H'
Model 1	x-disp (m)	y-disp (m)	z-disp (m)	HSCF-XX	HSCF-YY	VSCF-ZZ
70 m	-0.0055	-0.0009	-0.0121	2.05	1.10	1.38
80 m	-0.0059	-0.0011	-0.0121	2.05	1.10	1.38
90 m	-0.0063	-0.0013	-0.0121	2.05	1.10	1.38
100 m	-0.0067	-0.0016	-0.0121	2.05	1.10	1.38
110 m	-0.0072	-0.0019	-0.0121	2.05	1.09	1.38
120 m	-0.0077	-0.0022	-0.0121	2.04	1.09	1.38
130 m	-0.0084	-0.0025	-0.0121	2.04	1.09	1.38
140 m	-0.0092	-0.0029	-0.0121	2.04	1.09	1.38
150 m	-0.0101	-0.0033	-0.0121	2.03	1.08	1.38
160 m	-0.0111	-0.0038	-0.0121	2.02	1.07	1.38
170 m	-0.0123	-0.0043	-0.0120	2.01	1.07	1.37
180 m	-0.0129	-0.0045	-0.0116	1.99	1.06	1.36
190 m	-0.0129	-0.0045	-0.0109	1.98	1.05	1.34
200 m	-0.0128	-0.0045	-0.0098	1.97	1.06	1.31
210 m	-0.0125	-0.0043	-0.0083	1.98	1.07	1.27
220 m	-0.0119	-0.0039	-0.0065	2.03	1.08	1.22
230 m	-0.0109	-0.0034	-0.0044	2.13	1.09	1.16
240 m	-0.0095	-0.0030	-0.0023	2.27	1.10	1.10
250 m	-0.0080	-0.0027	0.0010	2.42	1.11	1.03
260 m	-0.0067	-0.0026	0.0024	2.55	1.13	0.96
270 m	-0.0060	-0.0023	0.0049	2.65	1.14	0.89
280 m	-0.0056	-0.0020	0.0072	2.71	1.14	0.83
290 m	-0.0055	-0.0015	0.0092	2.74	1.14	0.77
300 m	-0.0054	-0.0010	0.0108	2.76	1.14	0.73
310 m	-0.0054	-0.0005	0.0120	2.76	1.12	0.70
320 m	-0.0052	-0.0002	0.0128	2.75	1.11	0.68

Table 4.21: Average results for Model 2 H-H' data line within ±9.83 feet (3 m) of intersection with Model 2 fault for face advancing from 230 feet (70 m) through 1050 feet (320 m).

Avg (± 3m) Model 2	H-H' x-disp (m)	H-H' y-disp (m)	H-H' z-disp (m)	H-H' HSCF-XX	H-H' HSCF-YY	H-H' VSCF-ZZ
70 m	-0.0083	-0.0007	-0.0123	1.91	1.13	1.51
80 m	-0.0086	-0.0009	-0.0123	1.90	1.13	1.51
90 m	-0.0090	-0.0011	-0.0123	1.90	1.13	1.51
100 m	-0.0094	-0.0014	-0.0123	1.90	1.13	1.51
110 m	-0.0099	-0.0016	-0.0123	1.90	1.13	1.51
120 m	-0.0105	-0.0020	-0.0151	1.90	1.12	1.53
130 m	-0.0112	-0.0022	-0.0151	1.90	1.12	1.53
140 m	-0.0119	-0.0025	-0.0151	1.90	1.12	1.53
150 m	-0.0127	-0.0028	-0.0150	1.90	1.11	1.53
160 m	-0.0136	-0.0032	-0.0150	1.89	1.11	1.52
170 m	-0.0147	-0.0036	-0.0149	1.88	1.10	1.52
180 m	-0.0159	-0.0040	-0.0145	1.87	1.10	1.51
190 m	-0.0172	-0.0043	-0.0137	1.86	1.09	1.49
200 m	-0.0171	-0.0044	-0.0124	1.85	1.09	1.45
210 m	-0.0165	-0.0041	-0.0106	1.86	1.09	1.41
220 m	-0.0156	-0.0036	-0.0084	1.90	1.10	1.35
230 m	-0.0143	-0.0030	-0.0061	1.97	1.11	1.29
240 m	-0.0126	-0.0025	-0.0037	2.07	1.11	1.23
250 m	-0.0109	-0.0022	-0.0014	2.18	1.11	1.17
260 m	-0.0095	-0.0019	0.0011	2.27	1.12	1.10
270 m	-0.0084	-0.0017	0.0037	2.33	1.12	1.03
280 m	-0.0076	-0.0013	0.0061	2.38	1.12	0.96
290 m	-0.0072	-0.0008	0.0081	2.40	1.11	0.91
300 m	-0.0067	-0.0004	0.0099	2.41	1.10	0.86
310 m	-0.0065	0.0001	0.0112	2.46	1.09	0.82
320 m	-0.0061	0.0004	0.0121	2.45	1.07	0.80

Table 4.22: Percent change on H-H' within ±9.83 feet (3 m) of intersection with Model 2 fault for face advancing from 230 feet (70 m) through 1050 feet (320 m).

Avg (± 3m) Change	H-H' x-disp (%)	H-H' y-disp (%)	H-H' z-disp (%)	H-H' HSCF-XX (%)	H-H' HSCF-YY (%)	H-H' VSCF-ZZ (%)
70 m	49	-20	2	-7	3	10
80 m	46	-16	2	-7	3	10
90 m	43	-15	2	-7	3	10
100 m	40	-14	2	-7	3	10
110 m	37	-14	1	-7	3	10
120 m	36	-9	24	-7	3	11
130 m	33	-11	24	-7	3	11
140 m	29	-14	24	-7	3	11
150 m	25	-15	24	-7	3	11
160 m	22	-16	24	-7	3	11
170 m	20	-17	24	-6	3	11
180 m	23	-12	26	-6	4	11
190 m	33	-5	26	-6	4	11
200 m	34	-2	26	-6	3	11
210 m	32	-3	27	-6	2	10
220 m	31	-6	30	-7	2	11
230 m	31	-10	37	-8	1	11
240 m	33	-16	65	-9	0	12
250 m	37	-21	-239	-10	0	13
260 m	41	-25	-52	-11	-1	14
270 m	40	-29	-25	-12	-2	16
280 m	36	-35	-16	-12	-2	17
290 m	31	-45	-12	-13	-3	18
300 m	24	-62	-8	-13	-3	18
310 m	20	-116	-7	-11	-3	18
320 m	17	-318	-6	-11	-3	18

Table 4.23: Average results for Model 1 I-I' data line within ±9.83 feet (3 m) of intersection with Model 2 fault for face advancing from 230 feet (70 m) through 1050 feet (320 m).

Avg (± 3m)	I-I'	I-I'	I-I'	I-I'	I-I'	I-I'
Model 1	x-disp (m)	y-disp (m)	z-disp (m)	HSCF-XX	HSCF-YY	VSCF-ZZ
70 m	-0.0031	-0.0007	-0.0085	2.07	1.16	1.28
80 m	-0.0028	-0.0009	-0.0085	2.07	1.16	1.28
90 m	-0.0025	-0.0010	-0.0085	2.07	1.16	1.28
100 m	-0.0022	-0.0012	-0.0085	2.07	1.16	1.28
110 m	-0.0018	-0.0013	-0.0085	2.07	1.15	1.28
120 m	-0.0014	-0.0014	-0.0085	2.07	1.15	1.28
130 m	-0.0009	-0.0016	-0.0085	2.06	1.15	1.28
140 m	-0.0003	-0.0018	-0.0085	2.06	1.15	1.28
150 m	0.0003	-0.0020	-0.0086	2.06	1.15	1.28
160 m	0.0010	-0.0021	-0.0086	2.06	1.15	1.28
170 m	0.0017	-0.0023	-0.0085	2.06	1.14	1.28
180 m	0.0019	-0.0022	-0.0085	2.06	1.14	1.28
190 m	0.0014	-0.0020	-0.0084	2.06	1.14	1.28
200 m	0.0009	-0.0019	-0.0083	2.06	1.14	1.28
210 m	0.0003	-0.0018	-0.0082	2.06	1.14	1.28
220 m	-0.0001	-0.0018	-0.0081	2.06	1.14	1.28
230 m	-0.0004	-0.0018	-0.0079	2.06	1.14	1.28
240 m	-0.0005	-0.0019	-0.0077	2.05	1.14	1.28
250 m	-0.0005	-0.0020	-0.0073	2.05	1.14	1.27
260 m	-0.0003	-0.0021	-0.0067	2.05	1.14	1.27
270 m	-0.0001	-0.0021	-0.0061	2.05	1.14	1.26
280 m	0.0003	-0.0021	-0.0053	2.05	1.14	1.25
290 m	0.0006	-0.0021	-0.0044	2.05	1.15	1.23
300 m	0.0010	-0.0020	-0.0035	2.05	1.15	1.22
310 m	0.0013	-0.0018	-0.0027	2.05	1.15	1.21
320 m	0.0016	-0.0016	-0.0020	2.05	1.14	1.20

Table 4.24: Average results for Model 2 I-I' data line within ±9.83 feet (3 m) of intersection with Model 2 fault for face advancing from 230 feet (70 m) through 1050 feet (320 m).

Avg (± 3m) Model 2	I-I' x-disp (m)	I-I' y-disp (m)	I-I' z-disp (m)	I-I' HSCF-XX	I-I' HSCF-YY	I-I' VSCF-ZZ
70 m	-0.0060	-0.0007	-0.0083	2.01	1.15	1.17
80 m	-0.0058	-0.0008	-0.0083	2.01	1.15	1.17
90 m	-0.0055	-0.0009	-0.0083	2.01	1.15	1.17
100 m	-0.0052	-0.0011	-0.0084	2.01	1.15	1.17
110 m	-0.0048	-0.0012	-0.0084	2.01	1.15	1.17
120 m	-0.0046	-0.0014	-0.0102	2.01	1.15	1.18
130 m	-0.0041	-0.0015	-0.0102	2.01	1.15	1.18
140 m	-0.0036	-0.0016	-0.0102	2.01	1.15	1.18
150 m	-0.0030	-0.0018	-0.0102	2.01	1.15	1.18
160 m	-0.0024	-0.0019	-0.0102	2.01	1.15	1.18
170 m	-0.0018	-0.0020	-0.0102	2.01	1.15	1.18
180 m	-0.0011	-0.0021	-0.0102	2.01	1.15	1.18
190 m	-0.0005	-0.0021	-0.0101	2.01	1.15	1.18
200 m	-0.0011	-0.0020	-0.0100	2.01	1.15	1.18
210 m	-0.0020	-0.0019	-0.0099	2.01	1.15	1.18
220 m	-0.0028	-0.0019	-0.0097	2.01	1.15	1.18
230 m	-0.0033	-0.0019	-0.0094	2.01	1.15	1.18
240 m	-0.0036	-0.0019	-0.0091	2.01	1.15	1.18
250 m	-0.0037	-0.0019	-0.0086	2.01	1.14	1.18
260 m	-0.0037	-0.0019	-0.0079	2.01	1.14	1.17
270 m	-0.0036	-0.0019	-0.0070	2.01	1.14	1.16
280 m	-0.0035	-0.0018	-0.0061	2.01	1.14	1.15
290 m	-0.0033	-0.0017	-0.0050	2.01	1.14	1.15
300 m	-0.0031	-0.0016	-0.0040	2.01	1.14	1.14
310 m	-0.0028	-0.0013	-0.0030	2.00	1.13	1.13
320 m	-0.0026	-0.0011	-0.0022	2.00	1.13	1.12

Table 4.25: Percent change on I-I' within ±9.83 feet (3 m) of intersection with Model 2 fault for face advancing from 230 feet (70 m) through 1050 feet (320 m).

Avg (± 3m) Change	I-I' x-disp (%)	I-I' y-disp (%)	I-I' z-disp (%)	I-I' HSCF-XX (%)	I-I' HSCF-YY (%)	I-I' VSCF-ZZ (%)
70 m	97	-9	-2	-3	-1	-8
80 m	107	-8	-2	-3	-1	-8
90 m	119	-7	-2	-3	-1	-8
100 m	136	-8	-2	-3	-1	-8
110 m	164	-8	-2	-3	-1	-8
120 m	218	-5	19	-2	0	-8
130 m	337	-7	19	-2	0	-8
140 m	932	-10	19	-2	0	-8
150 m	-1093	-11	19	-2	0	-8
160 m	-345	-13	19	-2	0	-8
170 m	-204	-14	19	-2	0	-8
180 m	-157	-7	20	-2	0	-8
190 m	-134	3	21	-2	0	-8
200 m	-217	4	20	-2	0	-8
210 m	-708	3	20	-2	0	-8
220 m	1967	2	20	-2	0	-8
230 m	672	0	19	-2	0	-8
240 m	571	-2	19	-2	0	-8
250 m	648	-4	18	-2	0	-8
260 m	1050	-7	17	-2	0	-8
270 m	7060	-10	16	-2	0	-7
280 m	-1369	-14	15	-2	0	-7
290 m	-625	-18	14	-2	-1	-7
300 m	-407	-21	12	-2	-1	-7
310 m	-309	-26	8	-2	-1	-7
320 m	-266	-33	6	-2	-1	-7

4.3.2 Results Summary of Face Advance Analysis

For A-A' and J-J' data lines, analysis is done wherever the fault/face intersection occurs for a given face advance location. As J-J' moves with the advancing face, the intersection point with A-A' moves from being located in the block of coal to being located in gate entries after 623.4 feet (190 m). Summary comments for these data lines are as follows:

- A-A' data line
    - Y-displacements, Z-displacements, and HSCF-XX changes become significant between the two (2) models after 492 feet (150 m) of face advance. Supports around the fault/face intersection should be increased as the face advances beyond this point.
    - The change in Y-displacement shifts repeatedly between positive and negative values.
    - The change in Z-displacement was positive after 656 feet (200 m) of face advance.
    - X-displacements, although relatively small, undergo significant change beyond 328 feet (100 m) of face advance and these changes between Models 1 and 2 tended to be more negative.
    - HSCF-YY and VSCF are significant until approximately 800 feet (260 m) of face advance. Typically, changes in HSCF-YY and VSCF-ZZ are almost always negative between Models 1 to 2.
    - The fault/face/gate intersection at 558 feet (170 m) of face advance is a critical location for A-A' X-displacements. For the next 66 feet (20m) of face advance the most intense X-displacements along A-A' for any advance location occur.

- J-J’ data line
    - Within the longwall panel, there is significant negative percent changes between Models 1 and 2 for X-displacement, HSCF-YY, and VSCF-ZZ. Z-displacement significantly increased in percent change after 623.4 feet (190 m) of face advance where the analysis enters the gate entry.
    - Along the face at the fault intersection HSCF-XX percentage change is usually insignificant from Model 1 to Model 2.
    - Changes in Y-displacement were only significant after J-J’ was measured in the solid coal beyond the gate entries.
- Extra consideration for ground support should be taken as the face approaches the location where the fault intersects each of the gate entries. Gate entry geometry (including crosscuts) combined with an advancing face and a weak plane intersecting the corner of a solid coal block to be mined by the longwall shearer creates a localized area of low stiffness.

4.3.3 Results Summary of Gate Entry Analysis

Summary comments for the five (5) data lines in the gate entries are as follows:

- E-E’ data line
    - X-displacement change increased significantly from 229.7 ft (70 m) to 393.7 feet (120 m) of face advance, then decreased significantly until 623.4 feet (190 m) of advance. Y-displacement change was significant and negative after 459.3 feet (140 m) of face advance except when the face had advanced 525 feet (160 m)

where it was significant and positive. Change in Z-displacement were significant and positive from 393.7 feet (120 m) to 558 feet (170 m).

  - Percent change in HSCF-YY is significantly negative after 590.1 feet (180 m) of face advance. The percent change is negative for HSCF-XX after 590.1 feet (180 m) of advance and significantly positive after 754.6 feet (230 m) of advance. VSCF-ZZ significantly between positive and negative for face advancement from 492.1 (150 m) to 820.2 feet (250 m).

- F-F' data line
  - At the fault location, X-displacements increase significantly until the face passes the intersection of F-F' and the fault. At this point a significant decrease occurs over the next 131 feet (40 m) of face advance. In both models, X- and Y-displacements move in the positive X-direction and negative Y-direction until the face passes by, at which point the direction of displacements move in the negative X-direction and positive Y-direction. Changes in Y-displacement are consistently and significantly negative after the face advances 230 feet (70 m). Significant positive increases in Z-displacements occur after 304 feet (120 m) of face advance.
  - Changes in HSCFs were relatively insignificant until after 623 feet (190 m) of face advance. VSCF significantly increases in the positive direction until 558 feet (170 m).
- G-G' data line
  - X-displacement change is significantly positive both up to 459 feet (140 m) and after 722 feet (220 m) of face advance. Between these distances, change is

significantly negative. Y-displacement changes are significantly negative after 492 feet (150 m) of face advance except when the face reaches the face/fault intersection distance of 558 feet (170 m). Z-displacement changes are significantly positive from 394 feet (120 m) to 755 feet (230 m) of face advance and significantly negative thereafter.

  - Changes in horizontal stress concentrations are significantly negative after 722 feet (220 m) of face advance.

- H-H' data line
  - X-displacement changes are significantly positive throughout face advancement. Y-displacement changes are nearly entirely significantly negative. Z-displacement changes are significantly positive from 394 feet (120 m) to 787 feet (240 m) of face advance, and then significantly negative after.
  - Changes in horizontal stress concentrations are not very significant. Changes in VSCF are significantly positive throughout face advancement.
- I-I' data line
  - X-displacement changes are significantly positive except when the face (J-J') is within 115 feet (35 m) of the fault intersection with this data line, in which case results are significantly negative. X-displacements are also significantly negative after 919 feet (280 m) of face advance. Y-displacements are significantly negative from 459 feet (140 m) to 558 feet (170 m) of face advance. Z-displacements are significant and positive from 394 feet (120 m) to 984 feet (300 m) of face advance.
  - No changes in SCFs were significant.

4.4 Comparison of Model 2 and Field Results for Gate Entries Intersected by Fault

Roof-to-floor convergence points, roof bolt rosettes, and crib rosettes were installed in the mine to better estimate the geomechanical behavior of the mining environment. Data points were concentrated in entries near the fault intersection. In this comparison of model versus field results, two (2) points were compared. Point 11 is two (2) entries inby of the fault intersection and Point 13 is within the fault intersection (see Figure 4.40). Field and model data were compared without dimensions. In both model and field data, vertical convergence from roof to floor was calculated in meters of convergence per meter of seam thickness (see Figure 4.41).

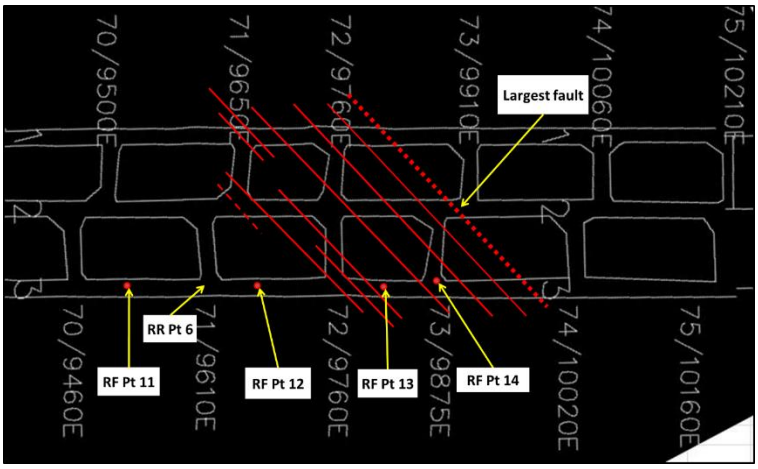

Figure 4.42: Mine map of gate entries showing fault intersection and observation points.

As shown in Figure 4.41, modeling data for Point 11 remains close to field data until the face has advanced 6600 feet (2000 m). Modeling data for Point 13 diverges immediately from field data; however, as the face advances, modeling data and field data behave similarly.

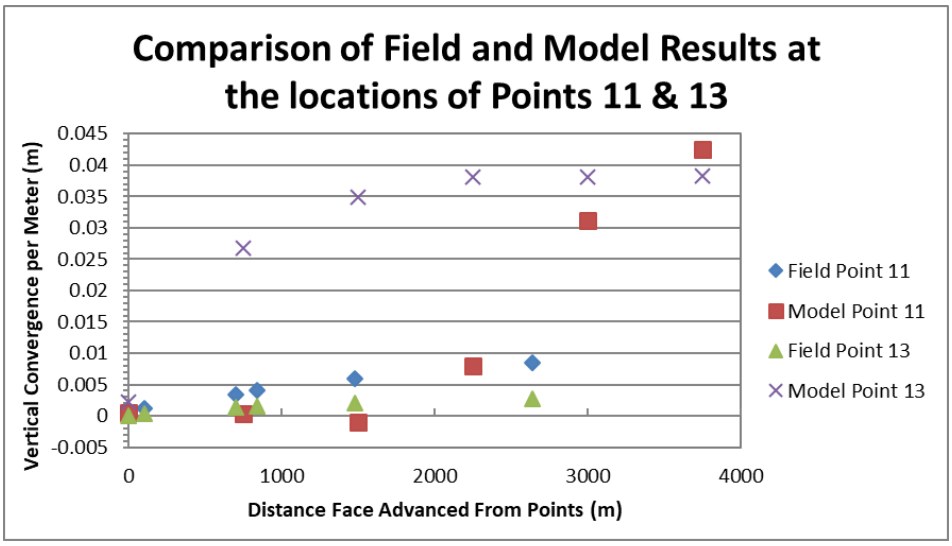

Figure 4.43: Points 11 and 13 results for model and physical mining environment.

There are several reasons for modeling data to not correspond closely to field data. Models were generated for a study of macro-level behavior and the mesh was sized accordingly. Natural mining environments are in a discontinuous environment where the model used a continuum. The rock mass in the field would behave in a more confined manner than the continuous media. In the field, multiple tight parallel faults were associated with the local graben, whereas in the model a single weak plane was introduced. The heterogeneous nature of the rock mass could have at least some influence in the difference of results. Models incorporate regional stress values, but around the fault area, stress values could be much higher. Therefore, at the micro-level within the model, data does not correlate strongly with data observed in the field.

CHAPTER 5

CONCLUSIONS AND RECOMMENDATIONS

5.1 Summary of Research

This study has examined 3D stresses and displacements around a longwall mining system that is intercepted by a geological fault. More specifically, the study analyzed the effect of a fault on longwall gate development entries, set-up rooms, T-junctions, and the longwall face as the longwall face progressed toward, through, and away from the fault. Linear 3D numerical modeling was utilized for this purpose. A general lithologic sequence and mining parameters related to the Herrin No. 6 coal seam in southern Illinois were employed within the model. Rock mass engineering properties were developed for lithologic units associated with the coal seam and used in analysis. The primary goal of this research was to develop a scientific understanding of the effects of faults that can be used to guide the coal mining industry in providing a safe work environment when they are present. A secondary goal was to develop recommendations for a specific mining company to move through a geologic discontinuity without causing safety issues or significant production loss.

FLAC3D code was used for simulating two (2) adjacent longwall faces. Linear elastic rock mass elements with non-linear elastic-plastic fault elements were analyzed using Hoek-Brown brittle failure criteria. Two (2) models were developed for analysis: a base elastic case without faulting and an elastic model with elastic-plastic fault elements. Engineering properties for the rock mass strata were derived from a history of rock core testing and modified following the process indicated for Hoek's Geologic Strength Index. Gob engineering properties and estimated load carrying capacities developed in earlier studies were used to make simulations

physically realistic. The local tectonic (horizontal) stress field and vertical stress levels were applied to the simulation boundaries.

Data was extracted from FLAC3D along several data lines in the roof and floor that were determined to be critical based on the geometry of the mine layout. Extracted data included 3D stresses and displacements with the Z-direction indicating vertical. This data was used to calculate vertical convergence and stress concentration variables VSCF, HSCF-XX, and HSCF-YY. Such data were developed for the longwall face advancing in 30-foot (10-m) increments away from the set-up room.

5.2 Summary of Results

Overall, incremental displacements due to the presence of a fault are more significant than stress concentrations related to the fault. Therefore, only displacement results are summarized. It is important to note that observations made in this study are for the specific fault, mining geometries, and engineering parameters used. Similar analyses must be performed using site specific parameters to understand true effects.

5.2.1 Displacements in Areas where Fault Intersects Set-up Rooms

1. Incremental X-displacements (across the longwall face) around set-up rooms due to the fault are generally small compared to displacements in the Y-direction (along the length of the face) and the Z-direction (vertical).
2. Incremental X-displacements increase consistently in Model 2 by 31-37% in the front row pillar/fault intersection and 2-16% in the second-row pillar/fault intersection.

3. Incremental Y-displacements around the first-row pillar/fault intersection in set-up rooms are high (ranging from -26% up to 39%) when face advance begins, but reduce to almost zero (0) after the face has advanced only 66 feet (20 m).
4. Z-displacements are similar in both models indicating little effect from faulting.
5. Horizontal and vertical stress concentrations are relatively unchanged due to the presence of the fault.

5.2.2 Displacements in Areas where Fault Intersects Gate Development Entries

1. X-displacements (across the face) are small and decrease significantly in the model with the fault until the face passes the area where the fault intersects gate development entries. This is because of the arching effect around the weak fault zone.
2. Incremental Y-displacements (along gate entries) show large decreases (on a percentage basis) around the intersection area as the longwall face advances towards it and away from it, but a rapid increase (on a percentage basis) while the face is at the first gate entry/fault intersection.
3. Z-displacements (vertical) increase significantly in all development entries around the fault intersection zone for at least 200 feet (60 m) before and after the intersection area. Displacements are small in entries further away from the intersection zone.
4. The effect of the fault is to decrease horizontal stress concentration in the gate entry/fault intersection area due to vertical and horizontal deformations along the fault plane. First row gate pillars at the fault experience a decrease in HSCF-XX and HSCF-YY ranging from 7 to 13%. Second row gate pillars experience a decrease in HSCF-XX ranging from 6 to 13%. HSCF-YY remains relatively constant. Once the face passes by the fault intersection area, horizontal stress concentrations are reduced to similar values found in

the model without faulting. This is over about 26 feet (8 m) along gate entry data lines.

5. VSCF values for gate development entry pillars are significantly increased around fault intersection areas; however, these increases at the fault's intersection with the first gate row pillar cease after the longwall face passes by. Increases in VSCF at the second gate row pillar/fault intersection are consistently 10-18%. Values rapidly normalize and are similar to values in the model without faulting within 10 feet (3 m) on either side of the gate development entry/fault intersection area.

5.3 Recommendations for Additional Research

1. This research modeled one (1) possible orientation and dip for a geologic anomaly. Modeling additional fault orientations and dips as well as fault positioning with respect to the longwall panel would show how the rock mass moves under different starting conditions. This sensitivity study would reveal how stresses and displacements change in different mining geometry environments.
2. Rock mass properties of the geologic anomaly are another important sensitivity variable. Additional work needs to be done to ensure properties that are physically realistic.
3. Only one (1) panel was modeled in this study. Faults can go through multiple panels in a mining environment and the size of a safe barrier pillar between panels needs to be evaluated.
4. Except for the region around the fault, all elements were assigned elastic properties. Non-linear analyses must be performed to assess these effects.

BIBLIOGRAPHY

Abbasi, B., Chugh, Y.P., and Gurley, H., 2014. "An Analysis of the Possible Fault Displacements Associated with a Retreating Longwall Face in Illinois." Proceedings, 48th US Rock Mechanics/Geomechanics Symposium, 1-4 June, Minneapolis, MN, USA, 9 pp.

Beck, D., Reusch, F., Arndt, S., Thin, I., Stone, C., Heap, M., and Tyler, D., 2006. "Numerical Modelling of Seismogenic Development during Cave Initiation, Propagation and Breakthrough." Deep and High Stress Mining 2006, 2-4 October, Quebec City, QC, CAN, 15 pp.

Bieniawski, Z.T., 1984. Rock Mechanics Design in Mining and Tunneling. Balkema, Rotterdam, NLD, 272 pp.

Board, M.P., Chacon, E., Varona, P., and Lorig, L., 1996. "Comparative Analysis of Toppling Behaviour at Chuquicamata Open-Pit Mine, Chile." Transactions – Institute of Mining and Metallurgy, Vol. 105, Sec. A – Mining Industry, pp. 11-21.

Chen, J., Mishra, M., Zahl, E., Dunford, J., and Thompson, R., 2002. "Longwall Mining-induced Abutment Loads and Their Impacts on Pillar and Entry Stability." Proceedings, 21st International Conference on Ground Control in Mining, 6-8 August, Morgantown, WV, USA, pp. 11-17.

Chiu, C.-C., Wang, T.-T., Weng, M.-C., and Huang, T.-H., 2013. "Modeling the Anisotropic Behavior of Jointed Rock Mass Using a Modified Smooth-joint Model." *International Journal of Rock Mechanics & Mining Sciences*, 62:14-22.

Chugh, Y.P., Gurley, H., Abbasi, B., Bastola, S., and Carlton, C., 2012. "Analysis and Measurement of Ground Control Stability in Setup Rooms and Gate Roads in an Illinois

Longwall Operation." Proceedings, Illinois Mining Institute Annual Meeting, 22-23 August, Marion, IL, USA, 50 pp.

Chugh, Y.P., Gurley, H., Abbasi, B., Carlton, C., Bastola, S., and Pulliam, J., 2013. "Development and Field Demonstration of Alternate Stable Mining Geometries for Set-up and Recovery Rooms in Illinois." Final Technical Report for Illinois Clean Coal Institute Project No. DEV11-5.

Clark, I., 2006. "Simulation of Rock Mass Strength Using Ubiquitous-joints." Paper No. 08-07, Proceedings, 4th International FLAC Symposium on Numerical Modeling in Geomechanics, Hart, R. and Varona, P. (eds.), 29-31 May, Madrid, SPA.

Deb, D., Kumar, A., and Rosha, R.P.S., 2006. "Forecasting Shield Pressure at a Longwall Face Using Artificial Neural Networks." *Geotechnical & Geological Engineering*, Vol. 24, Issue 4, pp. 1021-1037.

Dimitrakopoulos, R. and Li, S.X., 2010. "Quantification of Fault Uncertainty and Risk Assessment in Longwall Coal Mining: Stochastic Simulation, Back Analysis, Longwall Design and Reserve Risk Assessment." *Mining Technology*, Transactions of the Institutions of Mining and Metallurgy: Section A, Vol. 119, Issue 2, pp. 59-67.

Duplancic, P. and Brady, B.H., 1999. "Characterisation of Caving Mechanisms by Analysis of Seismicity and Rock Stress." Proceedings, 9th International Congress on Rock Mechanics, Paris, FRA, G. Vouille and P. Berest (eds.), Vol. 2, CRC Press/Balkema, Rotterdam NLD, pp. 1049-1053.

Frith, R., 2013. "A Holistic Examination of the Geotechnical Design of Longwall Shields and Associated Mining Risks." Proceedings, 2013 Coal Operators' Conference, University of Wollongong, 14-15 February, pp. 38-49.

Gale, W.J., 2004. "Rock Fracture, Caving and Interaction of Face Supports Under Different Geological Environments: Experience from Australian Coal Mines." Proceedings, 23rd International Conference on Ground Control in Mining, 3-5 August, Morgantown, WV, pp. 11-19.

Gale, W.J., 2005. "Application of Computer Modelling in the Understanding of Caving and Induced Hydraulic Conductivity About Longwall Panels." Proceedings, Coal2005 Conference, 26-28 April, Brisbane, QLD, pp. 11-15.

Hoek, E., Carranza-Torres, C., and Corkum, B., 2002. "Hoek-Brown Criterion – 2002 Edition." Proceedings, NARMS-TAC Conference, Toronto, ONT, CAN, Vol. 1, pp. 267-273.

Hoek, E., Marinos, P.G., and Marinos, V.P., 2005. "Characterisation and Engineering Properties of Tectonically Undisturbed but Lithologically Varied Sedimentary Rock Masses." *International Journal of Rock Mechanics & Mining Sciences*, Vol. 42, pp. 277-285.

Holla, L. and Buizen, M., 1991. "The Ground Movement, Strata Fracturing and Changes in Permeability Due to Deep Longwall Mining." *International Journal of Rock Mechanics and Mining Sciences & Geomechanics*, Vol. 28, Issues 2-3, pp. 207-217.

Hosseini, N., Oraee, K., and Gholinejad, M., 2010. "Design Optimization of Longwall Chain Pillars." Proceedings, 29th International Conference on Ground Control in Mining, 27-29 July, Morgantown, WV, USA, pp. 67-70.

Itasca Consulting Group (ITASCA), 2012. "Fast Lagrangian Analysis of Continua in Three-dimensions Version 5.0."

Kolebaevna, J.M., 1968. Theory of Ground Movement in Rock Mass (in Russian). Nedra, Moscow, RUS, 101 pp.

Laubscher, D.H., 1994. "Cave Mining – The State of the Art." *Journal of South African*

Institute of Mining and Metallurgy, Vol. 94, No. 10, pp. 279-293.

Lietner, R., Potsch, M., and Schubert, W., 2006. "Aspects on the Numerical Modeling of Rock Mass Anisotropy in Tunneling." Felsbau 24:2.

Marinos, P. and Hoek, E., 2000. "GSI: A Geologically Friendly Tool for Rock Mass Strength Estimation." Proceedings, GeoEng2000 International Conference on Geotechnical and Geological Engineering, 19-24 November, Melbourne, AUS, International Society for Rock Mechanics (ISRM), Lancaster, PA, USA, pp. 1422-1446.

Mark, C., Mucho, T.P., and Dolinar, D.R., 1998. "Horizontal Stress and Longwall Headgate Ground Control." *Mining Engineering*, Vol. 50, No. 1, pp. 61-68.

Martin, C.D., Kaiser, P.K., and McCreath, D.R., 1998. "Hoek-Brown Parameters for Predicting the Depth of Brittle Failure around Tunnels." *Canadian Geotechnical Journal*, Vol. 36, No. 1, pp. 136-151.

Medhurst, T.P. and Reed, K., 2005. "Ground Response Curves for Longwall Support Assessment." *Mining Technology*, Transactions of the Institutions of Mining and Metallurgy: Section A, Vol. 114, Issue 2, pp. 81-88.

Medhurst, T.P., Bartlett, M., and Sliwa, R., 2008. "Effect of Grouting on Longwall Mining Through Faults." Proceedings, Coal 2008: Coal Operators' Conference, University of Wollongong & Australasian Institute of Mining and Metallurgy, N. Aziz (ed.), pp. 44-55.

Nelson, W.J. and Krausse, H.-F., 1981. "The Cottage Grove Fault System in Southern Illinois." Illinois State Geological Survey, Circular 522, 71 pp.

Ozbay, U. and Rozgonyi, T.G., 2003. "Numerical Modeling of Stress and Deformations Encountered in Deep Longwall Coal Mines Using Strain Softening Failure Criterion." Proceedings, International Conference on Safety and Environmental Aspects of Mining,

University of Miskolc, Vol. 63, pp. 123-135.

Peng, S.S. and Chiang, H.S., 1984. Longwall Mining. John Wiley & Sons, New York, NY, USA, 720 pp.

Pierce, M., Sainsbury, B.L., and Mas Ivars, D., 2009. "Use of Synthetic Rock Masses (SRM) to Investigate Jointed Rock Mass Strength and Deformation Behavior." Proceedings, International Conference on Rock Joints and Jointed Rock Masses, 4-10 January, Tucson, AZ, USA, 6 pp.

Pierce, M. and Lorig, L., 1998. "*FLAC*^{3D} Analysis of Caveability of the Northparkes E26 Lift 2 Orebody." Itasca Consulting Group, Inc. Report to Northparkes Mines, Parkes, NSW, AUS, #1017, November.

Reyes-Montes, J.M., Sainsbury, B.L., Andrews, J.R., and Young, R.P., 2016. "Application of Cave-Scale Rock Degradation Models in the Imaging of the Seismogenic Zone." CIM Journal, Vol. 7, No. 2, pp. 87-92.

Sainsbury, B.L., Pierce, M., and Mas Ivars, D., 2008. "Analysis of Caving Behavior Using a Synthetic Rock Mass – Ubiquitous Joint Rock Mass Modeling Technique." Proceedings, 1st Southern Hemisphere International Rock Mechanics Symposium (SHIRMS) , Vol. 1 – Mining and Civil, Y. Potvin, J. Carter, A. Dyskin, and R. Jeffrey (eds.), Perth, AUS, pp. 243-254.

Sainsbury, B.L., Pierce, M., and Mas Ivars, D., 2008. "Simulation of Rock Mass Strength Anisotropy and Scale Effects Using a Ubiquitous Joint Rock Mass (UJRM) Model." Proceedings, 1st International FLAC/DEM Symposium on Numerical Modeling, 25-27 August, Minneapolis, MN, USA,

Sainsbury, B.L., 2010. "Sensitivities in the Numerical Assessment of Cave Propagation."

Proceedings, 2nd International Symposium on Block and Sublevel Caving, 20-22 April, Perth, AUS, pp. 523-535.

Sainsbury, B.L., Sainsbury, D.P., and Pierce, M.E., 2011. "A Historical Review of the Development of Numerical Cave Propagation Simulations." Proceedings, 2nd International FLAC/DEM Symposium on Numerical Modelling, 14-16 February, Melbourne, AUS, 14 pp.

Sainsbury, B.L., 2012. A Model for Cave Propagation and Subsidence Assessment in Jointed Rock Masses. Ph.D. Thesis, University of New South Wales, August.

Sainsbury, B.L. and Sainsbury, D.P., 2017. "Practical Use of the Ubiquitous-joint Constitutive Model for the Simulation of Anisotropic Rock Masses." *Rock Mechanics and Rock Engineering*, Vol. 50, Issue 6, pp. 1507-1528.

Salamon, M.G.D., 1990. "Mechanism of Caving in Longwall Coal Mining." Proceedings, 31st US Symposium: Rock Mechanics Contributions and Challenges, 18-20 June, Denver, CO, USA, Hustrulid, W.A. and Johnson, G.A. (eds.), Balkema, Rotterdam, NLD, pp. 161–168.

Salamon, M.D.G., 1991. "Displacements and Stresses Induced by Longwall Mining in Coal." Proceedings, 7th Congress of the International Society for Rock Mechanics, 16-20 September, Aachen, GER, Wittke, W. (ed.), Balkema, Rotterdam, NLD, pp. 1199-1202.

Salamon, M.D.G. and Munro, A.H., 1967. "A Study of the Strength of Coal Pillars." *Journal of South African Institute of Mining and Metallurgy*, 68:55-67.

Shabanimashcool, M. and Li, C., 2012. "A Numerical Study of Stress Changes in Barrier Pillars and a Border Area in a Longwall Coal Mine." *International Journal of Coal Geology*, Vol. 106, February, pp. 39-47.

Thin, I.G.T., Pine, R.J., and Trueman, R., 1993. "Numerical Modelling as an Aid to the Determination of the Stress Distribution in the Goaf Due to Longwall Coal Mining." *International Journal of Rock Mechanics and Mining Sciences & Geomechanics Abstracts*, Vol. 30, Issue 7, pp. 1403-1409.

Trueman, R. and Mawdesley, C., 2003. "Predicting Cave Initiation and Propogation." CIM Bulletin, Vol. 96 (1071), pp. 54-59.

Trueman, R., Thomas, R., and Hoyer, D., 2011. "Understanding the Causes of Roof Control Problems on A Longwall Face from Shield Monitoring Data – A Case Study." Proceedings, 11th Underground Coal Operators' Conference, University of Wollongong & Australasian Institute of Mining and Metallurgy, pp. 40-47.

Vakili, A., Albrecht, J., and Gibson, W., 2010. "Mine-scale Numerical Modelling of Longwall Operations." Proceedings, 2010 Coal Operators' Conference, University of Wollongong & Australasian Institute of Mining and Metallurgy, N. Aziz (ed.), pp. 115-124.

Verma, A.K. and Deb, D., 2007. "Analysis of Chock Shield Pressure Using Finite Element Method and Face Stability Index." *Mining Technology (Trans. IMM A)*, **116**(2), 67-78.

Verma, A.K. and Deb, D., 2008. "Numerical Analysis of the Interaction between Hydraulic Powered Support and Surrounding Rock Strata at Indian Longwall Faces." Proceedings, 12th International Conference of the International Association for Computer Methods and Advances in Geomechanics (IACMAG), 1-6 October, Goa, IND, pp. 394-402.

Wang, T.T. and Huang, T.H., 2009. "A Constitutive Model for the Deformation of a Rock Mass Containing Sets of Ubiquitous Joints." *International Journal of Rock Mechanics and Mining Sciences*, Vol. 46, No. 3, pp. 521-530.

Whittaker, B.N. and Reddish, D.J., 1989. Subsidence: Occurrence, Prediction, and Control.

Elsevier, Amsterdam, NLD, 528 pp.

Weir International, Inc. – WEIR, 2014. "United States Longwall Mining Statistics." Annual Report, 7 pp.

Yu, Z., Chugh, Y.P., Miller, P.E., and Yang, G., 1993. "A Study of Ground Behavior in Longwall Mining through Field Instrumentation." *International Journal of Rock Mechanics & Mining Sciences*, Vol. 30, No. 7, pp. 1441-1444.

VITA

Graduate School

Southern Illinois University

Corbin Carlton

corbincarltonscc@hotmail.com

Southern Illinois University, Carbondale

Bachelor of Science, Mining Engineering, May 2012

Special Honors and Awards: Master Research Fellowship 2012-2015, SIU Carbondale

Thesis Title: An analysis of stresses and displacements around a fault plane due to longwall face advance in coal mining

Major Professor: Yoginder P. Chugh

Publications:

- Chugh, Y.P., Gurley, H., Abbasi, B., **Carlton, C.**, Bastola, S., and Pulliam, J., 2013. "Development and Field Demonstration of Alternate Stable Mining Geometries for Set-up and Recovery Rooms in Illinois." Final Technical Report for Illinois Clean Coal Institute Project No. DEV11-5.
- Bastola, S., **Carlton, C.**, Abbasi, B., Chugh, Y. P. (2013) Stress distribution around typical field intersection geometries in coal mines. Proc. of SME conf., Denver, USA.
- Chugh, Y. P., Gurley, H., Abbasi, B., Bastola, S., **Carlton, C.** (2012) Analysis and measurement of ground control stability in setup rooms and gate roads in an Illinois longwall operation" Illinois Mining Institute Annual Meeting, Illinois, USA